# THESIS APPROVAL

## GRADUATE SCHOOL, KASETSART UNIVERSITY

Doctor of Philosophy (Chemistry)
**DEGREE**

Chemistry
**FIELD**

Chemistry
**DEPARTMENT**

**TITLE:** Sol-gel Synthesized Cerium Promoted $TiO_2$ as Cobalt Catalyst Support for Fischer-Tropsch Synthesis

**NAME:** Miss Anwaraporn Niltharach

**THIS THESIS HAS BEEN ACCEPTED BY**

**THESIS ADVISOR**
( Associate Professor Attera Worayingyong, Ph.D. )

**THESIS CO-ADVISOR**
( Assistant Professor Marisa Arunchaiya, Ph.D. )

**THESIS CO-ADVISOR**
( Assistant Professor Prayoon Songsiriritthigul, Ph.D. )

**DEPARTMENT HEAD**
( Associate Professor Supa Hannongbua, Dr.rer.nat. )

**APPROVED BY THE GRADUATE SCHOOL ON**

**DEAN**
( Associate Professor Gunjana Theeragool, D.Agr. )

## THESIS

# SOL-GEL SYNTHESIZED CERIUM PROMOTED $TiO_2$ AS COBALT CATALYST SUPPORT FOR FISCHER-TROPSCH SYNTHESIS

**ANWARAPORN NILTHARACH**

**A Thesis Submitted in Partial Fulfillment of**
**the Requirements for the Degree of**
**Doctor of Philosophy (Chemistry)**
**Graduate School, Kasetsart University**
**2011**

Anwaraporn Niltharach 2011: Sol-gel Synthesized Cerium Promoted $TiO_2$ as Cobalt Catalyst Support for Fischer-Tropsch Synthesis. Doctor of Philosophy (Chemistry), Major Field: Chemistry, Department of Chemistry. Thesis Advisor: Associate Professor Attera Worayingyong, Ph.D.
184 pages.

Cerium promoted $TiO_2$ samples were synthesized using a sol-gel method with different hydrolysis conditions; low and high water content (ratios of water to Ti-alkoxide precursor: *H*) and different cerium precursors. Mixture phases of anatase and rutile were investigated by X-ray diffraction (XRD) and X-ray absorption near edge structure (XANES). XANES spectra showed that hydrolysis resulted from both high and low cerium percentages of different cerium precursors [$Ce(acac)_3$ and $Ce(NO_3)_3$] did not show significant effect on the mixture phases. Instead, the spectra showed the effects of low and high water content. The low water content method ($H = 4$) produced mainly anatase phase. Raman spectra showed no peaks of $CeO_2$ for the promoted samples. Ce $L_3$-edge EXAFS spectra were used to investigate the localized sites of different cerium loading. Low percentage $Ce/TiO_2$ samples showed that the Ce ions in $TiO_2$ obtained the best fits using the interstitial defect simulations with Ce-O distances of 2.09 and 2.64 Å and Ce-Ti of 2.87 and 3.13 Å. For high percentage $Ce/TiO_2$ samples, EXAFS analysis showed that the Ce ions in $TiO_2$ gained both interstitial and substitution defect simulations with different ratios. From EXAFS results, it could be assumed that different Ce percentages performed different localized sites of Ce ions in $TiO_2$: the lower percentage resided as an interstitial site whereas the higher resided both an interstitial site and the Ti-substitution site in $TiO_2$. As for Fischer-Tropsch catalyst support, the low percentage of cerium ions in $TiO_2$ prepared by the low water content sol-gel method showed complete cobalt reduction at low temperature (550$^{o}$C) as resulted from temperature programmed reduction (TPR). Fischer-Tropsch synthesis with instantaneous total stream sampling analysis technique was tested and the gas products were analyzed using GC equipped FID.

____________________________ ____________________________ ___ / ___ / ___

Student's signature Thesis Advisor's signature

# ACKNOWLEDGEMENTS

First and foremost, I would like to thank my advisor (research director), Assoc. Prof. Dr. Attera Worayingyong for giving me with generous guidance, expert advice through all stages of this research and other wide-ranging research project. I would also like to thank Assist. Prof. Dr. Marisa Arunchaiya for her valuable suggestion.

Special thanks to Assist. Prof. Dr. Prayoon Songsirithikul, Prof. Dr. Sukit Limpijumnong, Dr. Wantana Klysuban and Dr. M.F. Smith at Synchrotron Light Research Institute (Public Organization), Nakhon Ratchasima, for the advice in X-ray absorption spectroscopy and their suggestions. I wish to express my many thanks to Prof. Dr. Han Schulz, Prof. Dr. Olaf Deutschmann and my good friends at Karlsruhe University for their good suggestions and encouragement during my stayed in Karlsruhe, Germany.

I wish to acknowledge Commission on Higher Education for granting of CHE-PhD-SW, DAAD and Department of Chemistry, Faculty of Science, Kasetsart University for the financial support.

Finally, I would like to thank my parents and my friends, who have given me support and encouragement throughout my graduate career. Their love and companionship have been an essential source of strength to me during the course.

Anwaraporn Niltharach
April 2011

# TABLE OF CONTENTS

**Page**

# LIST OF TABLES

## LIST OF TABLES (Continued)

# LIST OF FIGURES

# LIST OF FIGURES **(Continued)**

**Figure** **Page**

## LIST OF FIGURES (Continued)

**Figure** **Page**

## LIST OF FIGURES (Continued)

**Figure** **Page**

**Appendix Figure**

## LIST OF FIGURES (Continued)

# LIST OF ABBREVIATIONS

CP = Co-precipitation

CPr = Cyclopropane

$d_p$ = Particle diameter

EXAFS = Extended X-ray absorption fine structures spectroscopy

FID = Flame ionization detector

FT = Fischer-Tropsch

GC = Gas chromatography

min = Minute

SG = Sol-gel

TEM = Transmission electron microscopy

TPD = Temperature programmed desorption

TPR = Temperature programmed reduction

XANES = X-ray absorption near edge spectroscopy

XAS = X-ray absorption spectroscopy

XPS = X-ray photoelectron spectroscopy

XRD = X-ray diffraction

# SOL-GEL SYNTHESIZED CERIUM PROMOTED $TiO_2$
# AS COBALT CATALYST SUPPORT
# FOR FISCHER-TROPSCH SYNTHESIS

## INTRODUCTION

The Fischer-Tropsch (FT) synthesis has been invented over 70 years by German chemists; Hans Fischer and Franz Tropsch. The FT synthesis produces hydrocarbons from carbon monoxide and hydrogen. Nowadays, it is an interesting and powerful process because the FT synthesis produces high quality fuels. Because of currently the growing demand for energy is largely increasing. Whereas, the amount of fossil fuel available decreases and the limited reserves of these fuels along with the environmental concern (Dominguez *et al.*, 2008). The combustion of fossil fuel produces substantial greenhouse and toxic gases, such as $CO_2$, $SO_x$, $NO_x$ and other pollutants, which are the cause of global warming and acid rain. These reasons have led to research the alternative route to produce the environmentally friendly fuel. (Ni *et al.*, 2006).

The FT synthesis is inherently a very good way to make high quality fuels, environmentally clean transportation fuels, essentially middle distillate liquids used as diesel and jet fuels (Zhang *et al.*, 2005). These fuels can be used as blending stocks for transportation fuels derived from crude oil. Other valuable products besides fuels can be tailor-made with the FT in combination with upgrade processes: for example, ethene, propene, $\alpha$-olefins, ketones, solvents, alcohols and waxes.

FT synthesis, catalysed most commonly by Co- or Fe-based catalysts, is a polymerisation reaction with $CH_2$ as monomer, leading to mainly linear alkanes, ranging from methane to high molecular-weight waxes. Gasoline ($C_{5-9}$) obtained through low temperature FT synthesis has a very low octane number ($\leq 43$) due to the low-branched hydrocarbons selectivity. Hence, the $C_{5-9}$-fraction must be upgraded, mainly through isomerisation and reforming processes. Diesel ($C_{10-20}$) from FT synthesis has a high cetane number (> 70) due to its high n-alkane and low aromatic content. During FT synthesis, long-chain hydrocarbons ($C_{21+}$) are produced which are subsequently hydrocracked and hydroisomerised to produce a high-quality diesel product (i.e. product upgrading) (Subiranas, 2008).

To synthesize Fischer-Tropsch, other factors, such as a catalyst support and a promoter have to be accounted. Ideally, optimum Co catalysts should be prepared by achieving high dispersions of highly reducible Co species. The strength of cobalt–support interaction increases in the order $SiO_2 < TiO_2 < Al_2O_3$. The strong Co–support interaction such as $TiO_2$ leads to high dispersions, but it hinders the reduction of active Co metal sites and also favors the formation of nonreducible cobalt titanates, resulting in a low density of reduced cobalt surface ($Co^0$) sites. Cobalt precursors can be readily reduced on weakly interacting supports (such as $SiO_2$), but supports are unable to stabilize very small precursor crystallites, which leads to a low dispersion of the $Co^0$ particles on the silica surface (Martínez *et al.*, 2003). It has been studied that the reduction of $CoO_x$ was influenced by its interaction with $CeO_2$ (Liu *et al.*, 2007). But the chemical bond of Co-O-Ce on surface made it difficult to reduce $CoO_x$.

In this study, Ce will be deposited into the $TiO_2$ support and be prepared as Ce promoted $TiO_2$ to reduce the interaction of Co-O-Ce. At the same time Co-$TiO_2$ interaction will lead to high Co dispersions together with Ce as a promoter with $Ce^{3+}$/ $Ce^{4+}$ species will ease the $CoO_x$ reduction to Co. Characterization methods such as X-ray diffraction (XRD), Raman and X-ray absorption spectroscopies (XAS) will be employed. FT synthesis and analysis units with instantaneous total stream sampling technique will also be set up and tested.

# OBJECTIVES

1. To prepare Ce promoted on $TiO_2$ support with different cerium precursors and percentages via a sol-gel method. The Ce promoted $TiO_2$ and unpromoted $TiO_2$ are characterized by XRD, Raman spectroscopy and XAS.

2. To prepare Ce promoted $TiO_2$ as a support for the active cobalt FT catalysts. Cobalt on $TiO_2$ support (anatase phase) are prepared via a co-precipitation method for comparison. The catalysts are characterized by XRD, XAS and Temperature Programmed Reduction (TPR).

3. To set up FT analysis unit: Instantaneous total stream sampling (ITSS).

4. To set up FT synthesis unit.

5. To investigate FT synthesis on the cerium promoted $TiO_2$ as cobalt catalyst support and the gas products are analyzed using ITSS.

# LITERATURE REVIEW

## 1. Fischer-Tropsch synthesis

Fischer-Tropsch (FT) synthesis is the transformation process from a gas mixture of synthesis gas or syngas ($H_2$ and CO) to hydrocarbons, which bases on gas to liquids (GTL) technology. The high purity fuels can be obtained from feedstocks such as natural gas, charcoal or biomass other than crude oil. The main products from FT synthesis are aliphatic straight-chain hydrocarbons ($C_xH_y$). Besides, also branched hydrocarbons, unsaturated hydrocarbons, and primary alcohols are formed in minor quantities. The product distribution obtained from FT synthesis includes the light hydrocarbons methane ($CH_4$), ethene ($C_2H_4$) and ethane ($C_2H_6$), liquefied petroleum gas (LPG; $C_3$–$C_4$, propane and butane), gasoline ($C_5$–$C_{12}$), diesel fuel ($C_{13}$–$C_{22}$), and waxes ($C_{23}$–$C_{33}$). The distribution of the products depends on the catalyst and the process parameters such as temperature, pressure, and residence time (Demirbas, 2007).

**Table 1** Conventions of fuel names and composition.

| Name | Synonyms | Components |
|---|---|---|
| Fuel gas | | $C_1 – C_2$ |
| LPG | | $C_3 – C_4$ |
| Gasoline | | $C_5 – C_{12}$ |
| Naphtha | | $C_8 – C_{12}$ |
| Kerosene | Jet Fuel | $C_{11} – C_{13}$ |
| Diesel | Fuel oil | $C_{13} – C_{17}$ |
| Middle distillates | Light gas oil | $C_{10} – C_{20}$ |
| Soft wax | | $C_{19} – C_{23}$ |
| Medium wax | | $C_{24} – C_{35}$ |
| Hard wax | | $C_{35+}$ |

**Source** : Kroschwitz and Howe-Grant (1996)

Fuels produced from the FT process, are high quality due to the fuel is composed of a very low aromatic and absence of sulfur. The highly exothermic FT reaction converts synthesis gas into a large range of linear hydrocarbons as follows:

$$nCO + 2nH_2 \rightarrow (-CH_2-)_n + nH_2O \qquad \Delta H^o_{R\ (250^oC)} = -158\ kJ/mol\ (n=1) \quad (1)$$

Paraffins : $nCO + (2n+1)H_2 \rightarrow C_nH_{2n+2} + nH_2O$ (2)

Olefins : $nCO + 2nH_2 \rightarrow C_nH_{2n} + nH_2O$ (3)

Alcohols : $nCO + 2nH_2 \rightarrow C_nH_{2n+1}OH + (n-1)H_2O$ (4)

Aldehyde : $nCO + (2n-1)H_2 \rightarrow C_nH_{2n}O + (n-1)H_2O$ (5)

The parallel reactions can form as follows:

Water gas shift : $CO + H_2O \leftrightarrow CO_2 + H_2 \qquad \Delta H^o_{R\ (250^oC)} = -39.5\ kJ/mol$ (6)

Boudouard : $2CO \rightarrow C + CO_2 \qquad \Delta H^o_{R\ (250^oC)} = -175.6\ kJ/mol$ (7)

### 1.1 The Fischer-Tropsch process parameters

The activity and selectivity of FT products depend on both catalysts and process parameters. The process parameters, such as temperature, pressure, $H_2/CO$ molar ratio, space velocity etc, affect the activity and selectivity as the followings:

*Temperature:*

Performance of the FT synthesis depends strongly on reaction temperature. Fe- or Co-based catalysts produce high amounts of paraffins and linear products at low temperature. Increasing reaction temperature favors mainly the methane selectivity. Fe catalysts display low selectivity towards methane even at high reaction temperatures. The FT regime with iron may be stable over a wide range of temperature. However, increasing temperature obtains deposition of carbon and thereby deactivation of the catalyst (particularly with iron) (Schulz, 1999).

*Pressure:*

Schulz *et al.*, 1995 reported that the olefin content is generally low at low CO partial and the secondary olefin hydrogenation of $C_3$ obtains a highly selectivity. The results on cobalt concluded that high partial pressure of CO inhibits the secondary olefin hydrogenation, caused by the strongly adsorbed CO reactant. However, the secondary double bond shift is promoted (in contrast to the behavior of iron catalysts).

*$H_2$/CO molar ratio :*

Increasing the $H_2$/CO molar ratio of FT synthesis with cobalt catalysts, reducing the CO partial pressure, favors the $CH_4$ selectivity. This means that with cobalt the FT regime can only exist at a sufficiently high CO partial pressure. With low $H_2$/CO molar inlet ratios, the CO conversion and the $CH_4$ selectivity decreased, while the $C_{5+}$ selectivity and olefin/paraffin ratio for $C_2$-$C_4$ increased slightly (Schulz *et al.*, 2005). Yates *et al*, (1992) studied a cobalt FT catalyst in a well-stirred slurry reactor at 220-240 $^oC$, 0.5-1.5 MPa, $H_2$/CO feed ratios between 1.5 and 3.5. Increasing space velocity decreased the yield of (undesired) $C_1$ products and increased the yield of (desired) $C_{10+}$ products. Reactor temperature and pressure had little effect on the carbon number distribution.

The FT process parameters such as temperature, feed gas, pressure, type of reactor or composition of catalyst affect the FT product distribution and selectivity (as shown in Table 2).

**Table 2** Trend of selectivity changes in the FT synthesis. (+) increase with increasing parameter, (-) decrease with increasing parameter, (~) more complex relation, less pronounced dependency.

| Parameter | $\alpha$ | $S_{CH4}$ | Alkene/ alkane | $S_{alcohol}$ | Chain branching | C-deposition |
|---|---|---|---|---|---|---|
| Temperature | --- | ++ | - | - | ++ | ++ |
| Pressure | ++ | - | ~ | ++ | -- | ~ |
| $p_{H2}/p_{CO}$ | -- | ++ | -- | -- | ++ | -- |
| Conversion | ~ | + | -- | -- | ~ | + |
| Space velocity | ~ | - | ++ | ++ | ~ | ~ |
| Alkali (Fe catalysts) | ++ | - | ++ | + | -- | + |

**Source**: Subiranas and cited in there (2008)

**Note** : $\alpha$ is chain-growth probability

$S_{CH4}$ and $S_{alcohol}$ are selectivity of $CH_4$ and alcohol, respectively.

The FT reaction is highly exothermic, high temperature will increase the rate of desorption (chain growth ($\alpha$) decrease), and consequently lower molecular mass hydrocarbons are favored, especially methane ($S_{CH4}$, which is favored according to chemical equilibrium). As the temperature is increased hydrogenation rates are faster and the ratio alkene/alkane decreases as well as the alcohol selectivity, but the degree of branching increases (also expected from thermodynamics). Furthermore, an increase of hydrogen partial pressure will increase the probability of chain termination by hydrogenation. An increase of total pressure with Co-based catalysts increases the wax selectivity. The composition of a catalyst used in a process also has an effect on chain growth. Potassium is considered as a chemical promoter of iron-based catalysts, it is believed to enhance the electron-donor effect of iron catalysts, therefore facilitating CO adsorption and the dissociation of the C-O bond, while lowering the strength of the metal-hydrogen and the metal-oxygen bond.

## 2. Fischer-Tropsch catalysts

The metals of the group VIII A (such as Fe, Co, Ni, Ru etc.) of the Periodic Table display some activity in the C-C coupling reaction during the hydrogenation of CO. This is related to the capacity of the metals to dissociate CO. Going to the left and up in the group VIII transition metals, the CO dissociation intensifies and excessive carbonization of the metal is risk. Going to the right and down, CO dissociation becomes more difficult and the hydrogenation towards alcohols dominates. Iron, cobalt, nickel, and ruthenium display intermediate behavior and are excellent FT catalysts. Among all these metals however, cobalt and iron catalysts have widely found industrial application.

### 2.1 Active species (Co, Fe, Ni, Ru)

The most-active metals for FT synthesis are Co, Fe, Ru and Ni. Co and Ru are preferred for the synthesis of higher hydrocarbons at low temperatures and high pressures. However, despite Ru has high catalytic activity, it has not found commercial application because of the high price and limited world reserves for this metal compared to Co or Fe (Dijk, 2001). At elevated pressure, Ni tends to form nickel carbonyl with increasing temperature and the selectivity changes to mainly methane (Schulz 1999). Up till now, Fe and Co remain the only catalysts for industrial application.

*Nickel (Ni)*

Nickel is available at a low price and highly hydrogenation activity due to an easy dissociation of CO, resulting highly active for producing excessive amounts of methane. At industrial conditions, nickel mainly produces methane. In addition, the selectivity changes to mainly methane with increasing reaction temperature. This tendency is also observed with Co- and Ru-based catalysts. The major disadvantage of nickel is that it loses activity rapidly by carbon deposition, limiting the reaction pressure and the FT productivity (Cano, 2006).

*Ruthenium (Ru)*

Ruthenium catalyst is the most active FT catalyst. A high molecular weight wax is obtained at low reaction temperature as 423 K. The catalyst is active in a metallic form and no promoters are required to stabilize the activity (Dijk, 2001). However, the high price and relatively rareness of ruthenium exclude its application on industrial scale and Ru–based FT catalyst is also limited to study.

*Iron (Fe)*

Iron catalysts for the FT synthesis can produce the similar products of cobalt catalysts. The FT-regime with iron may be stable over a wide range of temperature. Increasing the reaction temperature to 350 $^{o}$C, the methane selectivity is low. Against cobalt catalysts, the selectivity shifts to mainly methane with increasing temperature (350 $^{o}$C) (Schulz *et al.*, 2005 and cited in there). Iron catalyst for the FT synthesis generally consists of precipitated iron, which is promoted with potassium and copper to obtain a high activity and selectivity (Dijk, 2001). $Al_2O_3$ and/or $SiO_2$ are added as structural stabilizers. Typically, Fe-based catalyst is the active phase for FT appears to be a Fe-carbide. The reaction between the iron metal and carbon is formed by CO-dissociation to produce iron carbide phases in addition to further composition changes (Schulz *et al.*, 2005). Fe-oxides are also formed, which are active for the water-gas shift (WGS) reaction. The high WGS activity causes the iron catalyst to be flexible towards the $H_2$/CO feed ratio of the synthesis gas. However, excess amounts of carbon dioxide can formed via the WGS activity. Thus, iron catalysts were considered unsuitable for once-through operation in gas-based FT plants. Nevertheless, Fe-based catalysts are selective for light olefins at high temperature.

*Cobalt (Co)*

Many of the cobalt catalysts showed good activities for CO conversion and high selectivity to liquid transportation fuels (>$C_5$ hydrocarbons) at low temperature condition. Moreover, cobalt catalysts are lower active for the water-gas shift than iron catalysts and Co-based FT systems are more resistant towards oxidation and more stable against deactivation by water than iron catalysts. Cobalt catalysts are usually supported on metal oxides with high surface area (silica, alumina, titania) due to they can reach the better catalyst stability (Dijk, 2001). Co-based catalysts are preferred for the production of paraffins, as they give the highest yields for high molecular weight hydrocarbons from a relatively clean feedstock, and produce less oxygenates than Fe-based catalysts. This is due to a higher hydrogenation activity of Co-based compared to Fe-based catalysts (Cano, 2006).

FT synthesis proceeds on the surface of cobalt metal particles which are dispersed on the support. FT reaction rate is proportional to the overall number of cobalt surface sites (Diehl and Khodakov, 2008). The number of cobalt surface sites on metal supported catalysts depends on particle size, particle morphology, extent of metal reduction and particle stability. The particle size of cobalt is as small as 6-8 nm also results in higher methane selectivity and higher yields of olefinic products. The reasons of lower specific high molecular weight hydrocarbons activity of smaller cobalt particles could be (i) catalyst deactivation at FT reaction conditions (cobalt oxidation, coking, sintering, formation of mixed cobalt-support compounds) which can occur more rapidly with smaller cobalt particles and (ii) different electronic structure of smaller and larger cobalt particles which would affect intrinsic activity of cobalt metal sites (Diehl and Khodakov, 2008).

## 2.2 Metal oxide supports ($TiO_2$, $SiO_2$, $Al_2O_3$)

Supported cobalt catalysts are highly attractive for the FT synthesis of high molecular weight. The type and structure of the support influence the dispersion, particle size and reducibility and the activity for Co-supported catalysts. The catalyst supports can improve the catalyst activity by dispersing cobalt and increasing the number of active Co metal sites that are stable after reduction and activation. The cobalt is most often present as dispersed clusters on a high surface area support such as $SiO_2$, $TiO_2$ or $Al_2O_3$ (Jacobs *et al.*, 2002). A negative effect of support could be related to the formation of cobalt support mixed compounds (silicate, titanate and aluminate). These mixed cobalt support compounds should be avoided since they do not produce active sites for FT synthesis.

Supported Co catalysts with high efficiency require the synthesis of small metal crystallites ($d > 6$-$8$ nm) at high local surface densities on support surfaces. The formation of these small oxide clusters requires strong interactions between the support and the Co precursor (Iglesia *et al*., 1997). The supports may also directly affect the properties of the metal phase through what is usually classed as 'metal-support interaction'. The strength of cobalt–support interaction increases in the order $SiO_2 < TiO_2 < Al_2O_3$. Ideally, optimum Co catalysts should be prepared by achieving high dispersions of highly reducible Co species. The strong Co–support interaction such as $Al_2O_3$ and $TiO_2$ leads to high dispersions, but hinder the reduction of active Co metal sites and also favors the formation of nonreducible cobalt aluminates and titanates, respectively, resulting in a low density of reduced cobalt surface ($Co^0$) sites. Cobalt precursors can be readily reduced on weakly interacting supports (such as $SiO_2$), but supports are unable to stabilize very small precursor crystallites, which leads to a low dispersion of the $Co^0$ particles on the silica surface (Martínez *et al.*, 2003).

The interaction of cobalt particles with the support has been the subject of many studies. Riva *et al.* (2000) studied cobalt supported on silica and titania catalysts, which prepared by incipient wetness impregnation, using XPS, TPR, TPD, XRD and TEM in order to explain the Co/support interactions and their effect on the dispersion and reducibility of cobalt. Only cubic $Co_3O_4$ was detected by XRD in silica-and titania supported calcined samples. The reduction behavior of cobalt depends on its content in the catalyst. The peaks of the first reduction step show a small trend towards higher reduction temperatures with lower cobalt loading, but has not evident for the second step. The samples containing 2, 5 and 10 wt%Co/silica are reduced completely in experiments with 700 $^{o}$C as the maximum temperature. The TPR peaks fall at higher temperatures for titania supported samples than for silica supported samples. A significant $Co/TiO_2$ interaction was found, while no conclusive proof of any interaction was found for $Co/SiO_2$. Riva revealed that the different reactivity of cobalt with silica and titania explains why reducing and reoxidizing treatments have opposite effects on the dispersion of cobalt supported on $SiO_2$ or $TiO_2$. The low reactivity of cobalt with silica favours sintering effects, after reduction and reoxidation treatments. In contrast, the high reactivity of cobalt with titania due to the coverage of $TiO_2$ by cobalt tends to increase after the same treatments.

The TPR profiles of $TiO_2$ and $Al_2O_3$ supported cobalt catalysts displayed broad peaks at temperatures that are higher than those observed for silica, due to the strong interaction of the Co surface species with the support (Jacobs *et al*., 2002).

Bunjerd *et al*. (2005) revealed influences of various rutile:anatase ratios in titania on the characteristics and catalytic properties of Co/$TiO_2$ catalysts during CO hydrogenation. The 20wt%Co/$TiO_2$ catalysts were prepared by incipient wetness impregnation. XRD results of all calcined samples showed mainly titania peaks and also exhibited weak XRD peaks at $31^o$, $36^o$, and $65^o$, which were assigned to the presence of $Co_3O_4$. However, at high content of the rutile phase, the XRD peaks of $Co_3O_4$ were less apparent due to the strong intensity of XRD peaks for the rutile phase of titania. Based on the XRD results, it was clear that $Co_3O_4$ species were definitely present in a highly dispersed form. TPR profiles of all calcined samples were similarly exhibiting only one strong reduction peak. This peak can be assigned to the overlap of two-step reduction of $Co_3O_4$ to CoO and then to $Co^0$. However, this reduction peak was dramatically shifted about 50–80 $^oC$ lower when ca.3–99% of rutile phase was present in the titania supports. This suggests that the presence of rutile phase in titania can facilitate the reduction process of cobalt oxide species on the titania support leading to reduction at a lower temperature. $H_2$ chemisorption on the reduced cobalt catalyst samples was used to determine the number of reduced Co metal surface atoms. It was found that the amounts of $H_2$ adsorbed increased with the presence of rutile phase in titania up to a maximum of 19% of rutile phase. CO hydrogenation ($H_2$/CO = 10/1) was also performed to determine the overall activity and selectivity at 220 $^oC$ and 1 atm. Their activities increased with the presence of rutile phase in titania up to a maximum of 19% of rutile phase.

Lynch *et al.* (1998) investigated XRD patterns of Co/$TiO_2$ (P25), Co/$Al_2O_3$ and Co/$SiO_2$, which were prepared by incipient wetness impregnation. XRD characterization showed that the only crystalline of cobalt present was $Co_3O_4$ and the corresponding particle size of $Co_3O_4$ were in the order as 75, 20 and 14 nm of Co/$TiO_2$, Co/$Al_2O_3$ and Co/$SiO_2$, respectively. The surface area of Co/$SiO_2$ is higher than Co/$Al_2O_3$ and Co/$TiO_2$. The silica support is amorphous allowing the XRD patterns of Co/$SiO_2$ to be analyzed. In the case of Co/$TiO_2$ the presence of many sharp lines from the support (rutile and anatase forms) prevents the cobalt phases from being correctly analyzed.

*Porous support*

The mesoporous silicas were used to study the effect of support texture of FT catalytic performance. The catalysts supported by periodic mesoporous silicas have exhibited good performance in FT synthesis (Khodakov, 2003). Carbon monoxide conversion was higher on crystalline matrix relative to silica gel. Higher FT catalytic activity and $C_{5+}$ selectivities were also observed on hexagonal mesoporous silicas rather than on MCM-41 cobalt supported catalysts. Hayakawa *et al.* (2007) investigated the effects of co-precipitated silica in iron-based catalysts for FT synthesis. Cobalt-based catalyst was prepared by impregnation of $SiO_2$ to compare their activities. Silica-containing catalysts exhibited micro pores (<10 nm) and large specific surface areas, while the silica-free catalyst had large pores (10–100 nm) and low specific surface area. Co-precipitated silica enhances the productivity of hydrocarbon for FT synthesis, especially $C_{5+}$ hydrocarbon selectivity. Silica-free and silica-containing iron catalyst showed high activity and stability over 100 h test, and exhibited little difference of the product selectivity (olefin/paraffin ratio) over the temperature range of 513–553 K with the $H_2$/CO ratio as 1.0. An iron catalyst has higher activity with the low $H_2$/CO ratio (0.4–1.0). Thus, an iron catalyst has the advantage in applications to coal-derived gas, as compared to the cobalt-based catalyst.

Due to the fact that the efficiency of the cobalt catalysts can be reduced by fractions of cobalt support mixed compounds such as cobalt titanate in the case of titania supported FT catalysts. These compounds are hardly reducible of the active sites for FT synthesis and responsible for a lower overall catalytic activity. Thus, the supports have been modified and promoters are applied on cobalt catalyst to improve their properties (Diehl *et al.*, 2008).

### 2.3 Promoters

Promoters are metal species added to catalysts in small amounts to improve the activity, selectivity and/or stability. Promoters of FT catalysts are noble metals or metal oxides. Numerous studies have shown that introduction of a noble metal (Ru, Re, Rh, Pt or Pd) has strong impact on the structure and dispersion of cobalt species, FT reaction rates and selectivities. The promoting metal is typically introduced via co-impregnation or subsequent impregnation. The literatures suggest that introduction of noble metal could result in the following phenomena (Khodakov, 2008) :

(1) easing cobalt reduction
(2) enhancement of cobalt dispersion
(3) resistance to deactivation
(4) high concentration of hydrogen activation site
(5) modification of intrinsic activity of surface sites

Promotion with oxides has also been one of the methods to improve activity and hydrocarbon selectivity of FT catalysts. The oxide promoters such as $ZrO_2$, $La_2O_3$, MnO and $CeO_2$ have been often employed. Addition of oxide promoters could (Khodakov, 2007):

(1) modify the catalyst texture and porosity
(2) reduce formation of hardly reducible cobalt mixed oxides
(3) increase cobalt dispersion, reducibility and fraction of different cobalt metal crystalline phases

(4) enhance mechanical and chemical attrition resistance of cobalt FT catalysts
(5) improve chemical stability of the support

*Promoted Co/SiO$_2$*

Moradi *et al.* (2003) has discussed that pre-impregnated zirconia makes a protecting layer to prevent major interaction or reaction between silica and cobalt to form cobalt silicate, which can only be reduced at elevated temperature (exceed 800 K). The effect of zirconia addition at various loading ratios on the performance of 10 wt% Co/SiO$_2$ catalysts for the FT synthesis has been studied under H$_2$/CO = 2 at 230 °C and 8 bar for 240 h. The catalysts were prepared through a new pseudo sol–gel method. H$_2$ reduction results with increasing zirconia which favours a high degree of reduction of cobalt at lower temperature and increase in the metallic atoms on the surface. The specific surface area of the catalysts decreases with increasing zirconium loading. The methane selectivity for the promoted catalysts is slightly lower than the unpromoted catalyst. The activity and selectivity for higher hydrocarbons of the promoted catalysts increase with increasing zirconium loading ratios.

*Promoted Co/TiO$_2$*

Li *et al.* (2002) investigated the effect of the addition of small amounts of boron, ruthenium and rhenium on the FT catalyst. The activity and selectivity of a 10wt%Co/P25-TiO$_2$ catalyst has been investigated in a continuously stirred tank reactor. A wide range of synthesis gas conversions has been obtained by varying space velocities over the catalysts. The addition of a small amount of boron (0.05wt%) onto Co/TiO$_2$ do not change the activity at lower space times but slightly increased synthesis gas conversion at higher space times. The product selectivity is not significantly influenced by boron addition for all space velocities. Ruthenium addition (0.20wt%) onto Co/TiO$_2$ and CoB/TiO$_2$ catalysts improves the catalyst activity and selectivity. At a space time of 0.5h-gcat./NL, synthesis gas conversion increased from 50–54 to 68–71% range and methane selectivity decreased from 9.5 to 5.5% (molar carbon basis) for the promoted catalyst. The rhenium promoted (0.34wt%Re) Co/TiO$_2$

catalyst exhibited the highest synthesis gas conversion (73.4%), and at a space time of 0.5h-gcat./NL. In comparison with the results obtained in a fixed bed reactor, the catalysts displayed a higher FT catalytic activity in the continuously stirred tank reactor.

Madikizela *et al.* (2002) has prepared a series of Co (10%)/Zn ($x$%)/$TiO_2$ catalysts *(*$x$ = 0–10%*)* by conventional incipient wetness techniques. TPR, BET, Raman spectroscopy and XRD data reveal that the presence of Zn has a minimal effect on the properties of the Co/$TiO_2$ materials. XPS data reveal that the surface cobalt (and Ti) concentration does not decrease after Zn addition, suggesting that the Co covers the Zn ions on the $TiO_2$ surface. At high Zn coverage, the reducibility of the Co increases slightly. FT synthesis performed on Co (10%)/Zn ($x$%)/$TiO_2$ ($x$ = 0, 5 and 10%) reveals that the Zn enhances the Co activity, but changes the selectivity to lower mass hydrocarbons. The 5% Zn catalyst shows optimal methane production relative to the other two catalysts.

Duvenhage and Coville (2005) studied 5%Fe/5%Co bimetallic catalysts supported on $TiO_2$ in which was promoted with 0.1%, 0.5% and 1.0%potassium, chromium and manganese respectively. The physical properties and CO hydrogenation capabilities were evaluated. Low level promotion (0.1%and0.5%) by K and Cr modestly improved the activity, decreased the selectivity to methane and increased the $C_{5+}$ fraction of the FT product. While the Mn promoted catalysts retarded the activity and reduced selectivity. The Mn was shown to be a poor promoter (olefin, WGS activity) for this catalytic system. On the other hand K and Cr exhibited some favorable promoting features.

Jalama *et al*. (2007) prepared 0.2-5wt% Au promoted on a 10%Co/$TiO_2$ catalyst. Addition of Au to the 10%Co/$TiO_2$ system improved the cobalt dispersion on the catalyst surface. Besides the Au addition can shifted the reduction temperature for the cobalt oxides in interaction with the support to lower temperatures. The catalyst activity for FT reaction increased with an increase in Au loading and passed through a maximum in activity at 1wt%Au. While the methane and light product selectivity increased with Au loading.

*Promoted Co/$Al_2O_3$*

Rohr *et al*. (2000) has been studied the effect of adding zirconia over Co/$Al_2O_3$ catalysts and the reaction conditions. At 5 bar and $H_2$:CO ratio 9:1, zirconia addition to the support leads to a significant increase in both activity and selectivity to higher hydrocarbons as compared to the unmodified catalysts. However, the specific amount of Zr (3, 6 and 10% Zr loading) does not seem to lead to any major differences. Reducibility and cobalt dispersion are not improved by the presence of zirconia compared to the unmodified catalysts. Addition, the comparison of the differ between 9:1 and 2:1 of $H_2$:CO molar ratio, higher $H_2$:CO ratio display a higher CO conversion for the same zirconia over Co/$Al_2O_3$ catalyst. Against, $C_{5+}$ selectivity decrease with increasing $H_2$:CO ratio. The increase of total pressure of reaction yields the decreasing CO conversion and the slightly increasing $C_{5+}$ selectivity of the Co-$ZrO_2$/$Al_2O_3$ catalyst.

Xiong *et al.* (2005) investigated a series of zirconium-modified Co/$Al_2O_3$ catalysts were prepared with a two-step incipient wetness impregnation method. XRD, XPS, TPR, $H_2$-TPD and oxygen titration were used for the characterization of the catalysts. The $CoAl_2O_4$ spinel phase was detected on the prepared catalysts and its content on the catalysts decreased with the increase of zirconium loading, indicating that Zr-added could inhibit $CoAl_2O_4$ formation. The addition of zirconium to the Co catalyst caused the increase of cobalt cluster size. Zr addition has been shown to improve the activity and $C_{5+}$ selectivity of Co/$Al_2O_3$ catalyst for FT synthesis. This could be explained by the increase of active metal cobalt site and reducibility. The increase of zirconium loading on Co/Zr/$Al_2O_3$ catalyst resulted in the increase of olefin/paraffin ratio in the products.

*Promoted Co/$SiO_2$ Co/$TiO_2$ and Co/$Al_2O_3$*

Storsæter *et al*. (2005) prepared 12wt%Co and 0.5wt%Re by incipient wetness co-impregnation of $\gamma$-$Al_2O_3$, $SiO_2$ and $TiO_2$ supports. The effect of water on the activity and selectivity of rhenium promoted cobalt FT catalysts supported on $Al_2O_3$, $TiO_2$ and $SiO_2$ have been studied in a fixed-bed reactor at 483 K and 20 bar. Exposure of the catalysts to water affected to the feed deactivates the $Al_2O_3$ supported catalyst, while the activity of the $TiO_2$ and $SiO_2$ supported catalysts increased. However, at high concentrations of water both the $SiO_2$ and $TiO_2$ supported catalyst deactivated. Common for all catalysts was an increase in $C_{5+}$ selectivity and a decrease in the $CH_4$ selectivity by increasing the water partial pressure.

**Table 3** Examples of the promoted cobalt FT catalysts.

| Promoters | FT catalysts | References |
|---|---|---|
| 0.05wt%B, 0.20wt%Ru, 0.34wt%Re | 10wt%Co/$TiO_2$ (P25) | Li *et al.* 2002 |
| Re | Co/ $SiO_2$ ,$TiO_2$ and $Al_2O_3$ | Bertole *et al*. 2004 |
| - | Co/$TiO_2$-$SO_2$ | Jongsomjit *et al.* 2006 |
| 0.1wt% K, 0.1wt%Mn, 0.5wt%Cr | 5%Fe/5%Co/$TiO_2$(P25) | Duvenhage and Coville 2005 |
| 2wt%Mn | 7.5wt%Co/$TiO_2$(P25) | Morale *et al*. 2005 |
| 1, 5 and 10wt%Zn | 10wt%Co/$TiO_2$ | Madikizela-Madikizela *et al.* 2007 |
| 0.2 - 5wt%Au | 10wt%Co/$TiO_2$(P25) | Jalama *et al.* 2007 |

### 2.4 Fischer-Tropsch reactions on cobalt catalyst

The oxidic form of cobalt catalysts, $Co_3O_4$ is usually the dominant cobalt phase in the prepared catalysts. Several previous reports suggested that reduction of $Co_3O_4$ to metallic cobalt active site may proceed via intermediate formation of CoO:

$$Co_3O_4 \rightarrow CoO \rightarrow Co^0$$

TPR profiles of the supported Co catalysts appeared two peaks, which are attributed to the reduction of $Co_3O_4$ to CoO and then to metallic $Co^0$ at higher temperature, respectively (Diehl and Khodakov, 2008).

The FT reactions on the metallic cobalt surface are proposed as the growth of aliphatic chains in steps of one-carbon-atom species with a prolongation and the alternative reactions of desorption as paraffin and olefin.

The relative rates of its reaction would be as shown in Scheme 1 (Schulz , 2003).

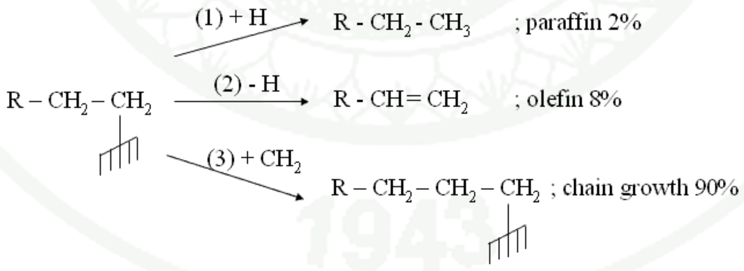

**Scheme 1** Typical alternative relative reaction rates of FT alkyl species for (1) desorption as paraffin, (2) desorption as olefin and (3) chain prolongation.

The associative desorption of the alkyl species together with hydrogen atom to be very slow, gaining paraffin products. Slow desorption of olefin might appears via the transition state of β–H abstraction, which need an adjacent vacant position for intermediate olefin π-adsorption.

Major reactions of the chain prolongation over supported cobalt catalysts were proposed by Schulz (2003) as the followings:

1. $CH_2$ monomer formation

The $CH_2$ monomer formation includes three steps as (1) CO dissociation and thereby carbon formation is possible with the FT catalyst metals (Ni, Ru, Fe, Co) (2) carbon hydrogenation to form CH specie and then (3) $CH_2$ monomer formation.

$$\mathrm{CO} \xrightarrow[(1)]{-\mathrm{O}} \mathrm{C} \overset{+\mathrm{H}}{\underset{(2)}{\rightleftarrows}} \mathrm{CH} \overset{+\mathrm{H}}{\underset{(3)}{\rightleftarrows}} \mathrm{CH_2}$$

Correspondingly, on the segregated cobalt surface, the in-hole sites of high coordination should be most capable for CO dissociation. The $CH_2$ monomer migrates to the on-top growth sites.

The $CH_2$ monomer is assumed to be mobile and capable of migrating to the growth sites. The oxygen from CO dissociation appears to react easily/reversibly with hydrogen and form $H_2O$.

$$\mathrm{O} \overset{+\mathrm{H}}{\rightleftarrows} \mathrm{OH} \overset{+\mathrm{H}}{\rightleftarrows} \mathrm{H_2O}$$

2. Starting of chains

The simplest way on growth sites would be the migration of $CH_2$ from in-hole sites to on-top sites of the supported cobalt surface and take up of a hydrogen atom (Scheme 2) form methyl species. The $CH_3$ species are visualized to be common starters for chains to grow.

**Scheme 2** Starting of chains at on-top sites.

The methyl species on the surface of hydrogenation catalysts can be very stable and accumulated to deactivate the catalysts.

3. Chain growth

The $CH_3$ species on the cobalt on-top sites can react with methyl groups as the methyl insertion to grow chain.

**Scheme 3** Chain growth on-top sites by methylene insertion.

4. Chain termination

Termination of chain growth obtains olefins and paraffins with the alkyl desorption proceeds. The olefin products are formed via dissociative β–H abstraction and paraffin products are formed via associative α-H addition as the following:

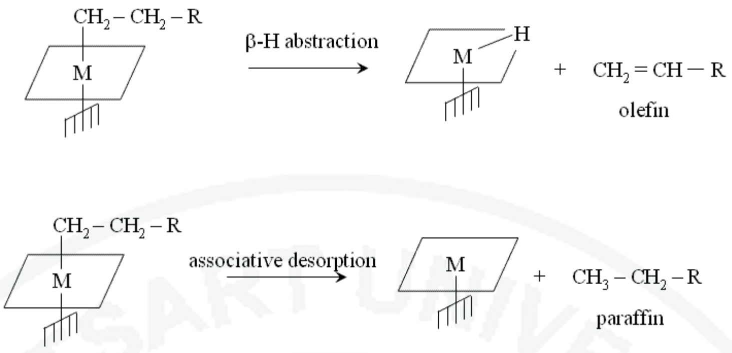

**Scheme 4** Chain termination reactions; formation of α-olefins and of paraffins as primary products of FT synthesis.

However, the FT synthesis on cobalt favored the primary olefin selectivity via β-H-abstraction from the alkyl rather than the primary paraffin selectivity. Thus, the olefin formation is selective on the supported cobalt catalysts as shown in Scheme 1.

Minor reactions of FT synthesis can appear, e.g. the methane formation, chain branching by alkylidene insertion, alcohol formation, on cobalt catalysts. For example, alcohols are the common products from the minor reaction of CO insertion. Alcohol selectivity increases in direction to higher pressure, lower $H_2$/CO molar ratio and lower temperature (Schulz, 2003).

## 3. Catalyst preparation methods

### 3.1 Sol-gel method (Ertl *et al.*, 1997)

A sol-gel process involves the formation of a sol followed by that of a gel. A sol is liquid suspension of solid particles ranging in size from 1 nm to 1 micron. The precursors bonded alkyl group to a central metal atom through an oxygen atom such as inorganic salt or metal alkoxide (M-OR) are used. A sol can be obtained by the hydrolyzed and partial condensation at relatively low temperature. The hydrolysis of the precursor is the addition of water or organic solvent which carefully controls the pH and the reaction temperature. The solvent can be eliminated by distillation under atmospheric pressure resulting in “Xerogel”, while under supercritical condition in autoclave resulting in “Aerogel”. The condensation of sol particles produces a three dimensional gel network. Alternatively, a gel can be produced by destabilizing solution of preformed sols. Sol-gel chemistry with metal alkoxides can be described in terms of two class reactions:

Hydrolysis: $\text{-M-OR} + H_2O \rightarrow \text{-M-OH} + \text{ROH}$
Condensation: $\text{-M-OH} + \text{XO-M-} \rightarrow \text{-M-O-M} + \text{XOH}$

where: X can either be H or R (an alkyl group).

The most important characteristic of the sol-gel preparation of catalytic material is its ease of control that translates into the following advantages:

(1) the ability to maintain high purity (because of purity of starting material);
(2) the ability to change physical characteristics such as pore size distribution and pore volume;
(3) the ability to vary composition homogeneity at a molecular level;
(4) the ability to prepare samples at low temperatures;
(5) the ability to introduce several components in a single step;
(6) the ability to produce samples in different physical forms.

The properties of material prepared by the sol-gel method are controlled by pH, hydrolysis rate, temperature, calcination temperature and atmosphere of calcination.

### 3.1.1 Hydrolysis effect : $H_2O$/metal precursor ratio (*H*)

Condensation/hydrolysis for the sol-gel process can take place by different mechanisms which depend on the metal precursors and conditions used for hydrolysis. Alkoxide groups (M-OR) react with hydroxyl groups (M’-OH), which are formed during the hydrolysis. In the case of substoichiometric quantities (low water content), the hydrolysis of the alkoxide group is not complete and linear oligomers as opposed to branched ones were obtained. When the $H_2O$/metal alkoxide ratio is excess of that required for stoichiometry, hydrolysis is observed to approach completion. This increase in the extent of hydrolysis is observed to lead to highly branched polymeric products, see Schemes 5 and 6.

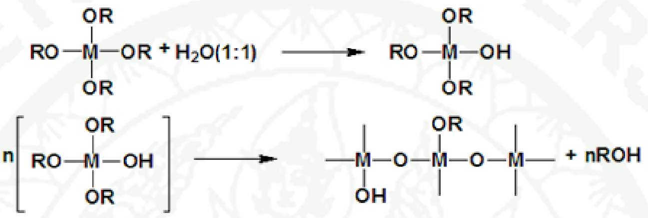

**Scheme 5** Hydrolysis of sol-gel with low $H_2O$/metal precursor ratio**.**

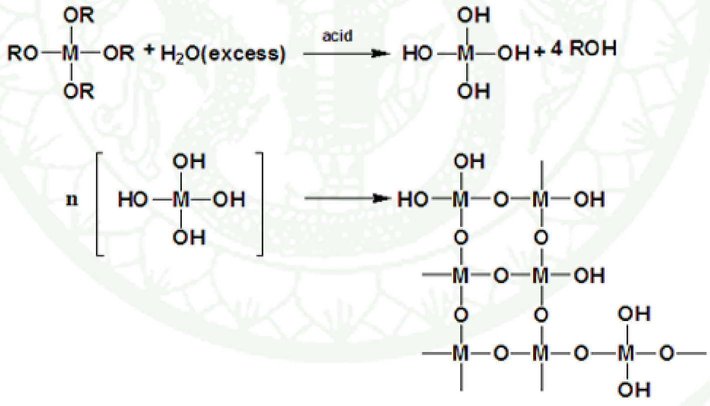

**Scheme 6** Hydrolysis of sol-gel with high $H_2O$/metal precursor ratio**.**

There are many publications investigating the effect of water content. Oskam *et al.* (2003) reported the kinetic growth of $TiO_2$ nanoparticles synthesized from aqueous solution using titanium (IV) isopropoxide as a precursor. The kinetics of the aggregates growth are determined by the stability of the colloid. For water to titanium mole ratio ($H$) < 10, spherical, relatively monodisperse aggregates of nanocrystallites with diameters of 0.5-1 nm are obtained. The high $H$ is very fast and nucleation and growth are completed within seconds. The $TiO_2$ particles formed are unstable and white suspension is immediately formed due to the precipitation of large aggregates. The anatase to rutile transformation depends on the growth time. The growth kinetics of particles can be further modified using different anions, solvents, pH or concentration, since these parameters may affect the equilibrium solubility, the viscosity, the particle shape as well as the energy gain for oriented attachment.

The influence of the hydrolysis process to the anatase-rutile transformation was reported by Zhang *et al.* (2000). They prepared nanosized titania powders by controlling the hydrolysis of $TiCl_4$ in aqueous solution. When $TiCl_4$ solution was hydrolysed at 70 $^{o}$C in the presence of small amount of sulphate ions, the obtained powder was pure anatase phase and the anatase-rutile transformation was inhibited.

### 3.1.2 Hydrolysis effect : pH

The pH of the solution is one of important parameters controlling the hydrolysis. Under acidic condition, the hydrolysis rate is very rapid and gel formation time is increased.

Hu *et al.* (2003) prepared nanosized $TiO_2$ powders using the sol-gel method under various pH values. Brookite formed at low synthesized pH value. It transformed to anatase at low temperature and to rutile at high temperature. It is found that the lattice parameter change with increasing pH value.

The influence of pH on the particle size and morphology of prepared powder has been investigated (Mahshid *et al.,* 2007). The smallest crystallites have been obtained from the hydrolysis in the acidic solution (pH = 2) and the dried powder at 100 ◦C. Furthermore, the size of anatase crystallites increases when calcination temperature has been elevated. The powder in acidic solution consists of spherical particles with poor agglomeration and aggregation takes place at higher temperatures. On the other hand, the powder in basic solution (pH = 9) consists of nonspherical particles with high agglomeration. Anatase to rutile transformation temperature is shifted to the lower than 600 ◦C for nanosize crystallites because of the high surface energy of the particles.

The effect of water and acid concentrations are the main factors influencing both particle size and the standard deviation of size distribution (Hsu and Nacu, 2003). In addition, the temperature and feed rate are the followed influence parameters. An increase acid concentration has the effect of decreasing not only the particle size but also the standard deviation of the size distribution. The presence of acid promoted the hydrolysis rate, acts as a catalyst, and prevented the particle agglomeration through electrostatic repulsions.

### 3.2 Precipitation and Coprecipitation

Precipitation has been widely used to prepare catalysts due to uniform distribution of the active component on the surface of the support. The catalyst also has a high density of active sites. However, precipitation is usually more demanding than several other preparation techniques, due to the necessity of product separation after precipitation and the large volume of salt-containing solution generated in precipitation process.

The main advantages of the precipitation method for the preparation of materials are the possibility of creating very pure materials and the flexibility of the process with respect to final product quality. Coprecipitation is suitable for the generation of a homogeneous distribution of catalyst components or for the creation of precursors with a definite stoichiometry, which can be easily converted to the active catalyst. Such a good dispersion of catalyst component is difficult to achieve by other means of preparation, and thus coprepicitation will remain an important technique in the manufacture of heterogeneous catalysts in spite of the disadvantage associated with such process. These disadvantages are the higher technological demands, the difficulties in following the quality of the precipitated product during the precipitation, and the problems in maintaining a constant product quality throughout the whole precipitation process, if the precipitation is carried out discontinuously (Ertl, 1999).

### 3.3 Impregnation

Impregnation technique is the most common technique for preparation of supported catalysts. A porous support material is impregnated with an aqueous solution of the active metal precursor. If the amount of liquid used for impregnation equals the pore volume of the support, the technique is referred to as *incipient wetness impregnation* (*IWI*). The final metal particle size will inevitably be governed by the morphology, primarily the pore size of the support material. The active metal particle size can be affected by using different metal precursors, different drying and calcinations' conditions, different solvents for impregnation etc. The metal loading achievable in one impregnation is limited to the solubility of the metal precursor. The wet impregnation technique is most often used for preparation of low-loading precious metal catalysts, with very small metal particles (i.e. high metal dispersion).

**Table 4** Examples of catalysts prepared by the sol-gel method and others.

| Catalysts | Preparation method | Ref. |
|---|---|---|
| $CeO_2$-$TiO_2$ thin film | reactive d.c. magnetron sputtering process | Purans *et al.* 2001 |
| $Fe_2O_3/TiO_2$ and $NiO/TiO_2$ | co-precipitation and wet impregnation | Riyas *et al.* 2002 |
| nanostructured $TiO_2$ | sol–gel method | Yeung *et al.* 2003 |
| Fe(10%) Pt(0.1%) K(0.2%)/$SiO_2$ | a novel nonaqueous (acetone) evaporative deposition technique | Xu *et al*. 2003 |
| (20 wt %)Co/$TiO_2$ | incipient wetness impregnation | Jongsomjit *et al.* 2005 |

**Table 4** (Continued)

| Catalysts | Preparation method | Ref. |
|---|---|---|
| $TiO_2$ thin films | radio frequency magnetron sputtering (RF-MS) deposition method | Kikuchi *et al.* 2006 |
| Rutile and anatase mixed crystal $TiO_2$ thin films | pulsed laser deposition | Kitazawa *et al.* 2006 |
| $TiO_2$ films | sol–gel deposited by spin- and dip-coating | Kuznetsova *et al.* 2007 |
| Co(10wt%)/Zn(x)/$TiO_2$ (x = 0,1 ,5 and 10wt%) | sol–gel method | Madikizela-Mnqanqeni *et al.* 2007 |
| Powder $TiO_2$ | hydrolysis and peptization | Mahshid *et al.* 2007 |
| $TiO_2$ and $V_2O_5/TiO_2$ | precipitation and micelle-template method | Mohamed *et al.* 2007 |
| nanocrystalline $TiO_2$ | surfactant-assisted sol–gel method | Jiu *et al*. 2007 |
| $ZrO_2$ and $TiO_2$ | microwave plasma synthesis | Schlabach *et al.* 2007 |

**4. Catalyst characterization**

Spectroscopic techniques are normally used to obtain information on the physico-chemical properties of most practical catalysts, such as X-ray diffraction (XRD), Raman spectroscopy and X-ray absorption spectroscopy (XAS), etc.

4.1 X-ray diffraction (XRD) (Niemantsverdriet, 1995)

XRD is used to obtain information about the structure and composition of crystalline materials. Common compounds can be identified by comparison with reference patterns. The mean crystalline size of a material can also be determined from XRD peak broadening. The line broadening is inversely proportional to crystalline size.

When the incident monochromatic X-ray strikes adjacent atomic planes of a crystal and the X-ray scatters from each of the plane. The X-rays scattered from the crystalline planes interfere constructively, producing a diffracted beam. The XRD pattern of a powdered sample is measured with a stationary x-ray source (usually Cu $K_\alpha$) and a movable detector, which scans the intensity of the diffracted beam as a function of the angle 2θ between the incoming and the diffracted beams.

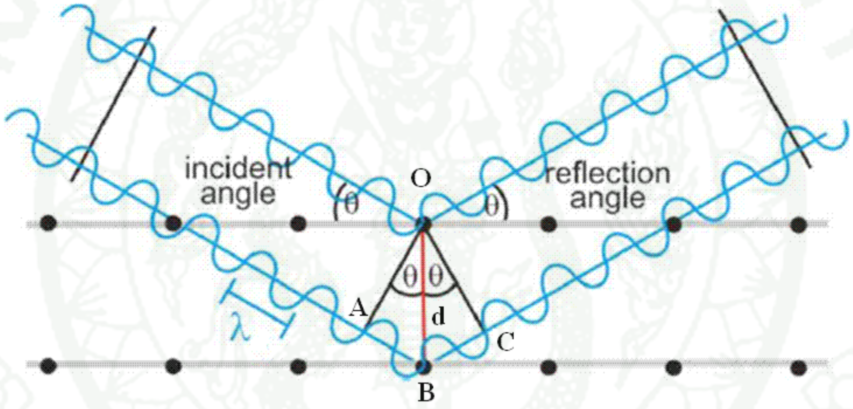

**Figure 1** Bragg's law arise from a set of crystal planes with a spacing $d_{hkl}$.

**Source**: Krumeich (2004)

In Figure 1, the wave reflection from the second plane must travel a distance ABC farther than the wave reflection form the top plane. All waves reflecting from planes below the surface will be phase retarded with respect to the first wave, causing interference. Plane geometry shows that when the distance ABC is exactly equal to one wavelength (λ) and the reflection from all planes at any depth in the crystal will emerge in phase, producing the constructive interference known as diffraction. The well-known Bragg equation follows readily from an analysis of the right triangle OAB. The distance AB may be obtained by taking the sine of θ :

$$AB = d_{hkl} \sin \theta \quad (8)$$

If it is assumed that the initial waves are in phase (constructive interference) with one another and that wave reflect from each plane in the family. The triangle OBC is considered and distance BC equal as $d_{hkl} \sin \theta$. The conditions satisfying this are defined by Bragg's equation:

$$n\lambda = AB+CB = 2d_{hkl}\sin\theta \quad (9)$$

where $\lambda$ : the wavelength of the X-rays

d : the distance between two lattice planes

$\theta$ : the angle between the incoming x-rays and the normal to the reflecting lattice plane

n : the integer called order of the reflection

4.2 Raman spectroscopy

Raman scattering is used to obtain information about structures and properties of molecules from their vibration transitions. It is due to the change in the polarizability of the molecule with respect to its vibration motion.

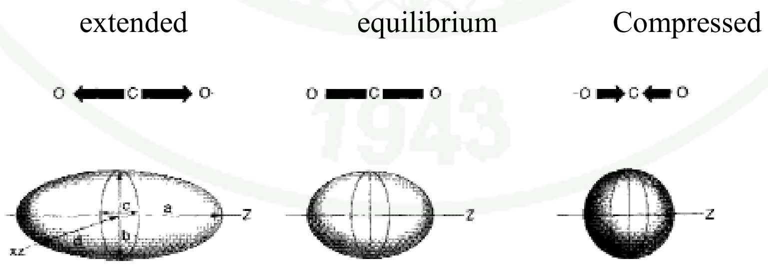

**Figure 2** A change in polarizability of $CO_2$ with vibration motion as Raman active.

**Source:** http://www.chemistry.ucsc.edu/~tholman/Chem256B/LectureNotes/Wk2-Ch6-Drago%20IR.pdf

When a polar molecule is irradiated by monochromatic light (visible, ultraviolet or infrared radiation region) of frequency $\nu_i$(laser), then creates in induced dipole moment in the molecule. The light scatted by the induced dipole of the molecule consists of Rayleigh scattering and Raman scattering. Rayleigh scattering corresponds to the light scattered at the frequency of the incident radiation ($\nu_i$) whereas the Raman scattering is shifted in frequency ($\nu \pm \nu_i$), energy from the frequency of the incident radiation by the vibration energy that is gained or lost in the molecule. If the molecule gains vibrational energy as shown, the scattering is called Stokes Raman scattering ($\nu - \nu_i$), whereas if the molecule loses vibrational energy, the process is known as anti-Stokes Raman scattering ($\nu + \nu_i$) (Figure 3). Thus, Raman spectra are presented as shifts from the incident frequency ( $\Delta\bar{\nu}$ ) and called Raman shift.

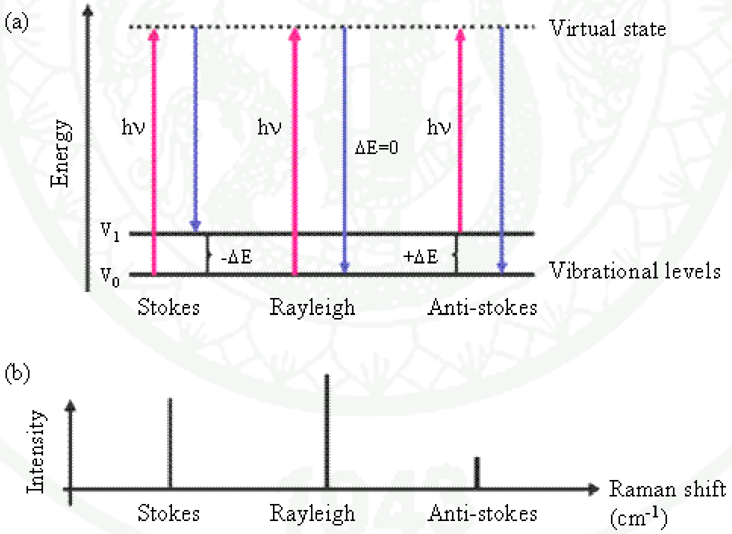

**Figure 3** (a) Schematic representation of Raman emission ; stoke and anti-stoke scattering and $\upsilon$ is vibrational quantum number of ground state ($\upsilon$=0) and excited state ($\upsilon$=1), (b) Spectrum corresponding to Raman emission in (a).

**Source**: Erzinger (2000)

The Raman technique is often superior to the infrared for investigating inorganic systems. Because, the vibration energies of metal-ligand bonds are generally in the range of 100-700 $cm^{-1}$, a region of the infrared that is experimentally difficult to study. These vibrations are frequently Raman active, however, and peaks with $\Delta \bar{\nu}$ values (Raman shift) in this range are readily observed. Raman studies are potentially useful sources of information concerning the composition, structure and stability of coordination compounds. Moreover, Raman spectra obtain information of functional group and fingerprint regions, so this technique is useful for investigating organic and biological systems (Lewis and Edwards, 2001).

### 4.3 X-ray absorption spectroscopy (XAS) (Rehr and Albers, 2000)

X-ray absorption spectroscopy (XAS) is a powerful technique that has long been available for the analysis and characterization of materials. It is one of the premier tools for investigating the local structural environment of metal ions. In XAS experiment when X-ray of energy (hν) strikes on an atom and is absorbed. The intensities of X-ray beam before ($I_0$) and after ($I$) absorption were measured. The X-ray absorption is expressed as:

$$\frac{I}{I_0} = \exp(-ux) \qquad (10)$$

where $u$ is the X-ray absorption coefficient and $x$ is the thickness of sample. From Eq. (10), $ux$ is obtained by plotting $\ln(I/I_0)$ versus the energy of incident X-rays.

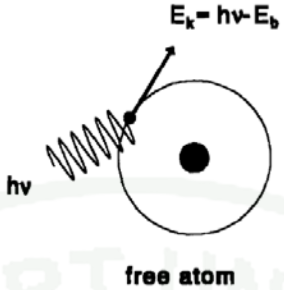

**Figure 4** Absorption of x-ray as a function of photon energy $E=h\nu$ by a free atom.

**Source** : Douglas *et al.* (2007)

In fact, an atom has an electron with binding energy $E_b$, if the photon energy equal to or higher than its binding energy ($h\nu \geq E_b$), the core level electrons are possibly excited into unoccupied states and leave behind a core hole in the atom. The kinetic energy of ejected electron ($E_k$) will be equal to that of the absorbed photon ($h\nu$) minus the binding energy ($E_b$) of the initial core state $E_k = h\nu - E_b$.

Figure 5 shows that XAS can be observed as X-ray absorption near edge structure (XANES), which provides information primarily about geometry and oxidation state, and extended X-ray absorption fine structure (EXAFS) which provides information about metal site. XANES spectroscopy is used to detect and determine oxidation states of metals that are provided by the absolute position of the absorption edge. The near edge absorption region, up to 50 keV above the edge, contains information about vacant orbitals, electronic configuration and site symmetry of the absorbing atom. EXAFS probes the local atomic and chemical environment of a selected element. Besides, X-ray absorption information can confirm and support with other techniques such as X-ray diffraction, Raman spectroscopy and can explain about molecular structures and compositions in the materials.

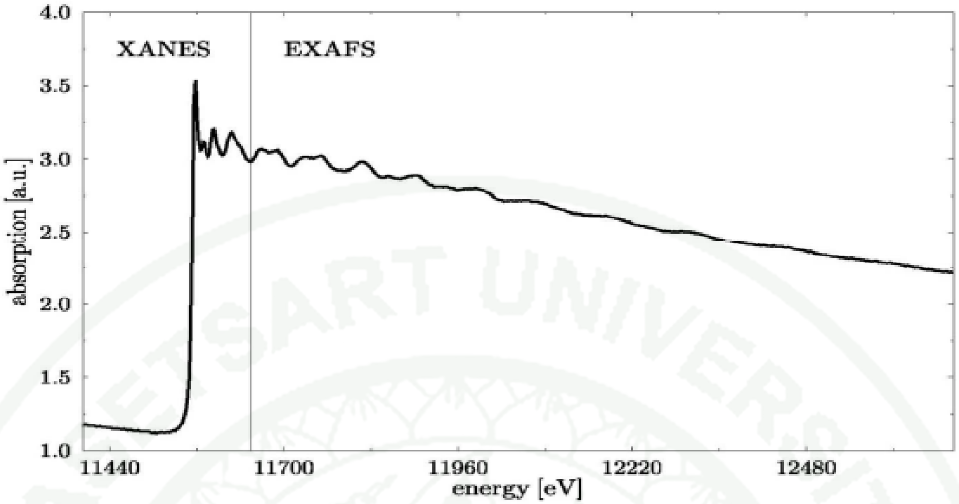

**Figure 5** X-ray absorption spectrum of Pt $L_3$-edge of Pt metal

**Source**: Bare (2003)

### 4.3.1 X-ray absorption near edge structure (XANES)

XANES region is the fingerprint information within ~50 eV of the absorption edge ($E_0$), which provides information primarily about geometry and oxidation state. XANES spectra are labeled according from the shell of excited core electron, such as XANES spectrum of Ti *K*-edge obtained from exciting electron of the *K* shell or 1s orbital of Ti atom, $L_I$ edge from 2s orbital; $L_{II}$, $L_{III}$ edge from 2p orbitals. In the XANES region can be subdivided into three sections as shown in Figure 6; (i) Pre-edge peak is due to the electron transitions from the core level to the higher unfilled or half-filled orbital, such as electron from 1s core level is excited to 3d orbital (1s → 3d transition) of Ti atom. The pre-edge peak is the forbidden transition ($E < E_0$). (ii) Absorption edge peak or white line is the strongest absorption ($E_0$), which occurs when the energy of the incident photon is just sufficient to cause excitation of the core electron of an absorbing atom to the higher state. (iii) XANES peak obtains from transition of core electrons to non-bound levels as the allowed transition, as s → p transition or p → d transition.

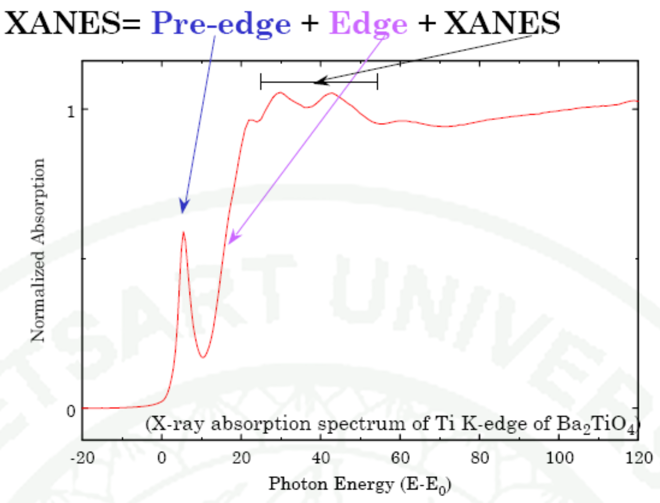

**Figure 6** X-ray absorption spectrum of Ti K-edge of Ba$_2$TiO$_4$ in XANES region including pre-edge, edge and XANES peak.

**Source**: Bare (2003)

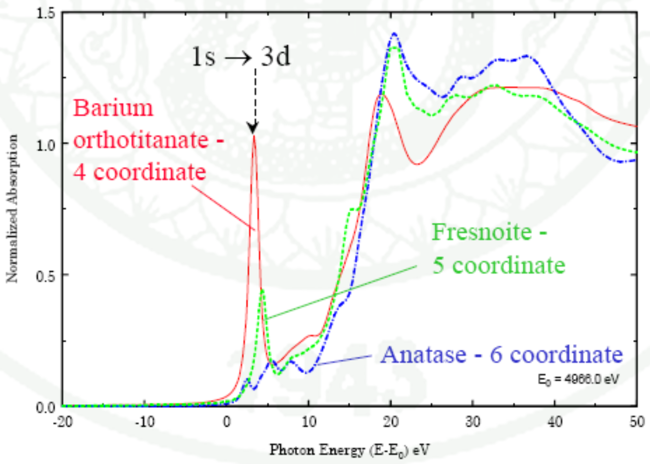

**Figure 7** Pre-edge peaks of Ti atom of 4, 5, 6-fold coordination.

**Source**: Bare (2003)

Figure 7 show the pre-edge peaks of Ti K-edge with different symmetry around Ti atom; 4, 5, 6-fold coordination. Pre-edge peaks of 4-fold coordination in barium orthotitanante ($Ba_2TiO_4$) occur the sharp peak, 5-fold coordination in fresnoite ($Ba_2(TiO)Si_2O_7$) occur the moderate intensity peak and 6-fold coordination in anatase ($TiO_2$) occur three pre-edge peaks. Pre-edge peak in the XANES region can be used for investigating local geometry of compounds.

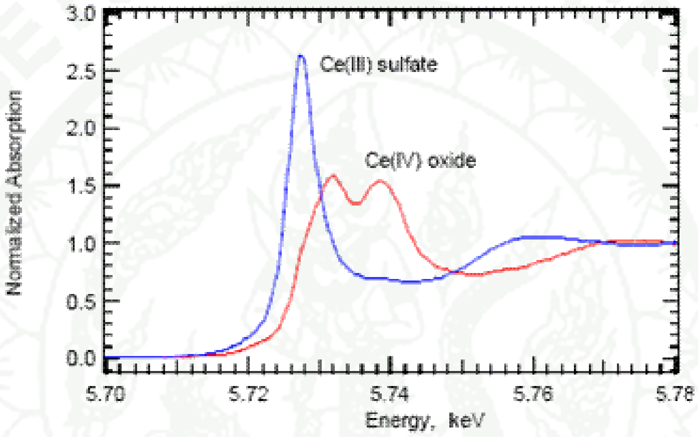

**Figure 8** XANES spectra of $Ce^{3+}$ of Cerium sulfate and $Ce^{4+}$ of Cerium oxide.

**Source**: Bare (2003)

Figure 8 show XANES spectra of Ce $L_3$-edge with different oxidation states of Ce; $Ce^{3+}$ of Cerium sulfate and $Ce^{4+}$ of Cerium oxide. Cerium (III) sulfate occur a sharp peak while cerium (IV) oxide occur double XANES peaks. For the example show XANES spectra can be used to identify the form of interested atom and it can be used as fingerprint (Bare, 2003)

### 4.3.2 Extended X-ray absorption fine structure (EXAFS)

EXAFS spectra range from 50 eV up to 1000 eV above the absorption edge. EXAFS spectra arise from the ejected photoelectron interacts with other electrons in the surrounding non-excited atoms. If the ejected photoelectron is taken to have a wave-like nature, its wave is backscattered by the neighboring atoms.

The maxima and minima after the edge correspond to the constructive and destructive interference between the outgoing photoelectron and the backscattered wave. The resulting interference pattern shows up as a modulation of the measured absorption coefficient, thereby causing the oscillation in the EXAFS spectra. Interference effects are visible in the X-ray absorption spectrum and give detailed information on the distance, number and type of neighbors of the absorbing atom.

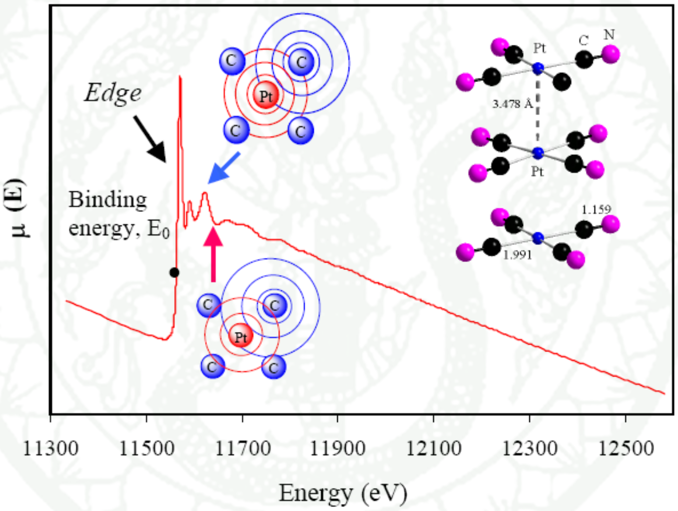

**Figure 9** XAS spectrum of Pt $L_3$ edge of $K_2[Pt(CN)_4]$.

**Source :** www.chem.ucalgary.ca/research/groups/faridehj/xanes.pdf

In order to separate the structural information from the energy dependence of the absorption cross sections, the normalized EXAFS spectrum ($\chi$) is usually defined as the normalized oscillatory part of X-ray absorption coefficient ($\mu$), as

$$\chi(E) = [\ \mu(E) - \mu0(E)]\ /\Delta\mu0(E) \qquad (11)$$

Conventionally, $\chi$ is often defined with respect to photoelectron momentum index, $k = \sqrt{h\omega - |E_c|}$, as measured from threshold, i.e., one defines $\chi(k)$ rather than $\chi$(E) on an absolute energy scale. The EXAFS spectra were analyzed using the standard EXAFS plane wave expression:

$$\chi(k) = \sum_R S_0^2 N_R \frac{|f(k)|}{kR^2} \sin(2kR + 2\delta_c + \Phi) e^{-2R/\lambda(k)} e^{-2\sigma^2 k^2} \tag{12}$$

Where $S_0^2$ is the overall amplitude factor, R is the inter-atomic distances, $N_R$ is the coordination number (or number of equivalent scatterers, |f(k)| is the backscattering amplitude, $\delta_c$ is central atom partial wave phase shift of the final state, $\lambda$(k) is the energy dependent XAFS mean free path, $\sigma$ is Debye-Waller factor as the temperature dependent fluctuation in bond length, which should also include effects due to structural disorder (Rehr and Albers, 2000). Radial structure function obtained by a Fourier transform of the $\chi$ ($k$) is shown in Figure 10.

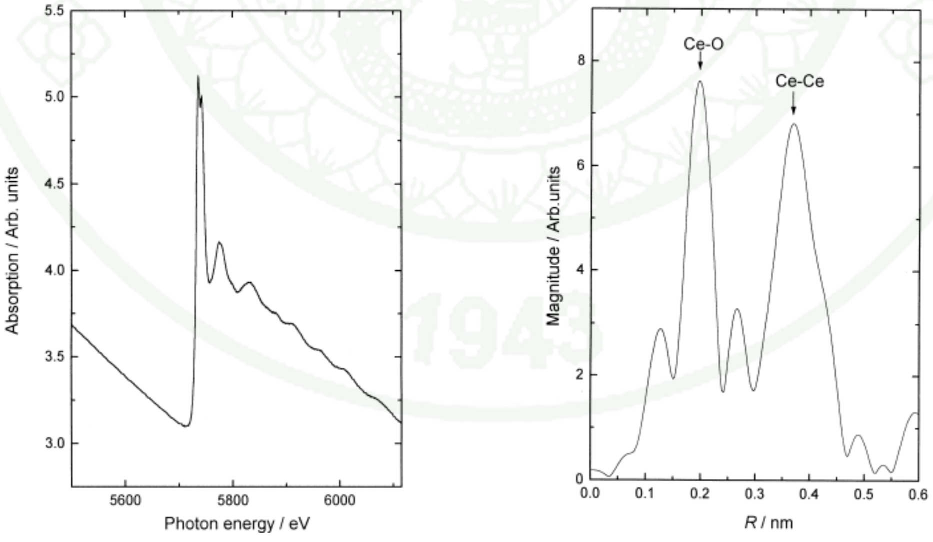

(a) (b)

**Figure 10** X-ray absorption spectrum near Ce $L_3$ edge of $CeO_2$ (a) and Magnitude of Fourier transform of Ce $L_3$ edge of $CeO_2$ (b).

**Figure 10** (Continued)

**Source**: Ohashi *et al.* (1998)

A Fourier transform of the EXAFS with respect to k corresponds to an effective radial distribution function, which peak near the first few near neighbor distances. This important observation paved the way for using EXAFS as a general probe of microscopic structural information in molecules and solids. This technique is especially important in noncrystalline materials, where lattice methods like X-ray diffraction cannot be applied.

*Examples of XAS studies*

Purans et al. (2001) produced CeO2-TiO2 thin film by reactive d.c. magnetron sputtering and studied local structure and electronic properties by X-ray absorption spectroscopy. X-ray absorption spectra at the Ce $L_3$-edge, $L_1$-*edge* and Ti *K*-edge were measured in transmission mode using a Si (311) double-crystal monochromator. The films were deposited on a polyimide substrate. The film thickness lay in the interval of 300–500 nm. The experimental data were analyzed by the EXAFS data analysis software package ‘‘EDA’’. For the XANES spectra of $CeO_2$–$TiO_2$ were compared with $Ce^{4+}$ ions of the crystalline $CeO_2$ and $Ce^{3+}$ ions of $CeTiO_3$. EXAFS data fits concerning the Ce-O shells show the number of nearest neighbors (NN) oxygens = 7.5, 6.6, 6.7 for Ce/Ti being 0.6, 0.3, 0.1, respectively. The Ce-O distance as 2.35 Å is observed in a mixed film with Ce/Ti = 0.6, that agree with $CeO_2$. In contrast, the Ce-O bond length increases (2.38 and 2.39 Å) with decreasing $TiO_2$ content (Ce/Ti =0.3 and 0.1). For Ti *K* edge, the first shell data analysis shows that the Ti-O distance (1.93 Å), and the number of NN oxygens = 5 are independent of the $CeO_2$ content.

Matsuo *et al.* (2005) used Ti *K*-edge XANES to examine the local Ti environments in the sol, gel and xerogels of titanium oxide, which were prepared by a sol-gel method. The xerogels were prepared by heat treatment at 200, 300, 400 500 and 600 $^{o}$C (denoted xero-200, xero-300, xero-400, xero-500 and xero-600), which were doped with Fe(II), Ni(II) and Cu(II) ions (xero-Fe, xero-Ni and xero-Cu). The local structures of the samples were compared using the pre- and post-edge features of the XANES spectra. From the results, the samples could be classified into three groups: a weak Ti-Ti interaction group, an anatase-like structure group and an anatase group. The sol, gel, xerogel and xero-Ni were in the weak Ti-Ti interaction group and the xero-200, xero-Fe and xero-Cu were in the anatase-like structure group. The remaining samples were in the anatase group.

Morales *et al.* (2006) investigated the effects of the addition of manganese to a series of P25 $TiO_2$-supported cobalt FT catalysts using XRD, TPR, TEM and in situ X-ray absorption fine structure (XAFS) spectroscopy at the Co and Mn *K*-edges. After calcination, the catalysts were generally composed of large $Co_3O_4$ clusters in the range 15-35 nm and a $MnO_2$ phase, which existed either dispersed on the $TiO_2$ surface or covering the $Co_3O_4$ particles. Manganese was also found to coexist with the $Co_3O_4$ in the form of $Co_{3-x}Mn_xO_4$ solutions, as revealed by XRD and XAFS. After $H_2$ reduction at 350 °C, XAFS and TEM results showed mostly the formation of very small $Co^0$ particles (~ 2-6 nm), indicating that the cobalt phase tends to re-disperse during the reduction process from $Co_3O_4$ to $Co^0$. The presence of manganese decreased the cobalt reducibility due to the presence of manganese generally led to the formation of larger cobalt agglomerates (~8-15 nm) upon reduction. The XAFS results revealed that all reduced catalysts contained manganese entirely in a $Mn^{2+}$ state, and two well-distinguished compounds could be identified: (1) a highly dispersed $Ti_2MnO_4$-type phase located at the $TiO_2$ surface and (2) a less dispersed MnO phase being in the proximity of the cobalt particles. Furthermore, the MnO was also found to exist partially mixed with a CoO phase in the form of rock-salt $Mn_{1-x}Co_xO$-type solid solutions. The existence of the later solutions was further confirmed by scanning transmission electron microscopy with electron energy loss spectroscopy (STEM-EELS) for a Mn-rich sample. Finally, the cobalt active site composition in the catalysts after reduction at 300 and 350 °C was linked to the catalytic performances obtained under reaction conditions of 220 °C, 1 bar, and $H_2/CO = 2$. The catalysts with larger $Co^0$ particles (~ >5 nm) and lower Co reduction extents displayed a higher intrinsic hydrogenation activity and a longer catalyst lifetime. The MnO and

$Mn_{1-x}Co_xO$ species effectively promoted these larger $Co^0$ particles by increasing the $C_{5+}$ selectivity and decreasing the $CH_4$ production, while they did not significantly influence the selectivity of the catalysts containing very small $Co^0$ particles.

**Table 5** Examples of catalysts characterized by XRD, XPS, XAS and Raman spectroscopy.

| Catalysts | Method | Results | Ref. |
|---|---|---|---|
| $Ce_xTi_{1-x}O_2$ | XRD | -Anatase, rutile, cubic and monoclinic phase composition of $Ce_xTi_{1-x}O_2$ depend on x | Luo *et al.* 2001 |
| | Raman | -Raman spectra of $Ce_xTi_{1-x}O_2$ show crystalline phase depend on x | |
| nanostructured $TiO_2$ | XRD | -pure anatase $TiO_2$ | Yeung *et al.* 2003 |
| | XPS | -only Ti and O, with carbons originating from the organometallic precursors and ambient contamination were detected | |
| | XAS | -The Ti *K*-edge XANES analyses indicate that 5-fold and mostly 6-fold coordinated titanium atoms in P5 and P11, respectively<br>-The EXAFS fitting results, P11 display the characteristic 4 short and 2 long Ti–O bonds of an octahedral anatase, the smaller P5 consist of 3 short (1.93 Å) and 3 long (1.98 Å) Ti–O bonds | |
| Pure rutie and anatase $TiO_2$ | XRD | -the large-grain powder, TiN and $TiO_2$ peaks dominate, and weak peaks $Ti_4O_7$<br>-the small-grained powder consisted of anatase and rutile $TiO_2$ | Oh and Ishigaki 2004 |

**Table 5** (Continued)

| Catalysts | Method | Results | Ref. |
|---|---|---|---|
| Pure rutie and anatase $TiO_2$ | Raman | -The powders with low oxygen flow rates showed Raman bands agree with rutile phase<br>-At high oxygen flow rates, Raman bands correspond to the spectrum of anatase crystal | Oh and Ishigaki 2004 |
| nanoparticles Nd doped $TiO_2$ | EXAFS | - Trivalent Nd ions substitute $Ti^{4+}$ in the $TiO_2$ structure<br>-The substitutional $Nd^{3+}$ ions cause anatase lattice expansion along *c* direction with a maximum value of 0.15 Å at 1.5 % Nd<br>-The lengths of the nearest neighbor Nd-O and Nd-Ti bonds increase by 0.5–0.8 Å compared to pure $TiO_2$ structure | Oh and Ishigaki 2004 |
| $CeO_2$–$TiO_2$ | XRD | -the patterns show the peaks of $CeO_2$ and become much wider and weaker with increasing Ti content | Yang 2006 |
| | BET | -the surface areas increased with the increase of Ti content | |
| | XPS | -the low valence of $Ce^{3+}$ increase with the increase of Ti content | |
| Ce/$TiO_2$ | XPS | -Ce present as a mixture of $Ce^{3+}/^{4+}$ oxidation state<br>-Ti exhibits oxidation state of 4+ | Xu *et al.* 2006 |

**Table 5** (Continued)

| Catalysts | Method | Results | Ref. |
|---|---|---|---|
| Ce/$TiO_2$ | XRD | -0.1% Ce/$TiO_2$ contains only anatase crystallites<br>-The mean crystallite diameter of 0.1% Ce/$TiO_2$ is lower than $TiO_2$ | Xu *et al.* 2006 |
| $TiO_2$ and $V_2O_5$/$TiO_2$ | XRD | anatase and rutile phase, depending on heating and template | Mohamed *et al.* 2007 |
| $ZrO_2$ and $TiO_2$ | XRD | Nanosized $ZrO_2$ and $TiO_2$ is in the cubic/tetragonal and anatase structure , respectively | Schlabach *et al.* 2007 |

# MATERIALS, INSTRUMENTS AND METHODS

## Materials, Instruments

### 1. Catalysts preparation and characterization

1.1 Materials

- Titanium(IV)bis(ethyl acetoacetato)diisopropoxide [[$CH_3C(O\text{-})=CHCO_2C_2H_5]_2Ti[OCH(CH_3)_2]_2$, Aldrich, technical grade]
- Titanium(IV)isopropoxide [$Ti(OC_3H_7)_4$, Fluka]
- Titanium(IV)oxide [$TiO_2$ (anatase) 325 mesh, ≥ 99%, Aldrich]
- Cerium nitrate hexahydrate [$Ce(NO_3)_3$ $6H_2O$, Fluka, 99.0%]
- Cerium(III)acetylacetonate hydrate [$Ce(C_5H_8O_2)_3.xH_2O$, Aldrich]
- Cobalt nitrate hexahydrate [$Co(NO_3)_2{\cdot}6H_2O$, 99.0%, UNIVAR]
- 2-Propanol [$C_3H_8O$, QRëC, AR grade]
- Ethylene glycol [$HOCH_2CH_2OH$, Fluka, 98.0%]
- Acetylacetone [$CH_3COCH_2COCH_3$, Fluka, 98%]
- Nitric acid [$HNO_3$, Merck, 65%]
- Ammonium hydroxide [$NH_4OH$, 26-30% $NH_3$, Mallinckrodt CHEMICAL]
- Aerosil 200 [$SiO_2$ ≥ 99.8%, Degussa]

1.2 Instruments for catalyst characterization

- X-ray diffraction patterns were observed by Philips X'Pert-MPD diffractometer
- Raman spectra were observed by Mk1 Renishaw Raman Imaging Microscope
- XANES and EXAFS spectra were investigated in the transmission mode at the X-ray absorption spectroscopy beamline (BL-8) with electron energy 1.2 GeV,

and beam current 150-80 mA, Synchrotron Light Research Institute (Public Organization)

- Temperature programmed reduction of catalysts were observed by TPD/R/O 1100 Thermo Electron
- Gas chromatographic analyses were performed on Varian gas chromatograph series CP3800

## 2. Instruments for Instantaneous products analysis set-up

The special technique namely: "Instantaneous total stream sampling (ITSS)", which is invented and developed by Schulz and co-workers (Schulz, *et al.*, 1984; Nie, 1996) is used for FT synthesis. ITSS technique is suitable for product streams containing multi component mixtures of gases and vapors as well as FT products. Hot product stream flow into pre-evacuated and pre-warmed ampoules, which are sealed by a gas burner and are later analyzed by a GC.

The advantages of this technique are as follows:

1. The sampling time of this technique does not depend on the GC analysis time.
2. This technique can investigate the selectivity of the catalyst for FT synthesis due to the selectivity changes very fast, especially at the beginning of the reaction (ca. 20 second), which can not be analyzed using the on-line GC method.
3. During reaction and the steady state (reaction time at 12 h and more), the products can also be analyzed.
4. Many samples at the same sampling time can be analyzed with different analysis methods.

ITSS technique includes an evacuated ampoule for storing gas products and devices such as an ampoule sampler for collecting products in a short time (more details in the FT set up, Section 3.2) and an ampoule breaker and lever for breaking the ampoules, which is connected with a GC to analyze organic and inorganic compounds.

2.1 Ampoule breaker

An ampoule (i.d. 8 mm, height 4 cm, length of capillary 14 cm and volume 3 cm$^3$) filled with products is taken into the ampoule breaker connected to a GC-sample donor shown in figure 11 (The detail of the ampoule breaker drawing is in Appendix A). The breaker is heated up under the desired temperature as high as the ampoule sampler temperature to ensure vaporization of the sample. The product mixtures flow into a GC with carrier gas (such as Ar or $N_2$).

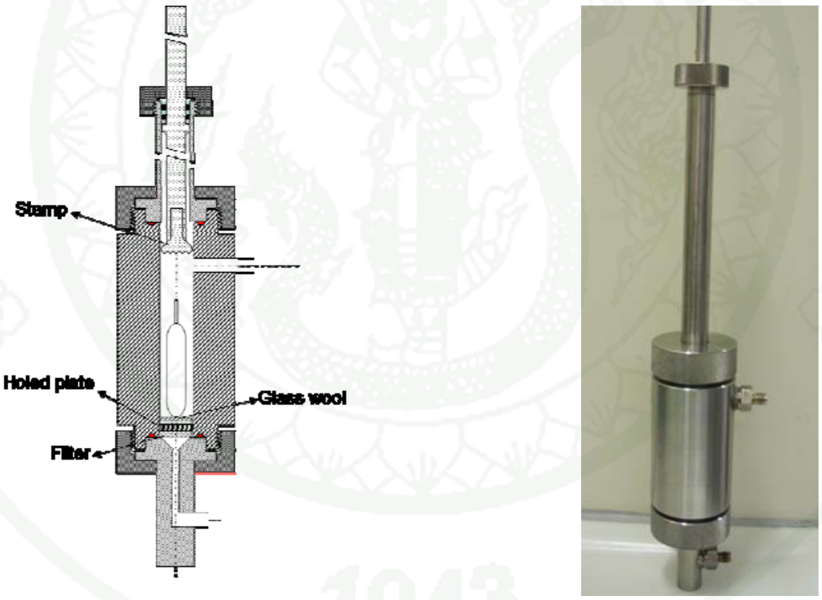

**Figure 11** The ampoule breaker includes the roughly movable stamp, removable upper and lower cover, bored body, and bored tube for controlling the stamp.

The ampoule breaker is connected to a GC as shown in Scheme 7. This system needs carrier gas for introducing the sample into a GC column, a filter for protecting broken glass ampoules into the GC and heating system for avoiding sample vapors condensation.

However, either a manual or a pneumatically controlled lever is necessary for the breaker to crush the sample ampoule as shown in Figure 12.

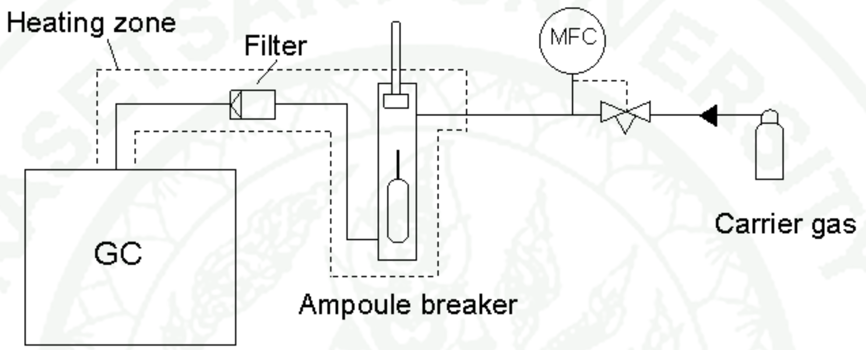

**Scheme 7** ITSS technique: Connection of an ampoule breaker to a gas chromatograph.

(a) (b)

**Figure 12** The ampoule breaker with the manual (a) and the pneumatically controlled system (b).

2.2 Set up for model product substances (Gasoline-Diesel)

The FT synthesis produces synthetic fuels from the synthesis gas, thus the model product substances such as gasoline ($C_5$-$C_{12}$) and diesel ($C_{13}$-$C_{17}$) from a gas station were used to test the efficiency of the existing analysis system. The model product substances include natural gas (methane, ethane), propane, butane, pentane, gasoline and diesel together with nitrogen using as a carrier gas. To obtain the FT model vapors, gasoline and diesel were preheated at 30 °C and 60 °C, respectively. The vapors were collected into the ampoules at 75 °C for avoiding condensation and were analyzed by GC using the existing ITSS analysis system.

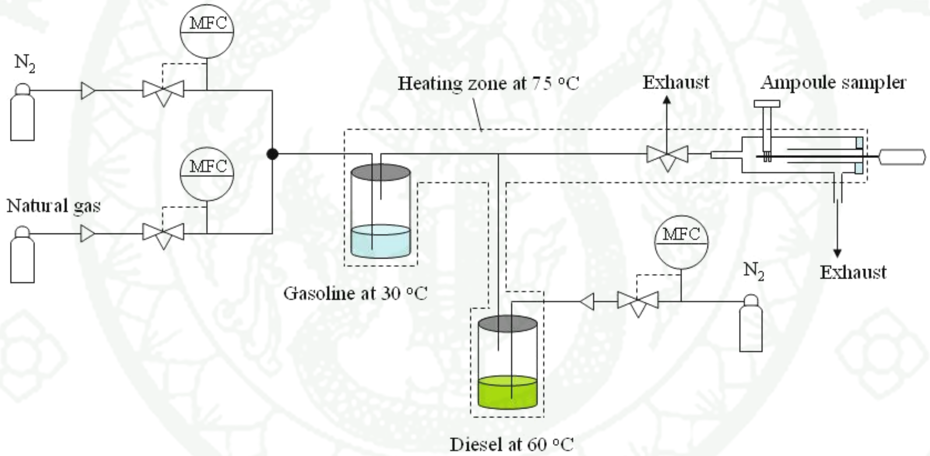

**Figure 13** The experiment set up of FT model product substances.

## 3. Fischer-Tropsch experimental set up

### 3.1 Experimental set up I

The scheme of the FT experimental is illustrated in Scheme 8 and the existing experimental set up is shown in Figure 14.

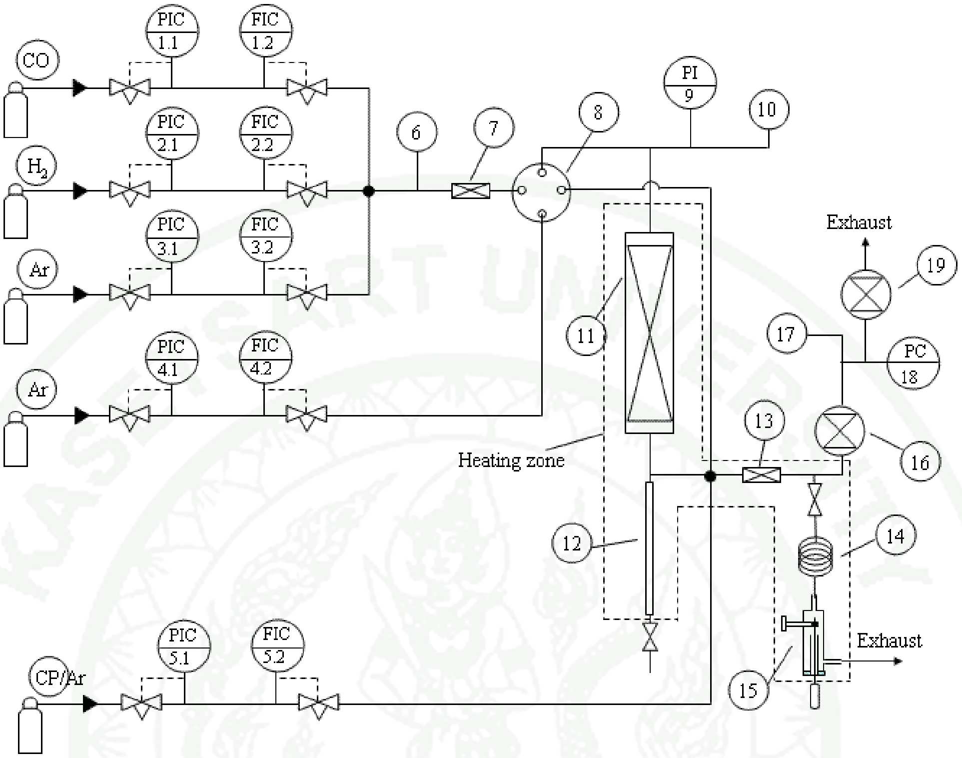

**Scheme 8** FT experimental set up I with a fixed-bed reactor.

**Table 6** Definitions of the numbered apparatus

| Number | Definition |
|---|---|
| 1.1 | Pressure Indicator Controller of CO ; 0-15 bar |
| 1.2 | Flow Indicator Controller of CO [0-100 cm3/min] |
| 2.1 | Pressure Indicator Controller of $H_2$ ; 0-15 bar |
| 2.2 | Flow Indicator Controller of $H_2$ [0-100 $cm^3$/min] |
| 3.1 | Pressure Indicator Controller of Ar ; 0-15 bar |
| 3.2 | Flow Indicator Controller of Ar [0-100 $cm^3$/min] |
| 4.1 | Pressure Indicator Controller of Ar (bypass) ; 0-15 bar |
| 4.2 | Flow Indicator Controller of Ar (bypass) [0-100 $cm^3$/min] |
| 5.1 | Pressure Indicator Controller of 0.5%Cyclopropane (CPr) in Ar ; 0-15 bar |

**Table 6** (Continued)

| Number | Definition |
|---|---|
| 5.2 | Flow Indicator Controller of 0.5%Cyclopropane in Ar [0-100cm$^3$/min] |
| 6 | Overpressure protection device |
| 7 | Mixer |
| 8 | 4-way valve |
| 9 | Pressure indicator |
| 10 | Relief valve |
| 11 | Reactor, oven and Temperature indicator controller |
| 12 | Hot trap |
| 13 | Mixer |
| 14 | Capillary chamber with temperature indicator controller |
| 15 | Ampoule sampler |
| 16 | Cold trap |
| 17 | Relief valve |
| 18 | Pressure Controller Regulator ; 0-25 bar |
| 19 | $H_2O$ absorber |

The fixed-bed reactor is connected to 5 gas cylinders, which are CO, $H_2$, Ar (through reactor and bypass) and 0.5%cyclopropane in Ar as a reference standard for organic products (not produced during FT synthesis). The gas volume flows adjusted by mass flow controllers are fed into the reactor or bypass. Ar is added into the reaction line in order to keep a constant pressure (5 or 10 bar). Before the reactor inlet, a 4-way valve allows to switch to bypass. When the valve is set to bypass, the feed gases ($H_2$/CO = 2) pass through the bypass and Ar(4.1) flows through the reactor until the desired temperature and pressure are reached. On the contrary, the FT synthesis begins after the feed gases flow through the reactor and argon through the bypass. After leaving the reactor, the product stream successively passes through a hot trap (wax trap) at 170 °C, where the gas and liquid phases are separated. The liquid product stream (wax) is removed discontinuously through a valve. A reference gas

(0.5 vol-%cyclopropane-CPr) is added via another mass flow controller, and mixed with the gas product stream after the hot trap (wax trap). The gas product stream is led through a capillary glass in the capillary chamber in order to reduce the pressure from 10 bar to the atmospheric pressure. The product stream continuously passes to the ampoule sampler and fills in the evacuated ampoule. Otherwise, the stream passes to a cold trap (25 °C), where it partially condenses. Thus, liquid products can be collected in the hot trap and the cold trap. Finally, the FT products in the ampoules are analyzed using the existing analysis system.

**Figure 14** Fischer-Tropsch experimental set up I.

### 3.2 Ampoule sampler

An ampoule sampler is a special device for opening an evacuated ampoule by breaking the ampoule capillary and instantaneous sampling small amounts of product stream under desired temperature and pressure. The special features are shown in Figure 15, the ampoule sampler includes a moveable pitchfork for opening the capillary of an ampoule, a sampling chamber for introducing the ampoule into the pitchfork and a removable bottom cover which is designed for ventilating heat. The detail drawing of the ampoule sampler is in Appendix B.

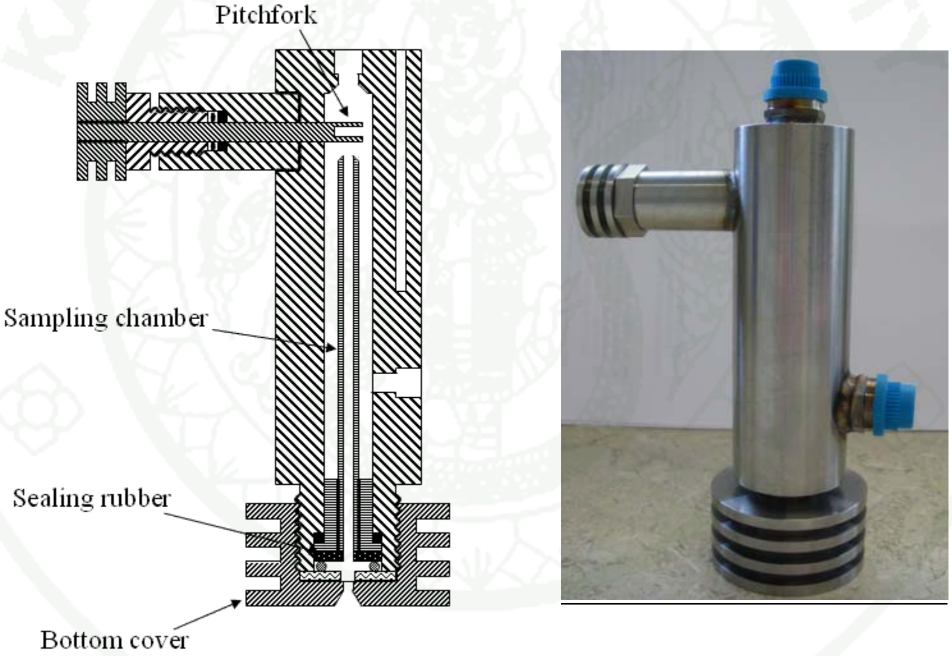

**Figure 15** The ampoule sampler includes a moveable pitchfork, a capillary bored tube and a bottom cover.

An ampoule sampler is connected with the FT experimental set-up at the end of the reaction line (as shown in Scheme 8). The capillary is inserted through a sealing rubber into the sampling chamber, which is filled with the mixture of the product stream and the reference gas. The capillary tip will be cut off with a pitchfork; (product) gases in the reaction line flow into the ampoule. Finally, the ampoule is pulled out and sealed with a small burner in a few second to avoid the pyrolysis of product gases. In this procedure, the gases and vaporized products are stored in the ampoule.

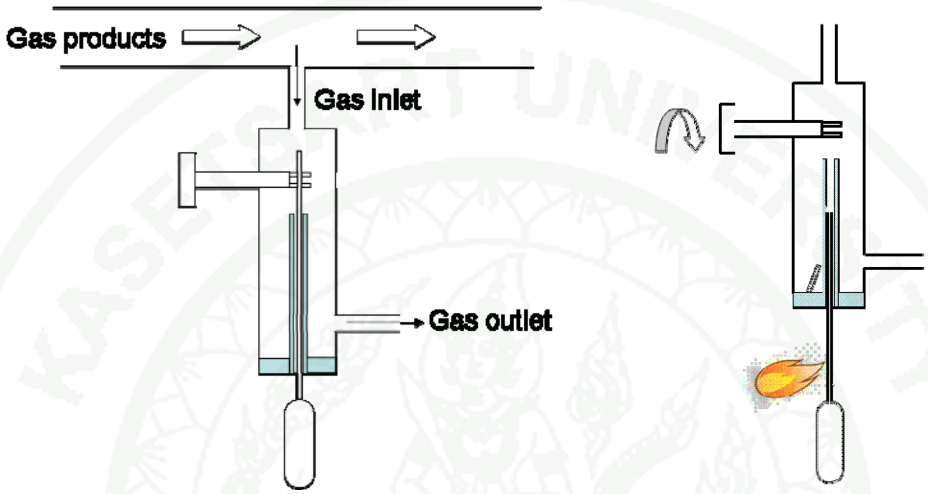

**Scheme 9** The process of sampling the gas products with ampoule sampler.

### 3.3 Experimental set up II

Due to the inconsistent results of the reference gases from the ampoule sampler of the experimental line (Set up I), the Experimental set up I is developed to the set up II as shown in Scheme 10. The capillary tube in a chamber (apparatus no. 14) which was used to reduce the reaction pressure has been removed and a leak valve (apparatus no. 20) is installed for controlling pressure inside the reactor to 5 or 10 bar. In addition, a flow indicator (apparatus no. 21) is placed after the ampoule sampler to check the gas flow during the sampling.

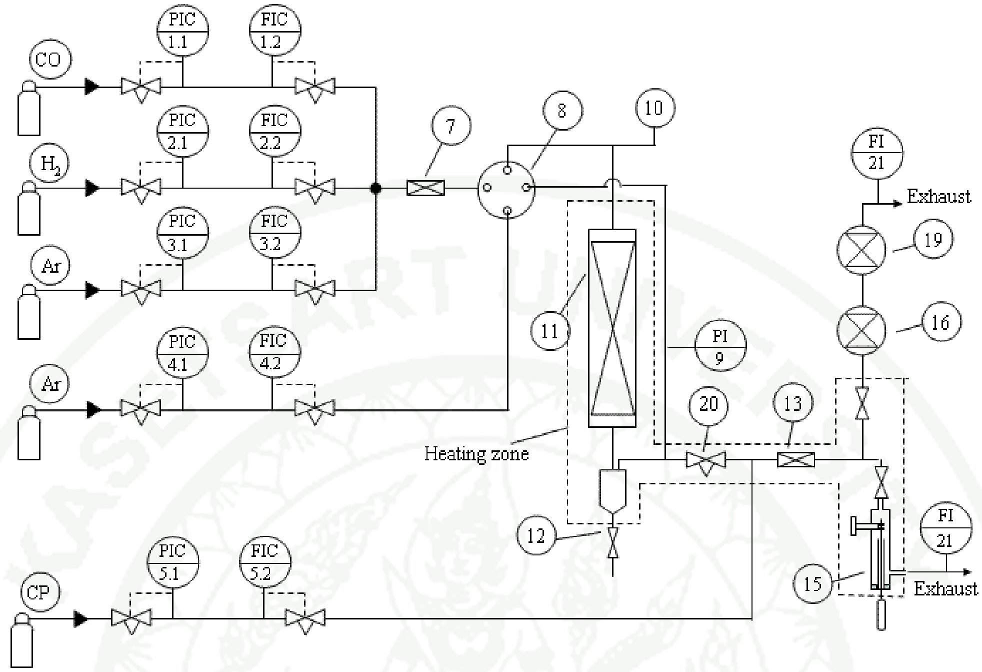

**Scheme 10** Fischer-Tropsch experimental set up II.

## 4. Fixed bed Reactor

The reactor consists of a quartz tubing and a stainless steel tubing. A quartz tubing (o.d. = 12.00 mm, i.d. = 10.00 mm, L = 560.00 mm) filled with catalyst. The quartz tubing is placed inside the stainless steel tubing (o.d. 18.00 mm, i.d. 14.00 mm, L = 660.00 mm) for pressure relief, avoiding the interference effect from metal tubing, its inert material property and the hot spot phenomena. (The detail of the reactor drawing is in Appendix C).

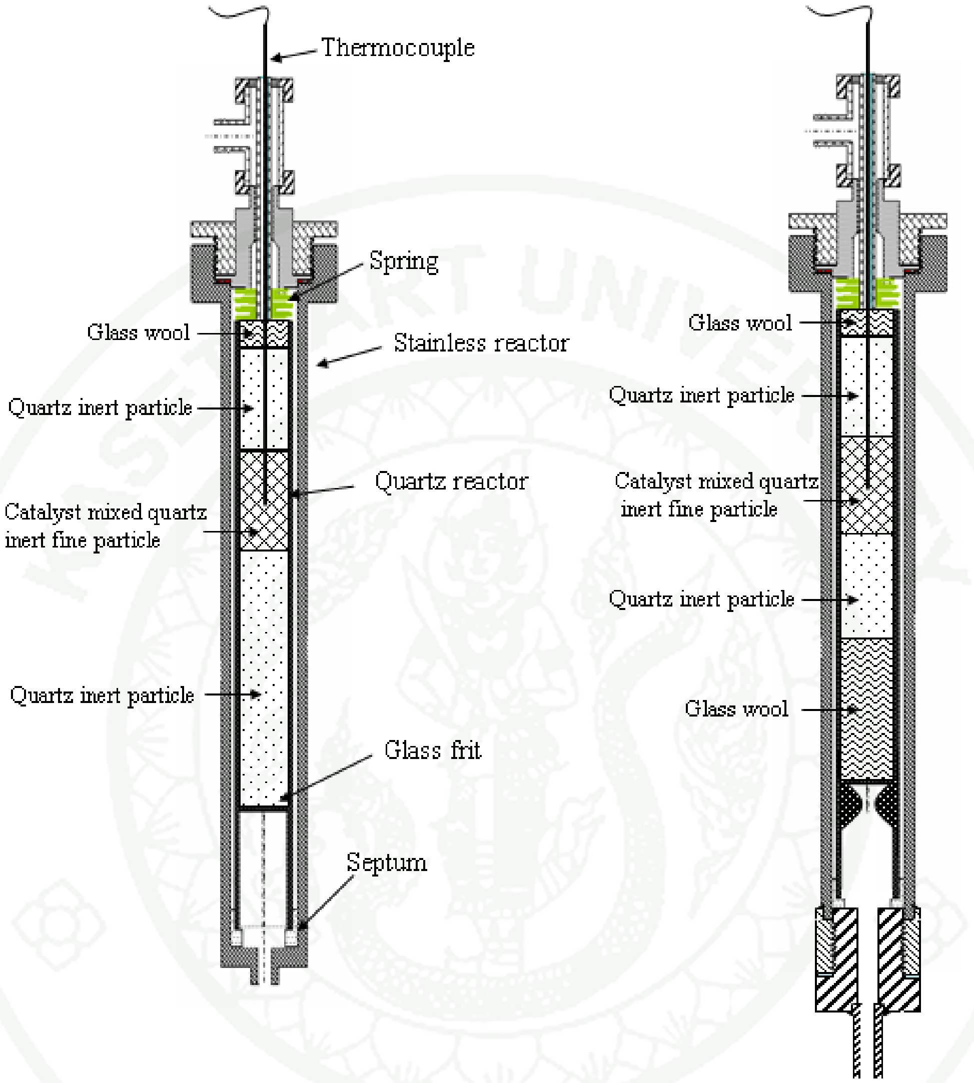

Type (a) Type (b)

**Figure 16** Cross section of the catalyst-bed configurations (quartz reactor). Type (a) : an original reactor and Type (b): a developed reactor. Quartz inert particle ($d_p$ > 0.35 mm), Cobalt based catalyst ($d_p$ 0.15 mm) ~2 grams, diluted with 5 $cm^3$ quartz inert fine particle ($d_p$ 0.2-0.35 mm).

Figure 16 shows the catalyst bed in the quartz reactor. The mixture of catalyst and quartz were filled into the quartz reactor at the isothermal zone of the furnace. The catalyst bed is positioned on a sintered quartz frit (Type a) or a U-shape (Type b) to prevent the catalyst and quartz fine particle from flowing through the quartz tubing.

The thermocouple in the ceramic tube is placed at the middle of the catalyst bed. To avoid any gas bypassing the reactor, the quartz tubing is pressed onto a septum seal with a spring. Type (a) quartz tubing was used as a reactor with the experimental set up I. Due to the fritted joint, which was broken easily, the quartz tubing was developed to Type (b) with the U-shape. The type (b) quartz reactor has been used with the experimental set up II.

# Methods

## 1. Catalyst preparations and characterizations

The catalyst preparations and characterizations are divided into 2 main parts as follows:

1.1 Preparations and characterizations of catalyst supports:
$TiO_{2(SG)}$ and $Ce/TiO_{2(SG)}$

1.2 Preparations and characterizations of modified cobalt catalysts:
$Co_{CP}$-$Ce_{CP}$/$TiO_2$(anatase)
$Co_{CP}$/Ce-$TiO_{2(SG)}$
$Co_{SG}$-$Ce_{SG}$/$SiO_2$(aerosil)

### 1.1. Preparations and characterizations of catalyst supports: $TiO_{2(SG)}$ and $Ce/TiO_{2(SG)}$

1.1.1 $TiO_2$ by sol-gel method: $TiO_{2(SG)}$

*- Hydrolysis effect : mole of water/mole of Titanium precursor (H)*

(a) Low water content ($H = 4$)

The titanium precursor [Titanium (IV) bis (ethyl acetoacetato) diisopropoxide] 4.2435 g (0.01 mol) was mixed with acetylacetone 0.715 g (7.15 mmol), ethylene glycol 4.50 $cm^3$ (79 mmol) and stirred to get homogeneous mixture. Water 0.71 g (0.04 mol) was added and stirred until the solution was clear. The solution was allowed to rest in an oven at 348 K to form gel for several hours according to the aging time. The gel was dried at 383 K for 24 h to solidification. The dried sample was calcined at 823 K in flowing $N_2/O_2$ (70/30) with the total flow rate of 100 $cm^3min^{-1}$ for 4 h to obtain $TiO_2$ catalysts denoted as $TiO_{2(SG)}$-LW. The heating rate was controlled at 1.7 K $min^{-1}$. The prepared catalysts were characterized by techniques such as ; XRD and XANES.

(b) High water content (*H* = 200)

Titanium(IV)bis(ethyl acetoacetato)diisopropoxide 4.2435 g (0.01 mol) was added dropwise into a mixture of $H_2O$ 36.00 $cm^3$ (2.00 mol) which was acidified with conc. $HNO_3$ 1 $cm^3$ (0.09 mol) to pH 1.55. In this step, the yellow suspension has been observed since the beginning. The suspension was then stirred at 358 K for 1 h and dried at 383 K for 24 h. The dried sample was calcined at 823 K in flowing $N_2/O_2$ (70/30) with the total flow rate of 100 $cm^3 min^{-1}$ for 4 h to obtain $TiO_2$ catalysts denoted as $TiO_{2(SG)}$-HW. The heating rate was controlled at 1.7 K $min^{-1}$.

*- Hydrolysis effect : pH*

The preparation procedure was the same procedure as that described in Section 1.1.1(b) with the exception that conc. $HNO_3$ was added 2.00 $cm^3$ and 3.00 $cm^3$ for adjusting to pH 1.25 and 1.08, respectively.

1.1.2 Cerium deposited on $TiO_2$ by sol-gel method: Ce/$TiO_{2(SG)}$

*- Hydrolysis effect : Cerium precursor*

(a) Low water content (*H* = 4)

Titanium(IV)bis (ethyl acetoacetato)diisopropoxide as titanium precursor 4.2435 g (0.01 mol) was mixed with acetylacetone 0.715 g ( 7.15 mmol) and ethylene glycol 4.50 $cm^3$ (79 mmol) followed by the addition of cerium nitrate (or cerium acetylacetonate). The percentage weight of cerium to titanium was 8 and 30% w/w. The mixture was stirred to get homogeneous mixture. Water was added 0.71 g (0.04 mol) and stirred until the solution was clear. The solution was allowed to rest in an oven at 348 K to form gel for several hours according to the aging time. The gel was dried at 383 K for 24 h to solidification. The dried sample was calcined at 823 K in flowing $N_2/O_2$ (70/30) with the total flow rate of 100 $cm^3min^{-1}$ for 4 h to obtain Ce/$TiO_{2(SG)}$-LW catalysts. The heating rate was controlled at 1.7 K $min^{-1}$.

(b) High water content ($H$ = 200)

Titanium(IV)bis(ethyl acetoacetato)diisopropoxide 4.2435 g was added dropwise into a mixture of $H_2O$ 36.00 $cm^3$ and cerium nitrate (or cerium acetylacetonate) which was acidified with conc. $HNO_3$ 1.00 $cm^3$ to pH 1. In this step, the yellow suspension has been observed since the beginning. The suspension was then stirred at 358 K for 1 h and dried at 383 K for 24 h. The dried sample was calcined at 823 K in flowing $N_2/O_2$ (70/30) with the total flow rate of 100 $cm^3min^{-1}$ for 4 h to obtain Ce/$TiO_{2(SG)}$-HW catalysts. The heating rate was controlled at 1.7 K $min^{-1}$.

**Table 7** Number of mole (#mol) and weight percentages (%wt) of catalysts by sol-gel method.

| Catalysts | Ti | | Ce | | Water/Ti ratio ($H$, mol) |
|---|---|---|---|---|---|
| | #mol | %wt | #mol | %wt | |
| $TiO_{2(SG)}$-LW | 0.01 | 100 | - | - | 4 |
| $TiO_{2(SG)}$-HW<br>[$TiO_{2(SG)}$-HWpH 1.55] | 0.01 | 100 | - | - | 200 |
| $TiO_{2(SG)}$-HWpH 1.25 | 0.01 | 100 | - | - | 200 |
| $TiO_{2(SG)}$-HWpH 1.08 | 0.01 | 100 | - | - | 200 |
| 8%Ce/$TiO_{2(SG)}$-LW | 0.01 | 92 | 0.0003 | 8 | 4 |
| 8%Ce/$TiO_{2(SG)}$-HW | 0.01 | 92 | 0.0003 | 8 | 200 |
| 30%Ce/$TiO_{2(SG)}$-LW | 0.01 | 70 | 0.0015 | 30 | 4 |
| 30%Ce/$TiO_{2(SG)}$-HW | 0.01 | 70 | 0.0015 | 30 | 200 |

### 1.1.3 Characterization

*X-ray diffraction (XRD)*

X-ray diffraction experiments were performed using Philips X'Pert-MPD diffractometer. The X-ray produces from Cu $K_\alpha$ radiation ($\lambda$ = 1.540 Å), electron current of 30 mA with an accelerating voltage of 40 kV. The diffractometer is equipped with a curved graphite monochromator. A scanning step of 0.02 degree was used. The identification of crystalline phases is accomplished by comparing the measured results with JCPDS (Joint Committee on Powder Diffraction Standards) file numbers 75-1537, 78-1510 and 81-0792 for anatase $TiO_2$, rutile $TiO_2$ and $CeO_2$, respectively.

*X-ray absorption near edge structure (XANES) spectroscopy*

(a) Ti *K*-edge absorption

XANES spectra of the Ti *K*-edge were measured in transmission mode with a Ge (2 2 0) double crystals monochromator on Beam Line 8 at the Synchrotron Light Research Institute (SLRI). The electron beam energy in the storage ring was 1.2 GeV and the current decayed from 70.9 to 33.5 mA. Data were collected using a 10 cm ion-chamber filled with $N_2$ at 63 for Ti *K*-edge. The spectral acquisition ranges were 4940 to 5040 eV for Ti *K*-edge at intervals of 0.2 eV. The data accumulation time was 1 s/step for powder samples which were prepared by depositing on polyimide film. The absorption edge energies were calibrated using Ti foil for Ti *K*-edge at 4966 eV.

(b) Ce $L_3$ edge absorption

X-ray absorption at the Ce $L_3$-edge in Ce/$TiO_2$ catalysts were measured in transmission mode with a Ge (2 2 0) double crystals monochromator on Beam Line 8 at SLRI. The absorption edge energies were calibrated using $CeO_2$ reference for Ce

$L_3$-edge at 5731.5 eV. The pressure in the chamber was 87 kPa $N_2$. The spectral acquisition ranges were 5625 to 5900 eV for Ce $L_3$-edge at intervals of 0.2 eV.

*Extended X-ray adsorption fine structures spectroscopy (EXAFS)*

EXAFS spectra of Ce $L_3$-edge were performed the same way as that described for XANES spectra in section 1.1.3 (b). The spectra were measured in energy range 5600 to 6140 eV.

*XANES analysis method*

(i) Ti *K*-edge

The X-ray absorption spectra were recorded from XASAvg (MATLAB modified by W.Kylsuban) showing data in 7 columns. The raw data the 7 columns data file were converted into a XASAvg (.ave) file that can be accessed by PROCESS for data analysis. This conversion worked by running a session of PROCESS and entering a sequence of keystrokes that were listed in prepave.keystroke. The prepave.keystroke file was saved into the folder which was the same as the data file and was modified by a text editor. If there are many spectra, the average command is used to combine the spectra. The modified absorption spectra were normalized with background subtraction.

(ii) Ce $L_3$-edge

X-ray absorption spectra of Ce $L_3$-edge were analyzed the same way as that described for Ti *K*-edge absorption, in Section 1.1.3 (i).

*EXAFS analysis method*

To obtain the normalized data, first, X-ray absorption spectra were proceeded with the XANES analysis (section 1.1.3 -i). Second, the experimental data were extracted and analyzed using the *EXAFSPAK* software package. The measured X-ray absorption spectra [Figure 17(a)] below the pre-edge region were fitted to a polynomial function [Figure 17(b)]. The polynomial were extrapolated over the entire energy region and subtracted from the total absorption spectra. The subtracted background spectra were normalized [Figure 17(c)]. The normalized $k^3$-weight EXAFS spectra were Fourier transformed to reveal the contribution of neighboring atoms.

Third, the measured spectra were compared to theoretical simulations. To generate these theoretical spectra, first principles calculations (done using the VASP ab initio package and described elsewhere, M. F. Smith, unpublished) were first carried out in order to determine the (locally distorted) $TiO_2$ crystal structure in the vicinity of a Ce defect. Once the positions of the Ti and O atoms surrounding the Ce defect were thus determined, the FEFF7 code was used to calculate the expected EXAFS spectrum.

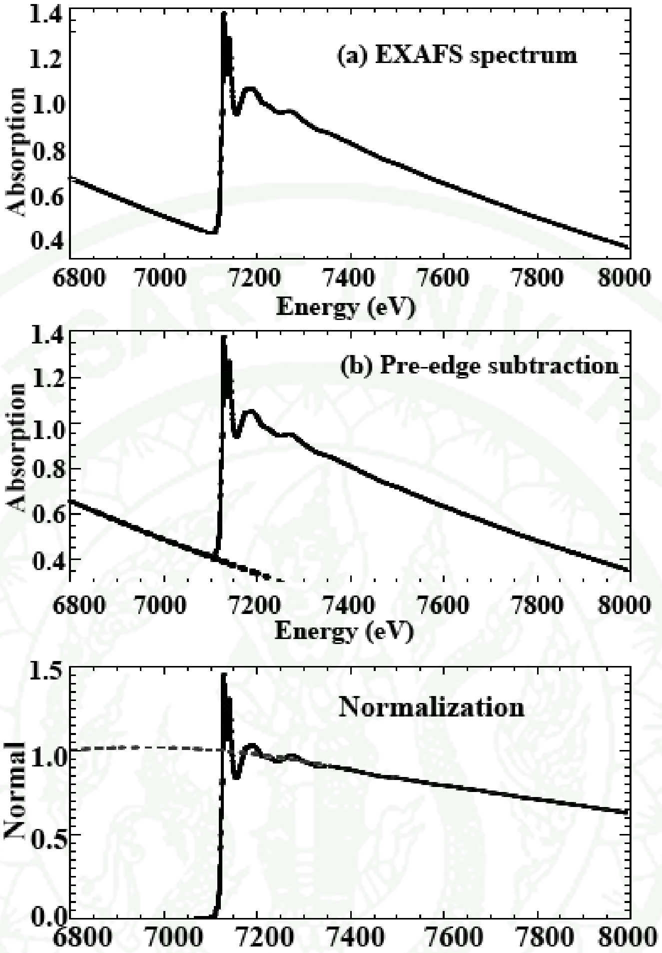

**Figure 17** Example of EXAFS data analysis (a) X-ray absorption spectrum, (b) Pre-edge subtraction and (c) Normalization.

**Source :** George and Pickering (1993).

1.2 Preparations and characterizations of modified cobalt catalysts: $Co_{SG}$-$Ce_{SG}$/$SiO_2$ (aerosil), $Co_{CP}$-$Ce_{CP}$/$TiO_2$ (anatase) and $Co_{CP}$/Ce-$TiO_{2(SG)}$

1.2.1 Preparation of cobalt and cerium by a sol-gel (citric acid) method deposited on $SiO_2$(aerosil): $Co_{SG}$ -$Ce_{SG}$ / $SiO_2$ (aerosil)

Cobalt nitrate 14.82 g was dissolved in water 25 $cm^3$and Ceriumn nitrate 1.31 g also was dissolved in 25 $cm^3$ water. Cobalt solution mixed with cerium solution in the round bottom flask. Citric acid 2.1611 g and $SiO_2$ Aerosil 200 3.00 g were added in the flask. The mixture was refluxed and ethylene glycol 16.5 $cm^3$ was dropped when the mixture was heated up to 363 K. Kept the temperature 363 K for 3 h. After that, the solution was heated at 363 K in air and stirred until gel was formed. The catalyst was dried at 383 K for 24 h and calcined at 473 K for 2 h and ramped to 823 K with a heating rate of 2 K. $min^{-1}$ , hold 2 h in Ar 40 $cm^3min^{-1}$, of which moles and weight percentages are listed in Table 8.

### 1.2.2 Preparation of cobalt and cerium by a co-precipitation method deposited on $TiO_2$(anatase): $Co_{CP}$-$Ce_{CP}$/$TiO_2$(anatase)

Ce promoted Co/$TiO_2$ (anatase) catalysts were prepared from suspension of titanium(IV) oxide (Aldrich, anatase ≥99%) mixed with cobalt(II) nitrate hexahydrate 0.9867 g and cerium (III) nitrate hexahydrate 0.0626 g in 20.00 $cm^3$ deionized water. $Co(OH)_2$ and $Ce(OH)_3$ were precipitated by $NH_3$ solution at pH 7.9 ± 0.2 under vigorous stirring. Then, the suspension was filtered off and washed with hot DI water. The filtered solid was washed and dried at 383 K in an oven. The prepared catalyst was calcined at 823 K for 2 h with ramp rate of 2.0 K/min in flowing argon with the flow rate of 40 $cm^3$/min. The sample is denoted as $Co_{CP}$-$Co_{CP}$/$TiO_2$ (anatase) with moles and weight percentages listed in Table 8.

### 1.2.3 Preparation of cobalt by a co-precipitation method deposited on Ce-$TiO_{2(SG)}$: $Co_{CP}$/Ce-$TiO_{2(SG)}$

Cerium promoted $TiO_2$ support [denoted: Ce-$TiO_{2(SG)}$] was prepared with low water content, the same method as that described in Section 1.1.2. The prepared catalyst was ground and sieved to 150 micron.

Cobalt based on the sieved Ce/$TiO_{2(SG)}$ was prepared by the co-precipitation, the same method as that described in Section 1.2.2. $Co(OH)_2$ was precipitated by $NH_3$

solution at pH 7.9 ± 0.2. Then, the suspension was filtered off, washed and dried at 383 K. The catalyst was calcined at 823 K for 2 h in Ar (40 $cm^3$/min) to obtain the sample denoted as $Co_{CP}$/Ce-$TiO_{2(SG)}$ (anatase), with moles and weight percentages listed in Table 8.

**Table 8** Number of mole (#mol) and weight percentages (%wt) of the modified cobalt catalysts.

| Catalysts | Co | | $TiO_2$ or $SiO_2$ | | Ce | |
|---|---|---|---|---|---|---|
| | #mmol | %wt | #mmol | %wt | #mmol | %wt |
| $Co_{SG}$-$Ce_{SG}$ / $SiO_2$ (aerosil) | 50.90 | 46.73 | 50.10 | 46.73 | 3.00 | 6.54 |
| $Co_{CP}$-$Ce_{CP}$/$TiO_2$(anatase) | 3.40 | 10.00 | 37.50 | 89.00 | 0.10 | 1.00 |
| $Co_{CP}$/Ce-$TiO_{2(SG)}$ | 1.00 | 10.00 | 8.33 | 89.00 | 0.03 | 1.00 |

### 1.2.5 Characterizations

*X-ray diffraction (XRD)*

The XRD measurement of Ce promoted $TiO_2$, Co/$TiO_2$ and Co/$SiO_2$ catalysts were performed in the same ways as that described for $TiO_2$ characterization, in Section 1.2.1.

*Temperature Programmed Reduction (TPR)*

TPR was used to determine the reduction behaviors of the samples. Each experiment was carried out with 20 mg of a sample and temperature rate was started from 35 to 950 ◦C at 10 ◦$Cmin^{-1}$. Carrier gas was 5% $H_2$ in $N_2$ with the flowrate of 20 $cm^3$/min. A thermal conductivity detector (TCD) was used to determine the amount of $H_2$ consumed during TPR experiment.

## 2. Fischer-Tropsch Experimental

The FT experimental is devided into 2 main parts as follows:

2.1 Fischer-Tropsch products analysis:
Testing of instantaneous products analysis using model substances

2.2 Fischer-Tropsch synthesis
  2.2.1 Testing of reactor set up I
  2.2.2 Testing of reactor set up II
  2.2.3 Testing of FT synthesis

### 2.1 Fischer-Tropsch products analysis:
### Testing of instantaneous products analysis using model substances

The model product substance is used for testing the efficiency of the analysis system by collecting the products in gas phase.

As the experimental set up shown in Figure 13, $N_2$ carrier gas (flow rate 70.00 $cm^3$/min) mixed with $CH_4$ (flow rate 2.00 and 5.00 $cm^3$/min) were kept in vacuum ampoules with purging 10 seconds and collecting 20 seconds as the background ampoules. Gasoline 95 was warmed at 30 $^oC$, mixed with $N_2$ as carrier gas (flow rate 70.00 $cm^3$/min) and $CH_4$ (flow rate 2.00 and 5.00 $cm^3$/min). The vapors were kept in vacuum ampoules with purging 10 seconds and collecting 20 seconds as the sample ampoules. Diesel was heated at 60 $^oC$, mixed with $N_2$ as carrier gas (flow rate 20.00 $cm^3$/min) and $CH_4$ (flow rate 5.00 $cm^3$/min). The vapors were also kept in vacuum ampoules with purging 10 seconds and collecting 20 seconds as the sample ampoules. The collected ampoules were analyzed by GC with SilicaPLOT and Flame ionization detector (FID) connected with the ampoule breaker. The column oven condition; 30$^o$C-225$^o$C (GC condition I, set up I and II) was compared with the column oven condition (-80$^o$C)-225$^o$C (GC condition II, set up I and II).

*GC connected ampoule breaker set up I*

Gas Chromatograph (GC) Varian 3380 equipped with a FID and a TCD. The FT products in gas phase were separated by a CP-SilicaPLOT column (stationary phase: a bonded silica porous layer, 30m x 0.53 mm x 6.00 µm) connects with a CP-Molsieve column (stationary phase: 5Å Molecular sieve, 10m x 0.53 mm x 50.00 µm) by a LIVE-T-Switching valve. The first column is CP-SilicaPLOT for separation of hydrocarbons. The second one is CP-Molsieve 5A column for separation of permanent gases ($H_2$, $O_2$, CO, $CH_4$).

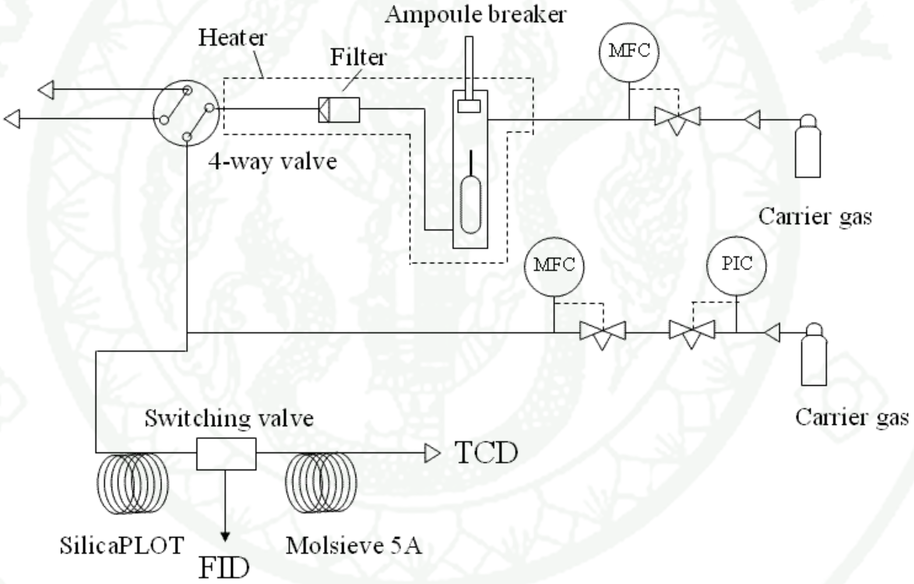

**Scheme 11** Configuration of GC connects to ampoule breaker.

*GC connected ampoule breaker set up II*

Gas Chromatography (GC) Varian 3800 equipped with FID and DB-1 column (polymethylsiloxane, 105m x 0.535mm x 5.00µm) to separate hydrocarbon compounds.

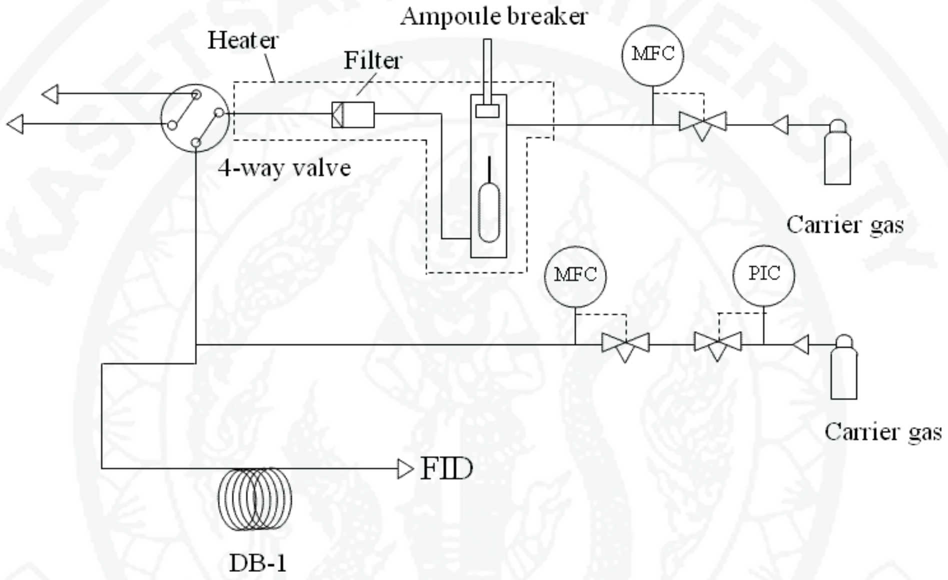

**Scheme 12** GC connected ampoule breaker set up II.

*Gas chromatographic condition*

A quantitative analysis of the hydrocarbon FT products in the gas phase ($C_1$-$C_{20+}$) was carried out using a Gas Chromatograph equipped with FID and modified with the ampoule breaker. The $N_2$ carrier gas led the hydrocarbon products and cyclopropane to the GC column. The GC condition is shown in Table 9.

**Table 9** Gas chromatographic analysis condition.

*GC set up I condition I:*

| | |
|---|---|
| Column oven | 30 °C hold 5 min – 225 °C (rate 3 °C/min) hold 10 min |
| Columns : | |
| Stationary phase | CP-SilicaPLOT (a bonded silica porous layer, 30m x 0.53 mm x 6.00 µm) |

*GC set up I condition II:*

| | |
|---|---|
| Column oven | -80 °C hold 3.5 min<br>rate 15 °C/min; -35 °C hold 3.5 min<br>rate 10 °C/min; -5 °C hold 2.0 min<br>rate 2 °C/min; 25 °C<br>rate 2 °C/min; 225 °C hold 10 min |
| Columns : | |
| Stationary phases | CP-SilicaPLOT (a bonded silica porous layer, 30m x 0.53 mm x 6.00 µm) |

*GC set up II condition I:*

| | |
|---|---|
| Column oven | -60 °C hold 5.08 min<br>rate 15 °C/min; -35 °C hold 3.5 min<br>rate 10 °C/min; -5 °C hold 2.0 min<br>rate 2 °C/min; 25 °C<br>rate 2 °C/min; 225 °C hold 10 min |
| Columns : | |
| Stationary phases | DB-1 (polymethylsiloxane, 105 m x 0.535 mm x 5.00 µm) |

*Calibration of methane/cyclopropane ratio*

The ampoules of 0.5% cyclopropane (CPr) in $N_2$ and methane ($CH_4$, purity 99.99%) mixture were collected with the ampoule sampler. First, the optimization ratio of 0.5%CPr/$CH_4$ mixture is investigated by collecting different ratios of CPr and $CH_4$ in the ampoules at 1 bar and room temperature. These ampoules were analyzed using GC with DB-1 column and FID (GC set up II condition I). $N_2$, as the carrier gas, flows at 10 $cm^3$/min. Next, the optimized ratio will be used to collect the ampoule to make the calibration curve for $CH_4$/CPr ratio.

Relative standard deviation (RSD)

The relative standard deviation is a measurement of the precision of the method by demonstrating the relative standard deviation for repeatability and reproducibility. It can be calculated with the formula:

$$SD = \sqrt{\frac{(x_1 - \bar{x})^2 + (x_2 - \bar{x})^2 + \ldots}{n-1}}$$

whereas

x = the sample

$\bar{x}$ = the average of samples

n = number of the sample

$$RSD = \frac{SD}{\bar{x}}$$

The relative standard deviation is often expressed in percent as the following:

$$\%RSD = \frac{SD}{\bar{x}} * 100$$

## 2.2 Fischer-Tropsch synthesis

### 2.2.1 Testing of reactor set up I

Before starting FT synthesis, the reaction line was tested with pressurized Ar to ensure that there was no leak. The catalyst was calcined and was reduced *in-situ* in order to activate the catalysts in the fixed-bed reactor. Cobalt catalyst, usually in the structure of $Co_3O_4$, was necessary reduced to metallic cobalt active site. The calcinations of each catalyst were under Ar 40.00 $cm^3$/min at 1 bar. The temperature program of the furnace was $2^oC$/min from 30 $^oC$ to the same temperature of the reduction condition and hold for 2 h or until $H_2O$ was not detected. For the *in-situ* reduction condition, the mixture of $H_2/Ar = 10/30$ $cm^3$/min at 1 bar was switched to the reactor. The reactor was heated up to the reduction temperature at 700 $^oC$ for cobalt based on $SiO_2$, according to the TPR data. The reference gases passed through a cold trap ($H_2O$ absorber) and exhaust.

**Table 10** Calcination and reduction conditions of the FT catalyst.

| Procedure | Gas | Temperature program | | | | | |
|---|---|---|---|---|---|---|---|
| | | flow rate ($cm^3$/min) | P (bar) | $T_{start}$ ($^oC$) | rate ($^oC$/min) | $T_{end}$ ($^oC$) | Time (h) |
| Calcination | Ar | 40 | 1 | 30 | 2 | 550 or 700 | 2 |
| Reduction | $H_2$/Ar (1/3) | 40 | 1 | 30 | 2 | 550 or 700 | 7 |

### 2.2.2 Testing of reactor set up II

The method is the same as that described in Section 2.2.1.

### 2.2.3 Testing of Fischer-Tropsch synthesis using $Co_{CP}$-$Ce_{CP}$/$SiO_2$(aerosil) with reactor set up II

At the end of the reduction, the reactor was cooled down to the desired reaction temperature at 190 °C and pressure was increased to the reaction pressure at 5 bar. The syngas ($H_2$/CO = 2) were introduced through the bypass, while Ar was introduced through the reactor for stabilizing the reaction condition. The syngases were collected into the ampoules and analyzed for the starting compounds. To begin the FT synthesis, the 4-way valve was switched from bypass into the reactor with the gas hour space velocity (GHSV) of 300 $h^{-1}$. This moment was defined as the start of the reaction (t = 0). During the reaction, the gas product streams were taken into ampoules. Then, the ampoules were analyzed by the GC equipped with the ampoule breaker. Each reaction part was heated at the set up temperature below:

| | |
|---|---|
| Reactor furnace | 180 - 190 $^oC$ |
| Hot trap | 160 - 170 $^oC$ |
| Needle valve | 220 - 230 $^oC$ |
| Reaction line | 220 - 230 $^oC$ |
| Ampoule sampler | 220 - 230 $^oC$ |

After the period of 10 hours, the syngases were replaced with Ar and subsequently the catalysts were cooled down to room temperature.

<u>Calculation of Gas hour space velocity (GHSV)</u>

Formula : $$GHSV = \frac{\text{Volume of reactant (in gas phase)}}{\text{Volume of catalyst}}$$

*Example :*

Condition : Pressure 5 bar
Temperature = 463 K
$H_2$/CO = 2
GHSV = 86 $h^{-1}$
Volume of catalyst (diluted with quartz particle) = 7 $cm^3$

$$86h^{-1} = \frac{\text{Volume of reactant (in gas phase)}}{7\ \text{cm}^3}$$

$\therefore$ Volume of reactant = 602 $cm^3/h$ = 0.60 $dm^3/h$

From PV = nRT

(5 bar) (0.60 $dm^3/h$) = n (0.082 $dm^3$ atm.$K^{-1}$.$mol^{-1}$)(463 K)

n = 0.08 mol/h

$2H_2 + CO$ = 0.08 mol/h

CO = 0.03 mol/h

$H_2$ = 0.05 mol/h

CO ; density 1.25 $g/dm^3$ , MW 28 g/mol

$H_2$ ; density 0.08991 $g/dm^3$ , MW 2 g/mol

d = g /V

V = n * MW / d

$V_{CO}$ = (0.03 mol/h * 28 g/mol) / 1.25 $g/dm^3$

$\therefore$ $V_{CO}$ = 0.67 $dm^3/h$ = 0.67* 1000 /60 $cm^3/min$

= 11.17 $cm^3/min$

and $V_{H2}$ = (0.05 mol/h * 2 g/mol) / 0.08991 $g/dm^3$

$\therefore$ $V_{H2}$ = 1.11 $dm^3/h$ = 1.11 * 1000 / 60 $cm^3/min$

= 18.50 $cm^3/min$

Thus, the FT synthesis condition was as follows:

| | |
|---|---|
| $H_2$ flowrate: | 20 $cm^3/min$ |
| CO flowrate: | 10 $cm^3/min$ |
| GHSV: | 86 $h^{-1}$ |
| Pressure: | 5 bar |
| Temperature: | 463 K (190 $^oC$). |

The product analysis was performed by the existing instantaneous product stream analysis. Organic compounds and inorganic compounds in the gas phase were analyzed separately with two gas chromatographs equipped with two ampoule breakers.

# RESULTS AND DISCUSSION

## 1. Characterizations of catalyst supports: $TiO_{2(SG)}$ and Ce/$TiO_{2(SG)}$

### 1.1. $TiO_2$ by a sol-gel method: $TiO_{2(SG)}$

### 1.1.1 Hydrolysis effect ($H_2O$ / Ti ratio)

*XRD results*

XRD patterns of $TiO_2$-LW show that the sample is mainly composed of the anatase phase which gives the 2theta peaks at 25.33, 48.10 and 55.14 degree (JCPDS PDF No. 83-2243), see Fig 18a. The peaks associated with the rutile phase, i.e. 27.51, 36.16 and 54.46 degree (JCPDS PDF No. 78-1510), are also present with a lower intensity. For $TiO_2$-HW sample, the XRD pattern in Figure 18b shows higher intensities of the rutile peaks than those of the $TiO_2$-LW sample.

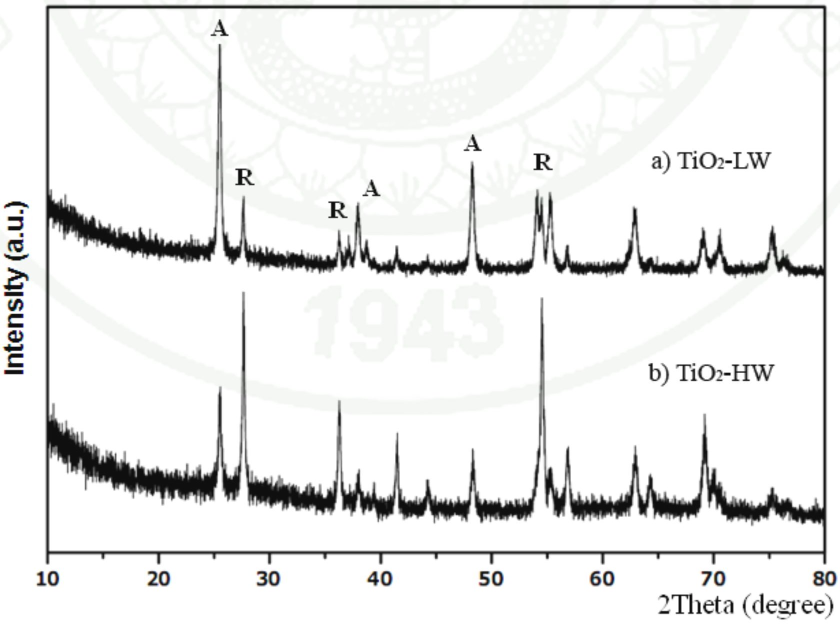

**Figure 18** XRD patterns of a) $TiO_2$-LW [$TiO_{2(SG)}$-LW] and b) $TiO_2$-HW[$TiO_{2(SG)}$-HW].

**Source** : Rattanakam (2005)

The XRD results indicate clearly that the water to alkoxide molar ratio has a strong effect on the structure of $TiO_2$. The sample prepared under low water condition has a higher ratio of anatase than that prepared under high water condition. When water is deficient, the hydrolysis of the alkoxide is incomplete, and linear oligomers are obtained. The mechanisms of $TiO_2$ formation with difference hydrolysis of the Ti-alkoxide were previously presented in details in the literatures (Gonzalez et al., 1997; Yu and Wang, 2000). When $H_2O$ is greater than stoichiometric ratio to the alkoxide, the hydrolysis approaches the completion. When the hydrolysis increases, it leads to highly branched polymeric products with highly cross-linkage which are likely to promote the formation of the rutile phase (Gonzalez *et al.*, 1997).

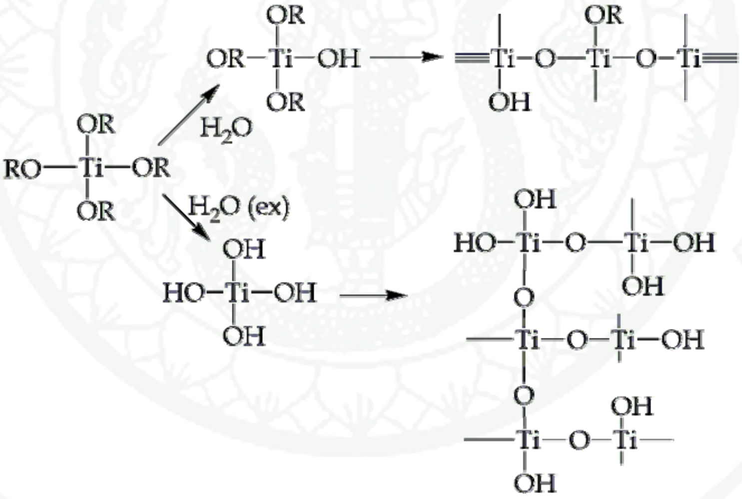

**Scheme 13** The hydrolysis process with low and high (excess) water contents.

*Ti K-edge XANES analysis*

X-ray absorption near edge spectra of $TiO_2$-rutile and -anatase reference were observed at Ti *K*-edge as shown in Figure 19.

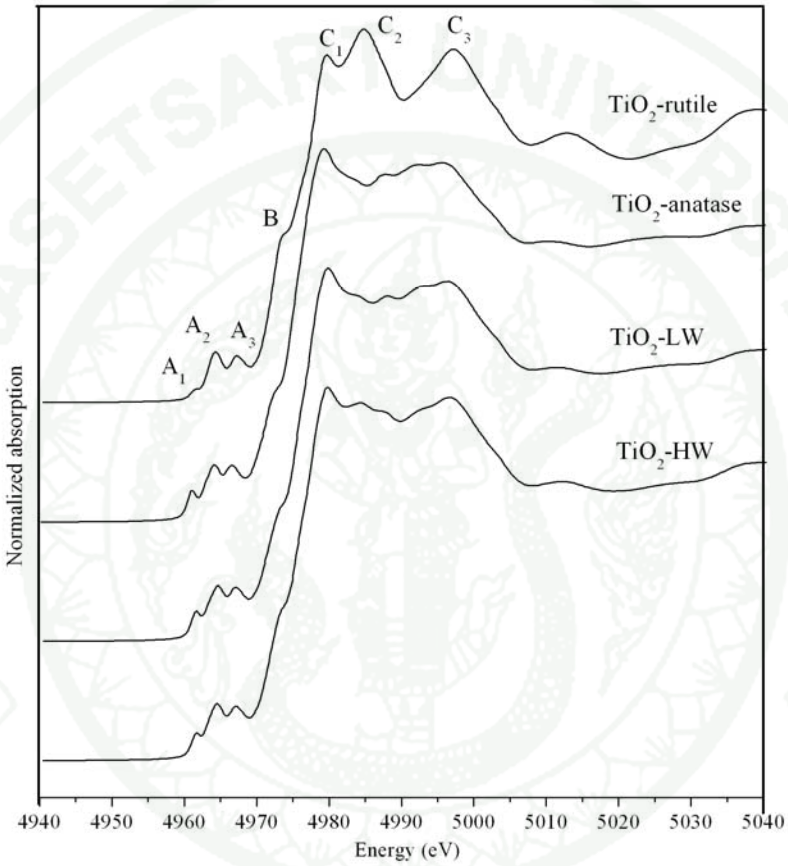

**Figure 19** Ti *K*-edge XANES of $TiO_2$-anatase, $TiO_2$-rutile, $TiO_2$-LW [$TiO_{2(SG)}$-LW] and $TiO_2$-HW [$TiO_{2(SG)}$-HW].

**Table 11** Pre-edge and edge position (eV) of rutile, anatase and samples at Ti *K*-edge.

| Samples | Position (eV) | | | | |
|---|---|---|---|---|---|
| | $A_1$ | $A_2$ | $A_3$ | B | $C_1$ |
| $TiO_2$-anatase | 4961.11 | 4964.15 | 4966.51 | 4976.50 | 4979.71 |
| $TiO_2$-rutile | - | 4964.34 | 4967.14 | 4976.13 | 4979.84 |
| $TiO_2$-LW | 4961.42 | 4964.49 | 4967.19 | 4974.39 | 4979.82 |
| $TiO_2$-HW | 4961.42 | 4964.62 | 4966.99 | 4974.59 | 4979.83 |

The X-ray absorption spectra at the Ti *K*-edge of $TiO_2$-anatase, $TiO_2$-rutile references and $TiO_2$ samples denoted as $TiO_2$-LW and $TiO_2$-HW. The allowed XANES transition for *K*-edge will be s to p orbital transition of 1s core electron. Ti, a 3d transition metal in the periodic table, has atomic number (Z) equal to 22 and electron configuration as $1s^2 2s^2 2p^6 3s^2 3p^6 3d^4 4s^0 4p^0$. The Ti *K*-edge XANES spectrum of $TiO_2$ composes of pre-edges features ($A_1$-$A_3$), a shoulder B, and main edge crests (C).

The absorption edge of Ti *K*-edge, composed of the dipolar transition 1s to 4p orbital appears as the shoulder B.

The pre-edge peak generally occur from the forbidden transition ($\Delta l \neq \pm 1$), Ti 1s energy level to Ti 3d level. A 1s to 3d transition is formally electric dipole forbidden but can gain intensity through either a quadrupole mechanism or through metal 4p mixing with the 3d orbitals, giving the transition electric dipole allowed character. The pre-edge features at the Ti *K*-edge for anatase $TiO_2$ with three fingerprint peaks ($A_1$, $A_2$ and $A_3$), are shown in Figure 19 (Top). The pre-edge feature attributed by a six-fold octahedral coordination. The first pre-edge ($A_1$) feature is mostly represent the quadrupolar transitions (2 order transition, $\Delta l = 2$) to *t2g* levels of the $TiO_6$ octahedron and the weak $A_1$ pre-edge magnitude attributed from 2 order allowed transition. The second pre-edge ($A_2$) is attributed to dipolar transition from Ti 1s to $t_{2g}$ of the neighboring octahedra around the octahedron containing the absorbing atom. (Chen *et al.*, 1997). The third pre-edge $A_3$ feature is attributed to another dipolar transition to $e_g$ orbital of the neighboring octahedral. The shoulders B of all samples are assigned to contribute mainly from the 1*s* to 4*p* transition. Farges *et al.* (1997) reported the calculations for rutile structure that feature $C_1$ edge crest is related to the presence of O and Ti next nearest neighbors around Ti. It is corresponded that XANES feature dominated by multiple-scattering (MS) resonance, which order n=4 relates to a MS path with up to four scattering along a Ti→O→Ti→O→Ti path within the tetrahedron (scattered two times by O first neighbors).

The XAS feature of rutile and anatase are different at the pre-edge and edge crest. The first A1 pre-edge of rutile show weaker intensity than that of anatase. Other, rutile appear the three edge crest ($C_1$-$C_3$).

XANES spectra at Ti *K*-edge of $TiO_2$-LW and $TiO_2$-HW samples are compared with anatase and rutile $TiO_2$ reference as shown in Figure 18. All spectra are normalized absorption and plotted on the same vertical scale. Both $TiO_2$-LW and $TiO_2$-HW show the anatase mixed with rutile-$TiO_2$ (pre-edge $A_1$-$A_3$ features for anatase and the shoulder at $C_1$-$C_3$ crests of rutile).

### 1.1.2 pH effect

The pH of prepared solution has a great influence on properties of $TiO_2$ nanoparticles. The effect of acidic solutions on the structure of $TiO_2$ is studied (Mahshid *et al.*, 2007).

### *XRD results*

Figure 20 shows XRD pattern of $TiO_2$-HW at different pH values as 1.55 ($TiO_2$-HWpH1.55), 1.25 ($TiO_2$-HWpH1.25) and 1.08 ($TiO_2$-HWpH1.08). The main peak at $2\theta$ = 25.4 and 27.5 degree represent the anatase phase and rutile phase, respectively. When pH values of the solution decrease, it is found that the rutile phase ratio clearly increases.

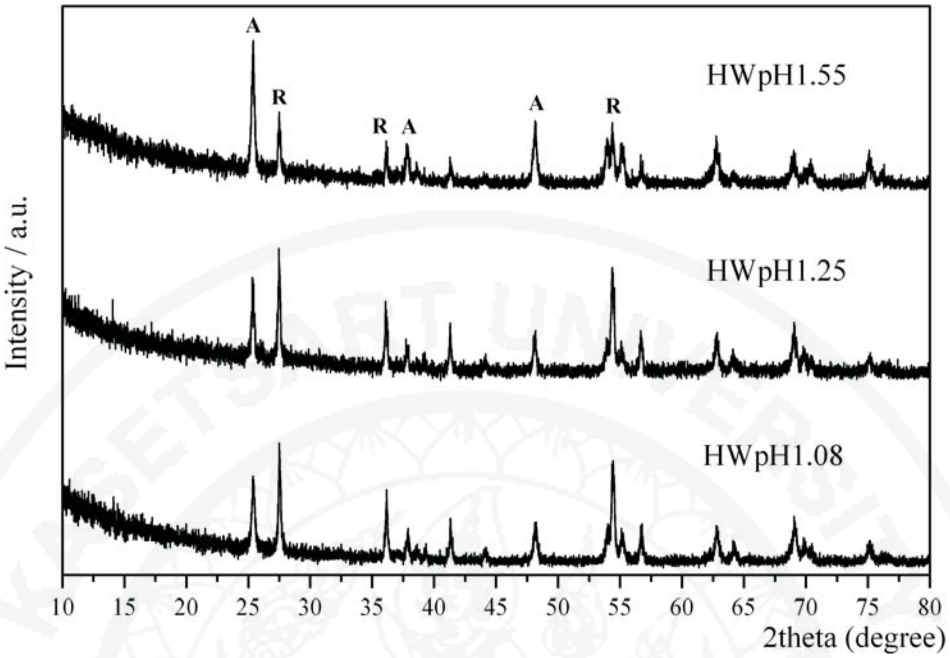

**Figure 20** XRD patterns of $TiO_2$-HWpH 1.55, $TiO_2$-HWpH1.25 and $TiO_2$-HWpH1.08.

The molar ratios of anatase to rutile has been determined by Spurr and Myer‘s method using the ratios of the most intense peaks of anatase (101) to rutile (110), as follows:

$W_R$ = $1/[1+0.8(I_A/I_R)]$ , $W_A = 1 - W_R$

whereas $W_A$ , $W_R$ : the mole fractions of anatase and rutile

$I_A$ : the peak intensities of anatase (101) , $2\theta = 25.3$ degree

$I_B$ : the peak intensities of rutile (110) , $2\theta = 27.5$ degree

Example : sample $TiO_2$-HW1.55

$W_R$ = $1 / [1+ 0.8(408/213]) = 0.3949$

$W_A$ = $1 - 0.3949 = 0.6051$

% rutile = $W_R$ x 100 = 0.3949 x 100 = 39.49%

% anatase = $W_A$ x 100 = 0.6051 x 100 = 60.51%

**Table 12** The molar percentages of anatase to rutile phase of $TiO_2$ with different pH.

| Samples | $2\theta_A$ | $I_A$ | $2\theta_R$ | $I_R$ | $W_R$ | $W_A$ | %R | %A |
|---|---|---|---|---|---|---|---|---|
| $TiO_2$-HWpH1.55 | 25.41 | 408 | 27.48 | 213 | 0.3949 | 0.6051 | 39.49 | 60.51 |
| $TiO_2$-HWpH1.25 | 25.38 | 278 | 27.47 | 360 | 0.6181 | 0.3819 | 61.81 | 38.19 |
| $TiO_2$-HWpH1.08 | 25.36 | 248 | 27.50 | 338 | 0.6301 | 0.3699 | 63.01 | 36.99 |

**Note** : A = anatase , R = rutile

The XRD results from Table 12 of the high water content ($H_2O$/alkoxide ratio) with different pH values occurred such that the intensity of the rutile structure increases with the increasing of acid concentration.

### *Ti K-edge XANES analysis*

The pH effect on the ratio of rutile and anatase $TiO_2$ structure is investigated using XANES at Ti *K*-edge as the results shown in Figure 21.

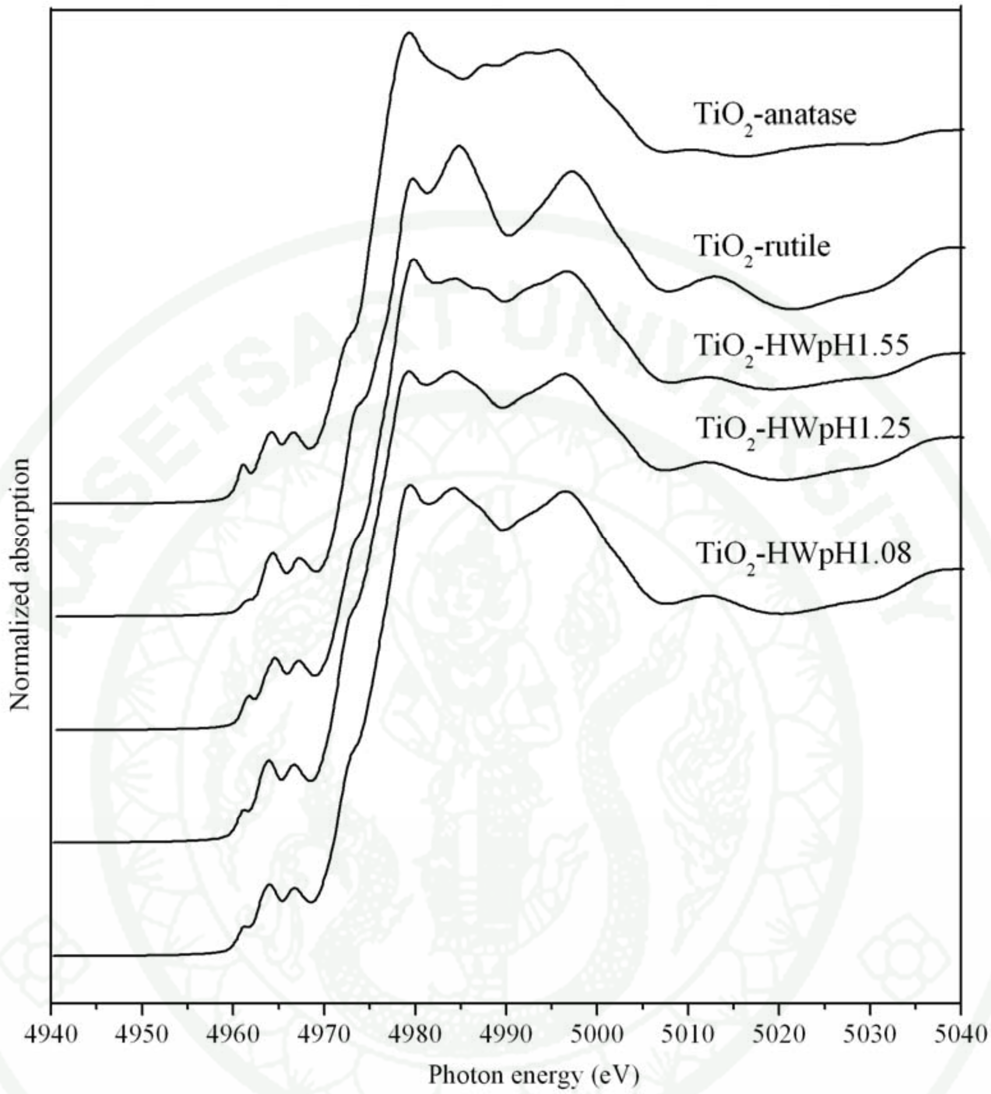

**Figure 21** Ti *K*-edge XANES of $TiO_2$ prepared with high water content at different pH solutions: $TiO_2$-HWpH1.08, $TiO_2$-HWpH1.25, $TiO_2$-HWpH1.55.

Edge region under consideration is between 4980 and 4990 eV of pH 1.25 and 1.08 show stronger shoulder than that of pH 1.55, which indicate higher ratio of rutile phase. In comparison of pH conditions, the phase transformation of the anatase to the rutile structure is increased in range 4980-5000 eV with decreasing the pH. In more acidic condition, the titanium alkoxide is hydrolyzed rapidly and subsequently polymerized to form the highly linked network, leading to the rutile structure.

It has been reported (Gonzalez *et al.*, 1997) for the case of $SiO_2$, that hydrolysis occurred rapidly and gel formation times were substantially increased under the strong acidic conditions. In this experiment, $HNO_3$ was used to control pH of the prepared sols. The mechanism was proposed as shown in Scheme 14. Alkoxide groups are rapidly protonated in the first step and pull electron away from titanium which makes titanium become more positive and thus more susceptible to be attacked by water with the elimination of ROH. The remaining negative anions ($NO_3^-$) from the acid attack the titanium atom and increase its coordination. Another alkoxide group acquires partial positive charge, which could be protonated and further elimination. This results in a transition state in which the removal of the alcohol group is facilitated. In the meantime, the hydrolysis can also take place through the M-X bonds of the transition state species.

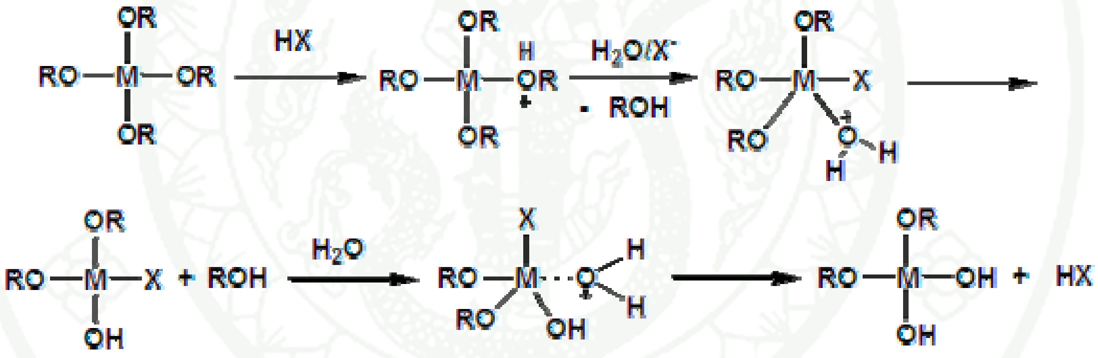

**Scheme 14** Mechanism of hydrolysis via M-X bonds.

The results of XANES spectra of Ti K-edge agree with XRD results, indicate that the hydrolysis effect with acidic condition has a strong effect on the rutile and anatase structure of $TiO_2$.

### 1.2 Cerium deposited on $TiO_2$ by a sol-gel method: $Ce/TiO_{2(SG)}$

*Cerium precursor effect: Cerium acetylacetonate and Cerium nitrate*

The cerium precursor was changed from cerium nitrate (CN) to cerium acetylacetonate (CA), which was hydrolyzed less than cerium nitrate (CN).

*XRD results*

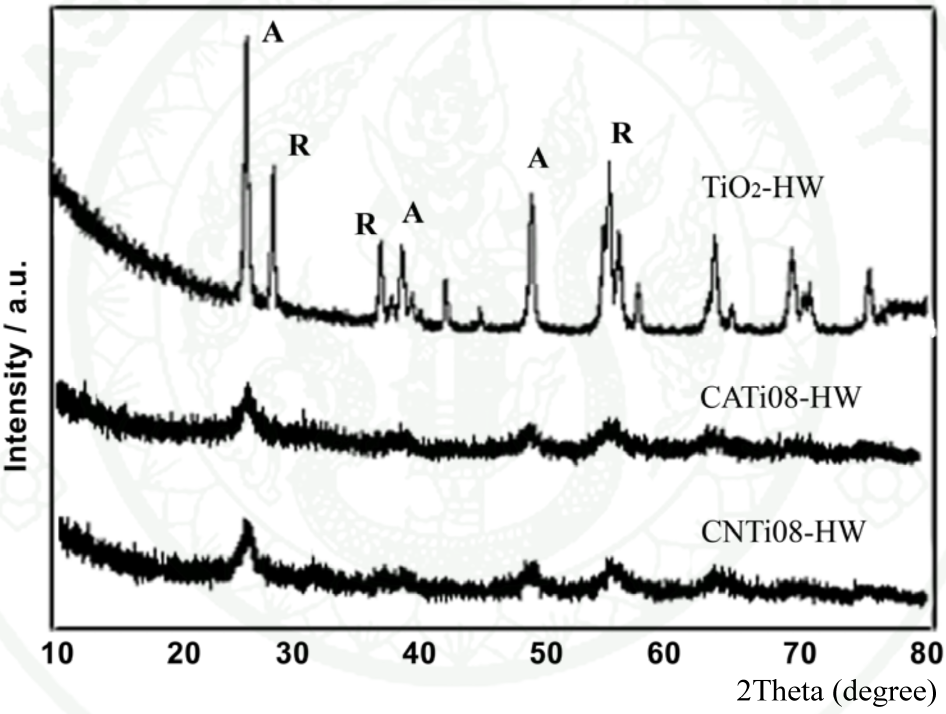

**Figure 22** XRD patterns of $TiO_2$-HW, CATi08-HW and CNTi08-HW.

Different cerium precursors ($Ce(acac)_3$ for CATi08-HW and $Ce(NO_3)_3$ for CNTi08-HW) were deposited with the same amount of cerium into the mixed phase $TiO_2$. The influence of cerium ions on the $TiO_2$ structure can be observed from the XRD patterns of the CATi08-HW and CNTi08-HW compared to that of $TiO_2$-HW in Figure 22. The two XRD patterns of the Ce-deposited samples are very similar and suggest that both samples composed of the anatase phase. However, when compare with the undeposited one ($TiO_2$-HW), it is evident that the diffraction peaks of the Ce-deposited samples are much broader. This implies that the particle size of the Ce-deposited samples is much smaller. Based on Scherrer equation (Patterson, 1939), the average particle size of Ce-deposited samples are estimated to be in the order of 10 nm or less, while the average particle size of the undeposited samples are in the order of 50 nm. We note that, from the XRD of Ce-deposited samples, it cannot be concluded that there is any rutile phase due to high noise level combining with the broad peaks. Similar behavior has been previously observed by Lin and Yu, 1998. They attributed the stability of the anatase phase to the formation of Ti-O-Ce bonds which inhibit the transformation of anatase to rutile.

*Raman spectroscopy*

The Raman shifts of samples: CATi08-HW, CNTi08-HW, rutile-$TiO_2$ (exhibited two characteristic peaks at 477 and 611 $cm^{-1}$) and anatase-$TiO_2$ (exhibited four characteristic peaks at 144, 395, 513, and 637 $cm^{-1}$), as shown in Figure 23. These peaks are consistent with the allowed modes of anatase-$TiO_2$ that are assigned as $E_g$ (144 $cm^{-1}$), $B_{1g}$ (395 $cm^{-1}$), $A_{1g}$ (513 $cm^{-1}$), and $E_g$ (637 $cm^{-1}$) (Sekiya *et al.*, 2001; Hu *et al.*, 2003). The lower energy peaks at 144 and 395 $cm^{-1}$ were assigned to the bending modes, whereas the high energy peaks at 513 and 637 $cm^{-1}$ were assigned to the anti-symmetric bond stretching and symmetric bond stretching modes (Rattanakam, 2005). The peak associated with the rutile-$TiO_2$ at 477 $cm^{-1}$ ($E_g$) and 611 $cm^{-1}$ ($A_{1g}$) (Swamy *et al.*, 2006) appears as only a weak shoulder around 612 $cm^{-1}$ for the Ce-deposited samples and totally disappeared in the anatase-$TiO_2$, as expected. This indicates that the Ce-deposited samples might contain at most only a small fraction of rutile phase. This is consistent with the assumption that the presence of Ce ions inhibits the transformation of anatase to rutile (Francisco and Mastelaro, 2002). Furthermore, if $CeO_2$ is formed, it should have a strong Raman peak, due to the characteristic fluorite structure, centering around 459 $cm^{-1}$ (Choi *et al.*, 2005; Francisco and Mastelaro, 2002). The peak was not observed in our Ce-deposited samples, indicating that there is no $CeO_2$ phase forming.

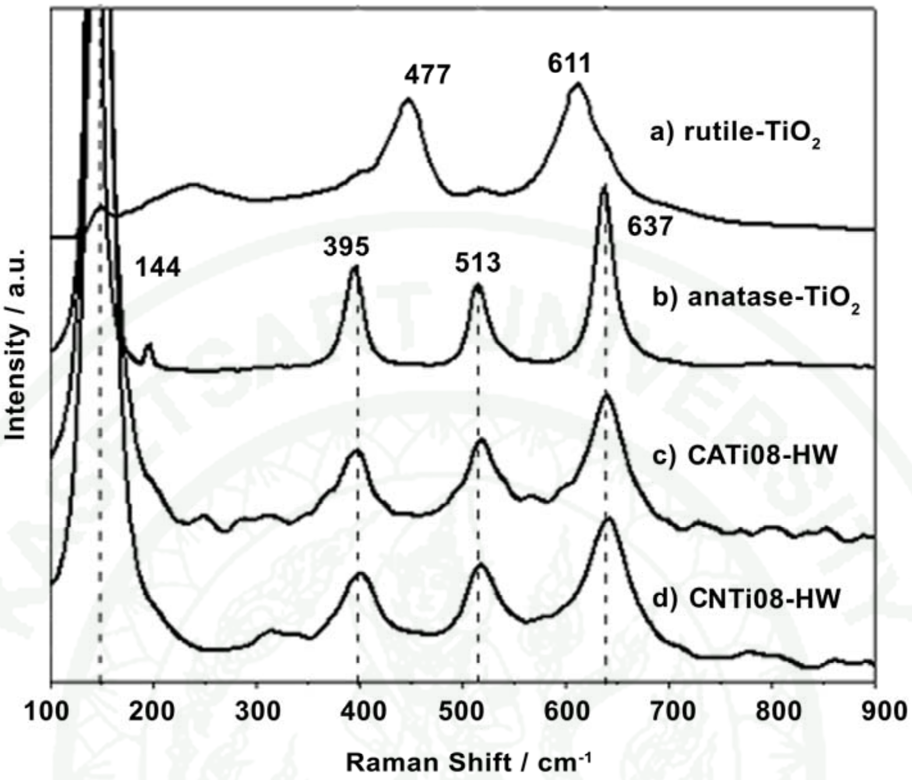

**Figure 23** Raman spectra of a) rutile-$TiO_2$, b) anatase-$TiO_2$, c) CATi08-HW and d) CNTi08-HW.

Comparison of the high and low cerium content prepare with the low water/alkoxide ratio e.g. CATi08-LW and CATi30-LW samples show the main features of the anatase $TiO_2$ reference (as shown in Figure 24 and Table 13). CATi08-LW and CATi30-LW samples are dominantly the anatase phase.

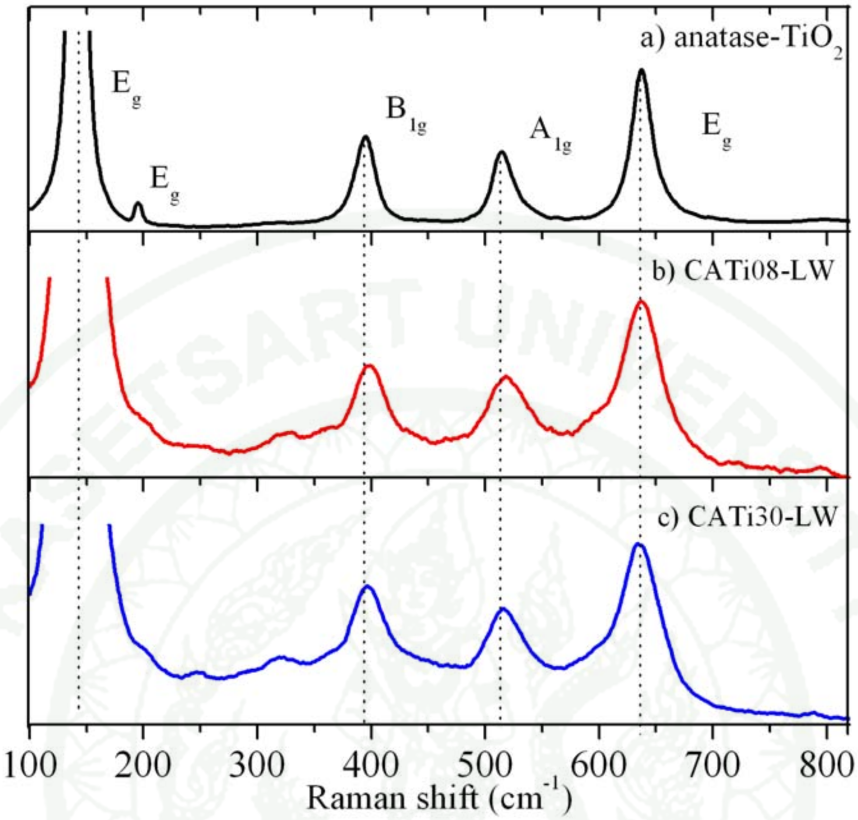

**Figure 24** Raman spectra of a) anatase $TiO_2$, b) CATi08-LW and c) CATi30-LW samples.

**Table 13** The Raman shift ($cm^{-1}$) of anatase $TiO_2$, CATi08-LW and CATi30-LW samples.

| Samples | Raman shift ($cm^{-1}$) | | | |
|---|---|---|---|---|
| | $E_g$ | $B_{1g}$ | $A_{1g}$ | $E_g$ |
| anatase $TiO_2$ | 144 | 395 | 513 | 637 |
| CATi08-LW | 144 | 397 | 516 | 636 |
| CATi30-LW | 143 | 396 | 515 | 634 |

*XANES*

*Ti K-edge analysis*

*- Low cerium content:8%Ce/$TiO_2$*

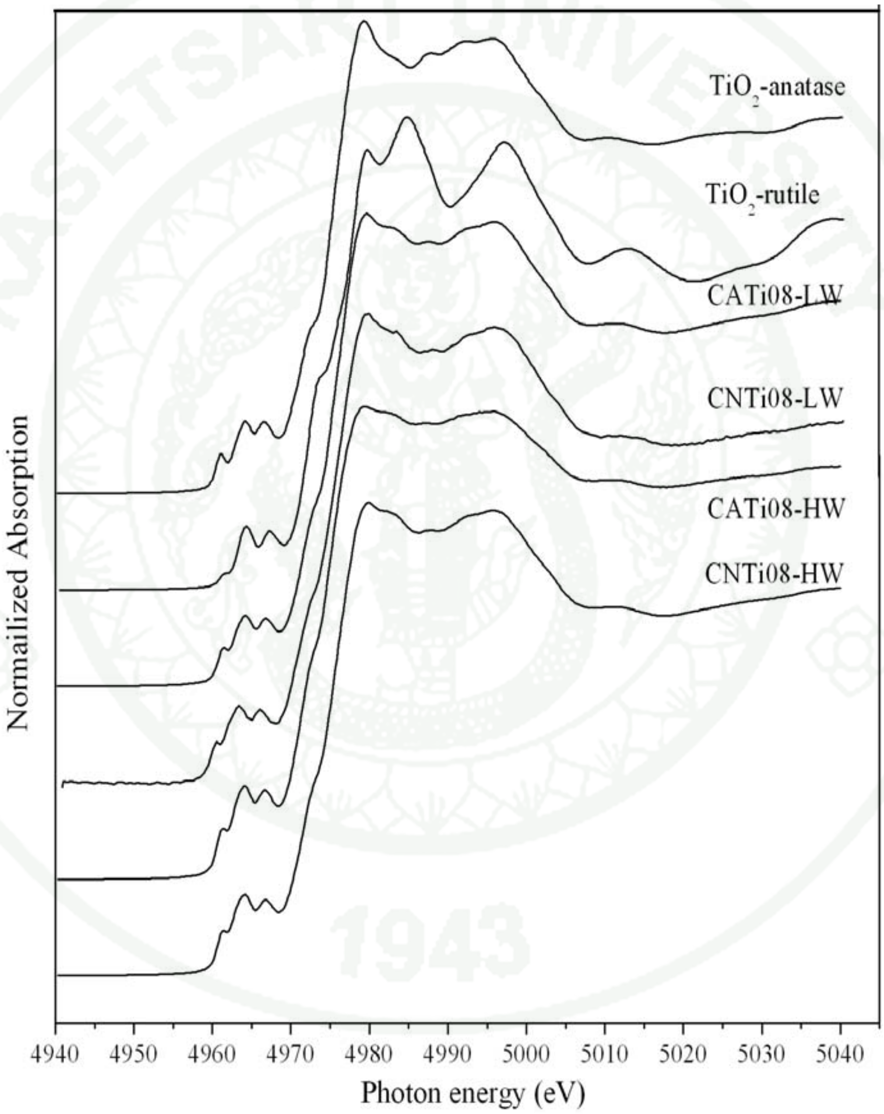

**Figure 25** Ti *K*-edge XANES spectra of 8%Ce/$TiO_2$ prepared with different cerium precursor (CA:Cerium aceactylacetonate, CN:Cerium nitrate) at low (LW) and high water content(HW).

Figure 25 shows that different Ce-precursors do not affect significantly $TiO_2$ phase structures. CATi08-LW and CNTi08-LW under low water content exhibit $TiO_2$ both anatase and rutile phase. CATi08-HW and CNTi08-HW under high water content also exhibit $TiO_2$ both anatase and rutile phase. In previous section, by using XRD technique, we cannot see the rutile peak in the CeATi08-HW and CeNTi08-HW samples because the XRD peaks are too broad.

XANES spectra can be concluded that the hydrolysis resulted from the low cerium percentages of cerium precursors [$Ce(acac)_3$ and $Ce(NO_3)_3$] did not show significant effect on the mixture phases.

It can be assumed that the low cerium content (8%Ce = 0.0003 mol) was hydrolysed with low water content ($H_2O$ = 0.04 mol), the hydrolysis of the cerium precursors and the Ti-alkoxide are in excess. The cerium species are hydrolyzed as cerium (III) ions and resides between Ti-O-Ti linkages in sol formation. They resides in the anatase structure as the interstitial defect. According to these results, the mechanism of sol gel process with low water content can be proposed as shown in Scheme 15.

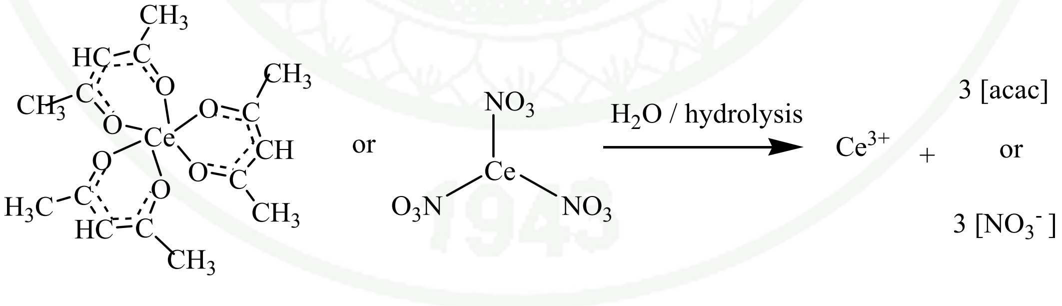

(a)

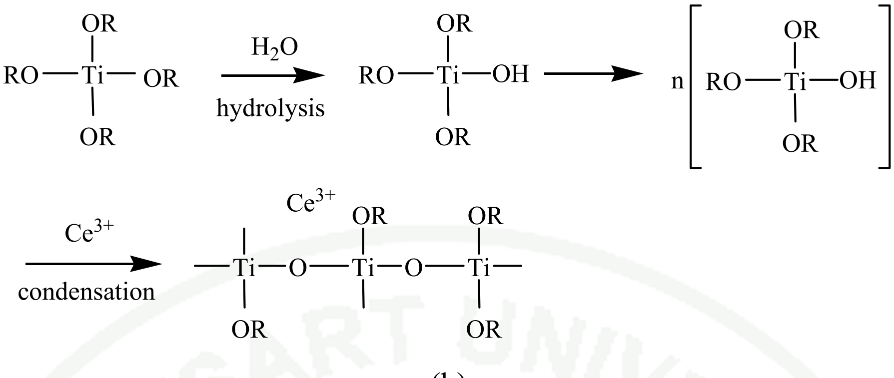

(b)

**Scheme 15** The proposed mechanism of the sol-gel process with low cerium precursor concentration in low water hydrolysis; (a) hydrolysis of cerium species, (b) hydrolysis and condensation of sol-gel process.

When water content is high ($H_2O$ = 2.00 mol), the hydrolyses of both the cerium precursors [Scheme 15(a)] and the Ti-alkoxide precursors approach the completion. It leads to highly branched polymeric products with highly cross-linkage which are likely to also promote the formation of the rutile phase. The cerium species as cerium (III) ions resides between Ti-O-Ti linkages in sol formation (Scheme 16), which subsequently become interstitial defect in the anatase structure after calcinations.

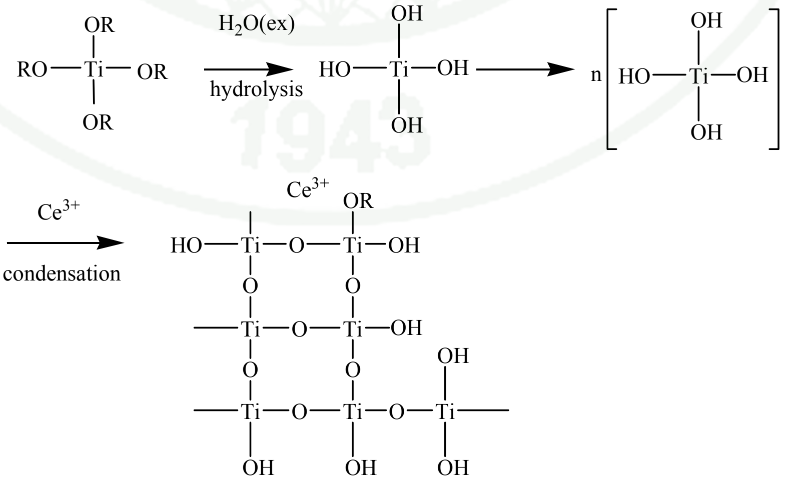

**Scheme 16** The proposed mechanism of the sol-gel process with low cerium precursor concentration in high water hydrolysis.

*High cerium content: 30%Ce/$TiO_2$*

*XRD results*

In Figure 26, XRD patterns of the catalysts with higher cerium content are denoted as CNTi30-LW and CATi30-LW. In the case of cerium acetylacetonate precursor (CATi30-LW), the anatase peaks did not appear whereas only anatase structure was observed in the XRD patterns from cerium nitrate precursors (CNTi30-LW).

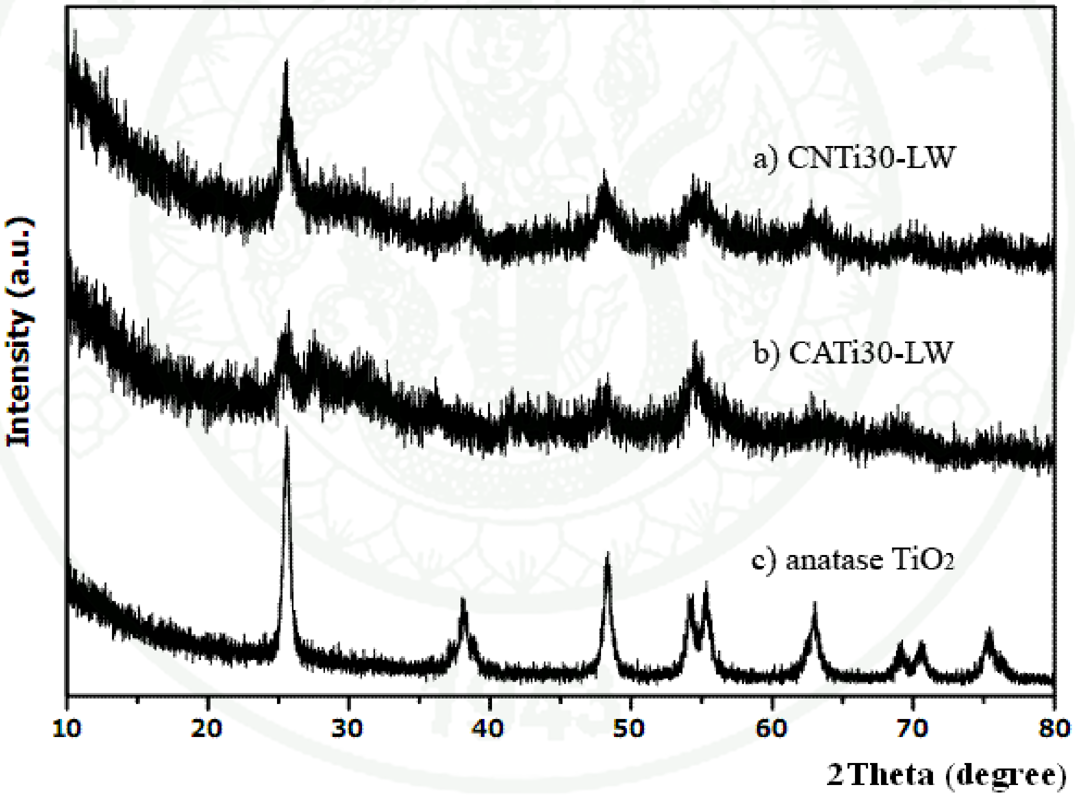

**Figure 26** XRD patterns of CNTi30-LW, CATi30-LW and $TiO_2$ anatase.

**Source** : Rattanakam (2005).

*XANES*

*Ti K-edge analysis*

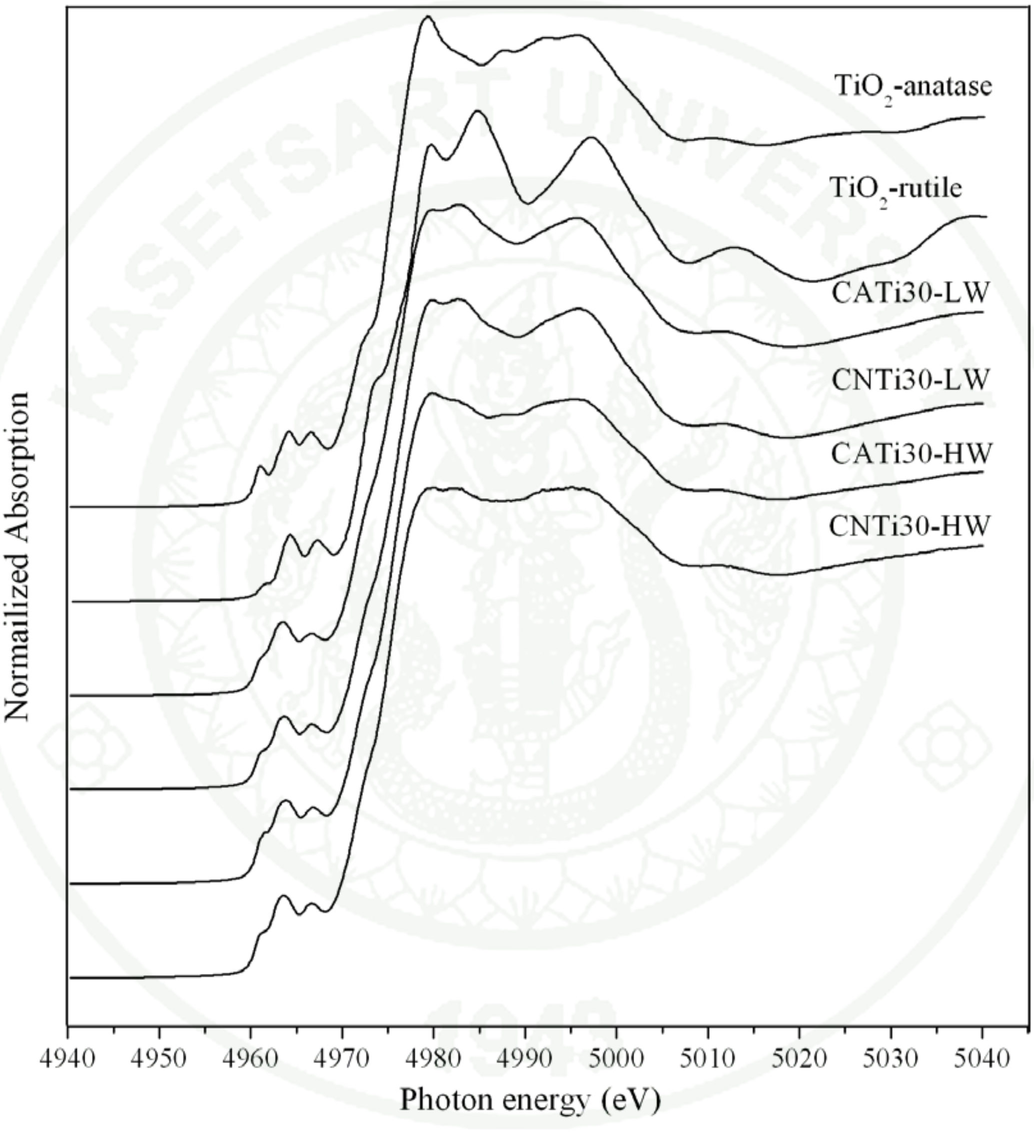

**Figure 27** XANES Ti K-edge spectra of 30%Ce/$TiO_2$ prepared with different cerium precursor (CA : Cerium Aceactylacetonate, CN : Cerium Nitrate) under low (LW) and high water content (HW).

Feature of pre-edge peaks of all samples trend to the rutile structure. Egde region range 4980 – 4990 eV, the high cerium content prepared from both methods

(LW and HW) exhibit both anatase and rutile features. Comparison of XANES with XRD results, XANES spectra clearly show the effect of cerium content to the $TiO_2$ structure and show the mixed phases of anatase and rutile in the $TiO_2$ structures.

*EXAFS analysis*

*Ce $L_3$-edge*

The experimental data were extracted and analyzed using the *EXAFSPAK* software package. The experimental spectra were compared with the theoretical simulations. To generate these theoretical spectra, first principles calculations (using the VASP *ab initio* package, M. F. Smith) were first carried out in order to determine the (locally distorted) $TiO_2$ crystal structure in the vicinity of Ce defect. Once the positions of the Ti and O atoms surrounding the Ce defect were thus determined, the FEFF7 code was used to calculate the expected EXAFS spectra.

*- Low cerium content: 8%Ce/$TiO_{2(SG)}$*

EXAFS data were considered in an energy interval 5625 – 5900 eV for $L_3$-edge analysis (at higher energies, the spectrum became too noisy to reliably analyze). The $L_3$-edge spectra of cerium showed a characteristic double-peak shape near the absorption edge as shown in Table 14 and Figure 28.

**Table 14** The energy peaks of 8%Ce/$TiO_{2(SG)}$ sample for Ce $L_3$ edge.

| Samples | Lower energy peak (eV) | Higher energy peak (eV) |
|---|---|---|
| CATi08-LW | 5730.05 | 5738.05 |
| CNTi08-LW | 5730.01 | 5738.21 |
| CNTi08-HW | 5729.99 | 5737.99 |

This double –peak shape is due to the mixed-valence behavior of Ce in its final state and the interaction between 4f orbitals of the metal and 2p orbitals of the ligands (oxygens) in its initial state (see, for e.g., Fonda 1999).

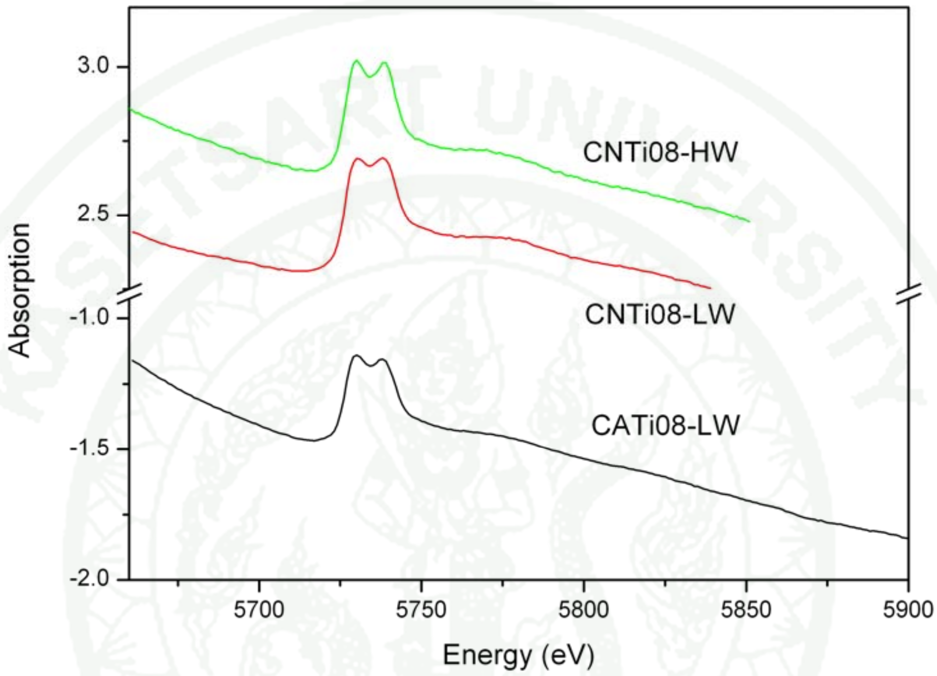

**Figure 28** Absorption spectra of $L_3$ edge of Ce in 8%Ce/$TiO_{2(SG)}$.

This mixed valence behavior complicates the analysis of the EXAFS spectra because there are, effectively, two absorption edges so that background subtraction cannot be done in the usual manner. It is not captured automatically by the first principles simulations of the absorption spectra, and therefore the second peak has to be added by hand. That is, the spectra are simulated twice, once for each absorption edge, and the results summed with some arbitrary relative weight. This crude procedure has been used previously (Fonda *et al.,* 1999). Below, the main results of the analysis are not sensitive to the manner in which the mixed valence behavior is treated.

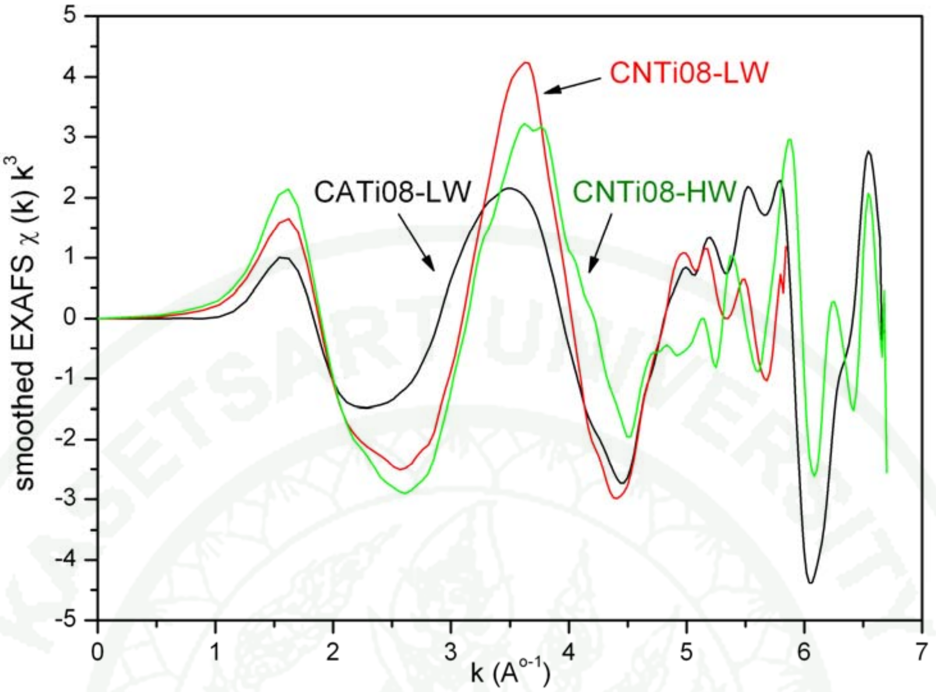

(a)

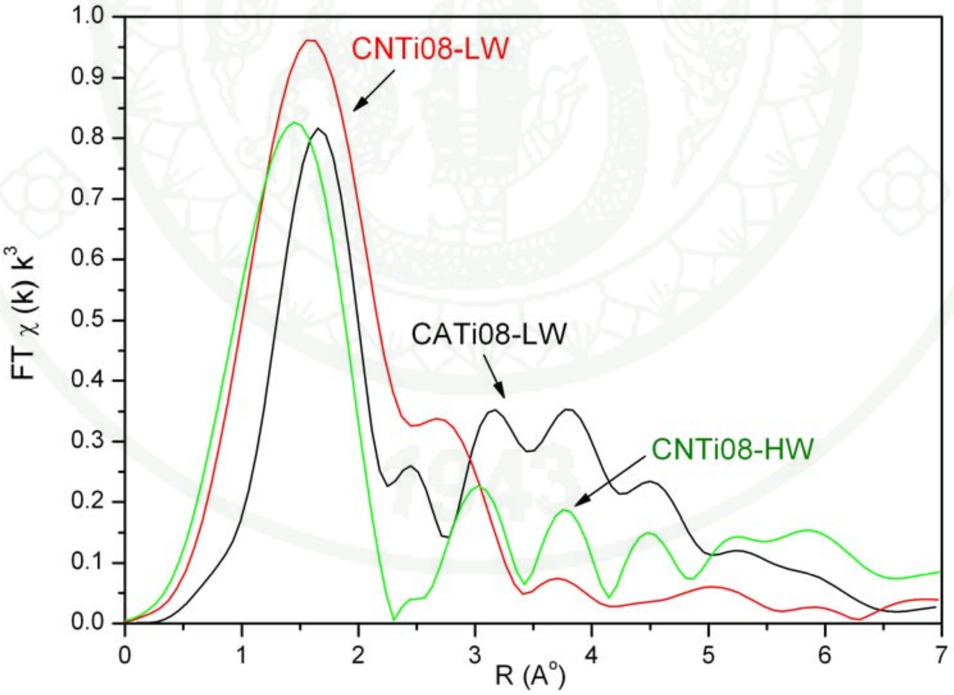

(b)

**Figure 29** Ce $L_3$-edge EXAFS spectra $\chi(k)k^3$ for 8%Ce/TiO$_{2(SG)}$ (a); EXAFS spectra, (b); Fourier transforms

Figure 29a shows EXAFS spectra of CATi08-LW, CNTi08-LW and CNTi08-HW. In Figure 29b, the magnitude of the Fourier transforms of the spectra are shown. The latter one was concentrated, since it is simpler to interpret. The peaks of the Fourier transforms spectra correspond to interatomic distances, i.e. each peak position corresponds to atoms at a given distance from the absorbing Ce, with the peak height being proportional to the number of atoms located at that distance. The actual bond lengths cannot be directly read off the graphs since phase corrections must first be made, nonetheless, there is a one-to-one correspondence between peaks and bond lengths. The spectra of all three samples have a prominent peak occurring slightly below 2 Å. The difference between the first-peak position of all spectra is ~ 0.2 Å (that is, the peak position associated with nearest neighbors. There is seen to have a difference in the peak heights, with the CNTi08-LW peak being roughly 20% higher than the other two). These differences are not especially large when one considers the noise in our data i.e. different background subtraction methods change things somewhat, and thus only qualitative differences in the data can be taken seriously. Indeed, within our experimental error, we cannot observe any difference in the local structure for the three samples.

Here, it may also be noted that a relatively narrow range in *k*-space (that is, a narrow energy range above the absorption threshold) are analyzed. Because of data at higher energy became increasingly noisy, and its inclusion would make the EXAFS spectra even more sensitive to background subtraction. The dependence of the spectra shown on the manner has been studied in which the background is subtracted and found that the position and height of the main peak remains roughly constant independent of the details of the subtraction.

Raman spectra of CATi08-LW CNTi08-LW and CNTi08-HW showed that the cerium atom resides as an interstitial defect in $TiO_2$. There is consideration of two defect sites for Ce in $TiO_2$: an interstitial site and the Ti-substitution site. For each Ce defect site, the local structure was determined and the EXAFS spectra simulated so that, upon comparing the results with the measured spectra, the most likely site for Ce occupation in each sample could be determined. (Other possible sites for Ce occupation, such as alternative interstitial positions or O-substitution are considered unlikely to occur, which is why we restrict our attention to the two sites mentioned.) In Figure 30 show an illustration of the local crystal structure surrounding the Ce atom in the two defect sites. The interstitial position is in the centre of the square formed by four Ti atoms.

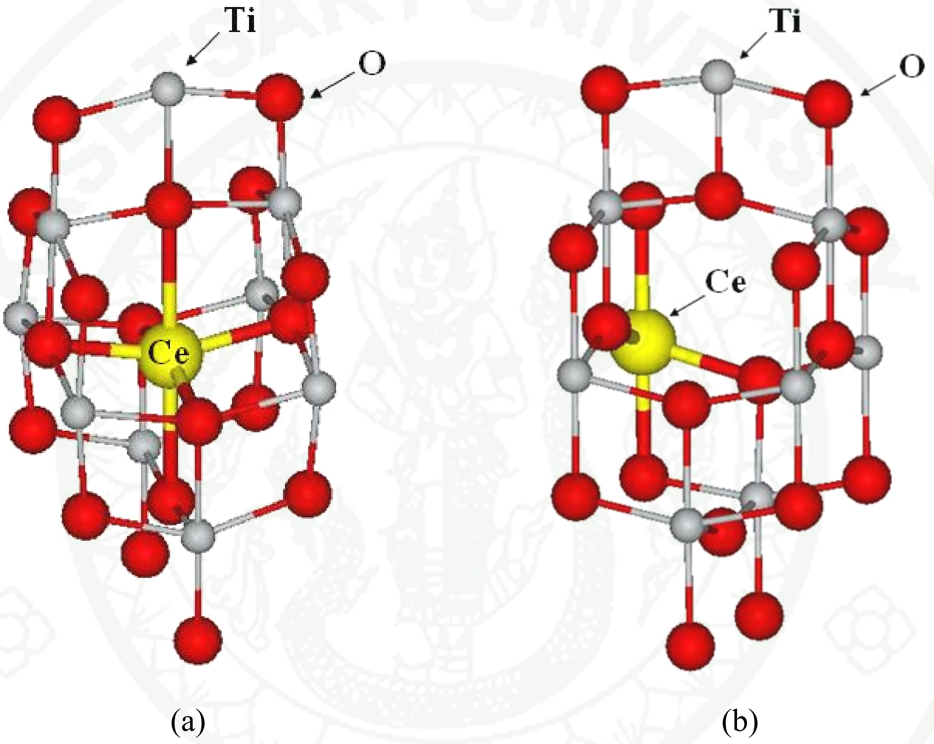

(a) (b)

**Figure 30** Models of Ce defects in anatase $TiO_2$. (a): Ce interstitial (b): Ce substitute for Ti. The Ce-O bonds are thick in the Figure. Note that for 30b, only four of the O neighbors are shown, the remaining two may be obtained using the 4-fold symmetry about the vertical axis through Ce.

This local structures have been obtained from first principles density functional theory, which were not adjusted in any way during attempts to fit the data. That is, the bond lengths between Ce and neighboring Ti and O were fixed to the values obtained theoretically. The EXAFS spectra, including contributions from single and multiple scattering paths, were then simulated using FEFF7.

First, a comparison between the two theoretical spectra, Ce-interstitial and Ce-Ti substitution so that qualitative differences are shown in Figure 31.

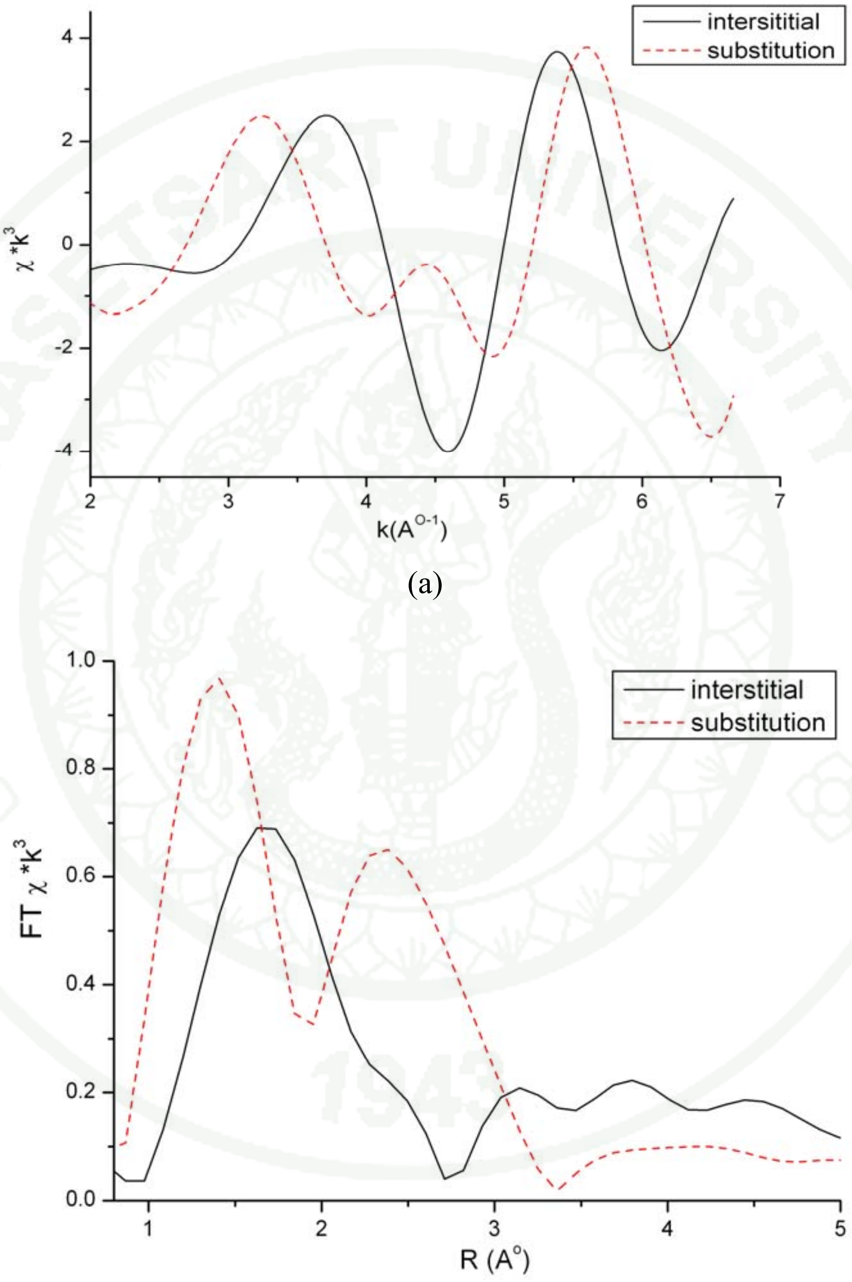

(a)

(b)

**Figure 31** Theory graphs of interstitial and substitution simulation.
(a); EXAFS spectra, (b) ; Fourier transforms

Looking first at Figure 31a, which shows the EXAFS spectra (intensity versus wave vector k), it is seen that a peak occurs in the substitution spectrum (at about 4.5 Å$^{-1}$) that does not appear in the interstitial spectrum. Turning now to the Fourier transform of the spectra (intensity versus distance R), where peaks correspond to shells of neighboring atoms, the differences between the spectra are seen even more clearly. In the case of Ti-substitution, there are two peaks occurring at distances less than 3 Å (note that the peak positions do not correspond to actual bond lengths since phase corrections have not been made, however the number and relative spacing of the peaks is meaningful). The small-R peak is due to the nearest O atoms.

The Ce substitute has four oxygen neighbors at a distance 2.08 Å and two more at a distance 2.22 Å. These six O atoms all contribute to the first peak. The second peak is associated with the 8 nearest Ti atoms. There are four Ti atoms at a distance 3.16 Å, and four more at 3.78 Å, and all eight contribute to the second peak in the substitution spectra. Note that the two peaks are clearly resolved in the spectrum because of the significant difference between the Ce-O and Ce-Ti interatomic distances. The models of Ce substitution from simulation theory are shown in Figure 32.

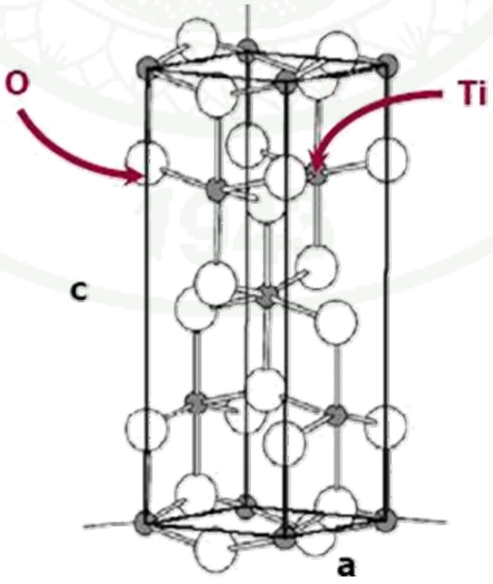

(a)

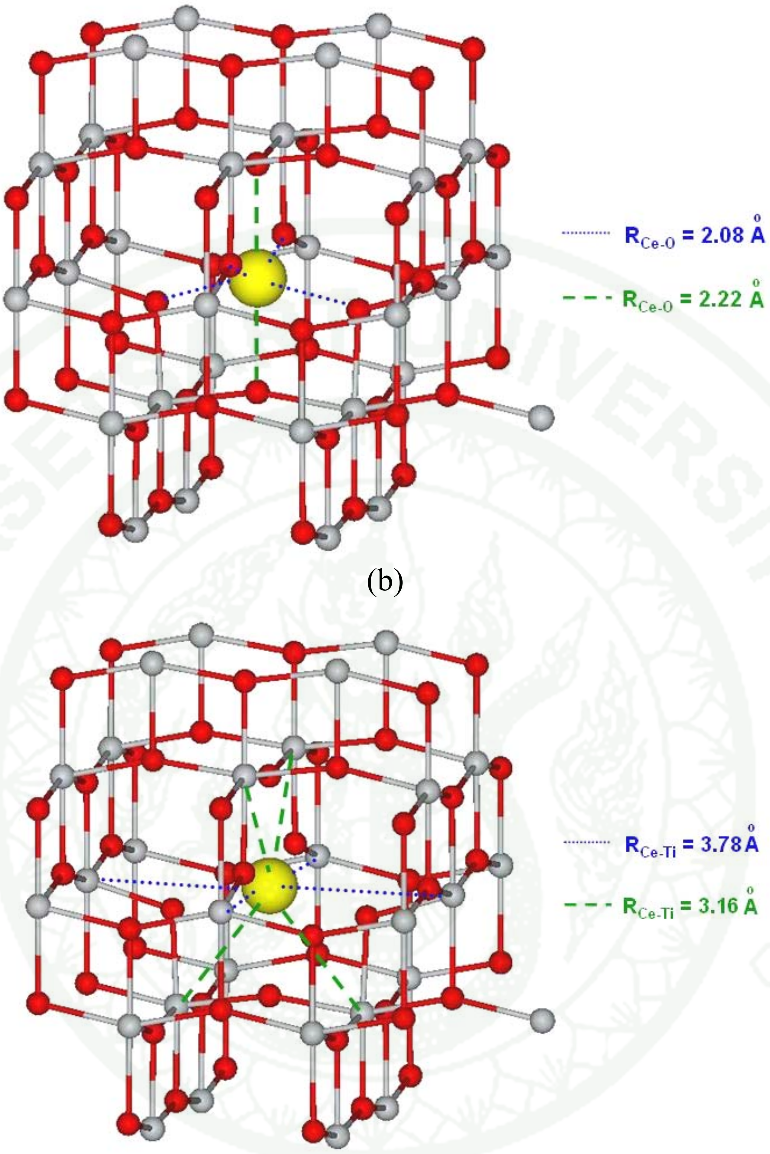

(b)

(c)

**Figure 32** (a) Perfect anatase $TiO_2$; Model of Ce *substitution* defects in anatase $TiO_2$ exhibit distance (R) of (b) absorbing Ce neighbor O atoms (red sphere) and (c) absorbing Ce - neighbor Ti atoms (grey sphere).

On the other hand, for the interstitial spectra, there is only one broad peak occurring below 3 Å. This single broad peak receives contributions both from neighboring O atoms and the nearest Ti atoms. The two peaks are not resolved because of the corresponding bond lengths are not sufficiently different. The interstitial Ce defect has four O neighbors at a distance 2.08 Å, two more at 2.67 Å, with four Ti neighbors 2.87 Å away and another four Ti atoms at a distance of 3.13 Å. The models of Ce interstitial defect from simulation theory are shown in Figure 33. The single peak results from additive contributions from all of these atoms, its position is determined by some weighted average of their bond lengths while its breadth is determined by the spread in the bond length of these atoms.

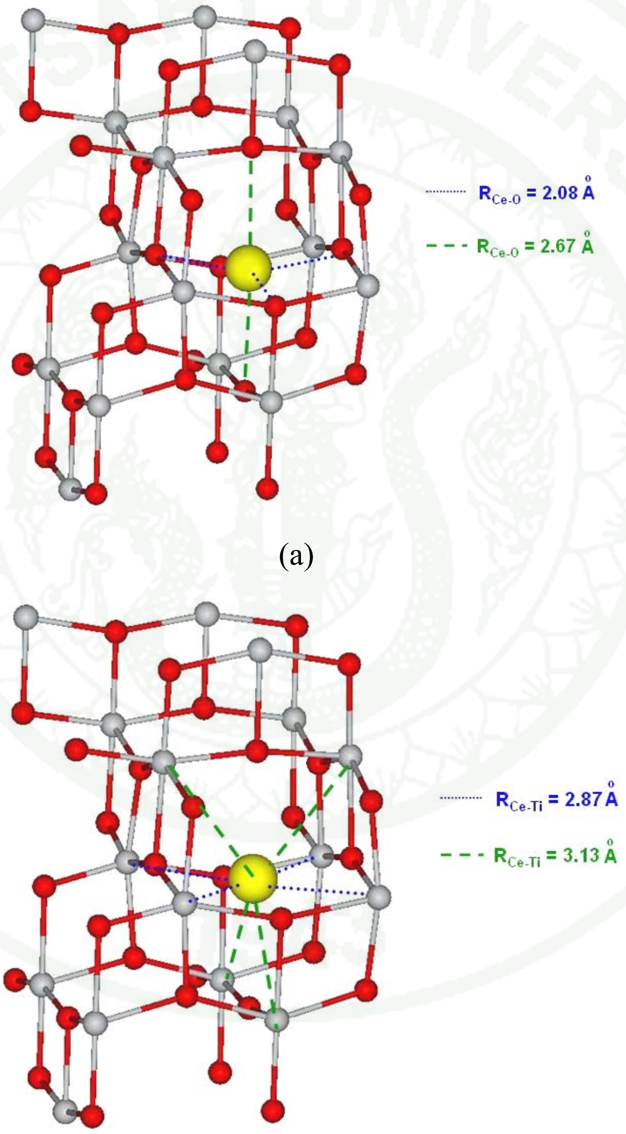

(b)

**Figure 33** Models of Ce *interstitial* defects in anatase $TiO_2$ exhibit distance (R) of (a) absorbing Ce – neighbor O atoms and (b) absorbing Ce - neighbor Ti atoms.

To summarize, the main qualitative differences between the Fourier transformed EXAFS data for the two candidate defect sites are: i) the first peak in the substitution spectrum occurs at a smaller distance (smaller by about 0.3 Å) than that of the interstitial spectrum ii) a second peak below 3 Å is resolved for the substitution spectrum but not the interstitial spectrum.

Note that the resolution in bond lengths is set by the width of the measured energy range. The noise in the high energy data forced to confine a rather narrow energy range above the absorption threshold, which resulted in relatively poor R-space resolution (Calculation of the theoretical spectra over this same energy range, thus giving the same resolution as expected in the experiment, for comparison). Nevertheless, the difference between the interstitial and substitution spectra is large enough to be distinguished, even given this limited resolution.

Comparison between theory and experiment are shown in Figure 34, the data of all 8%Ce/$TiO_2$ samples along with best fits obtained using the interstitial defect simulations. In these fits, the free parameters were: 1) the (first) edge energy $E_0$ , 2) a single Debye-Waller factor (for one of the nearest neighbor O atoms). A second edge was included at energy higher than the first by 8 eV, as discussed above. The Debye Waller factors for all other paths were fixed to a given ratio with the first path according to the correlated Debye model (with T=300 K and $T_{Debye}$=560 K).

For Ce atom as interstitial defect :

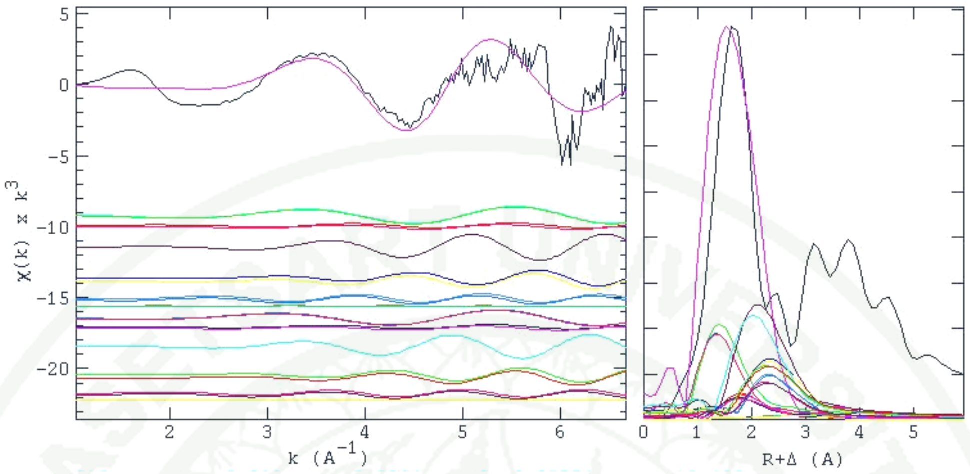

(a) CATi08-LW

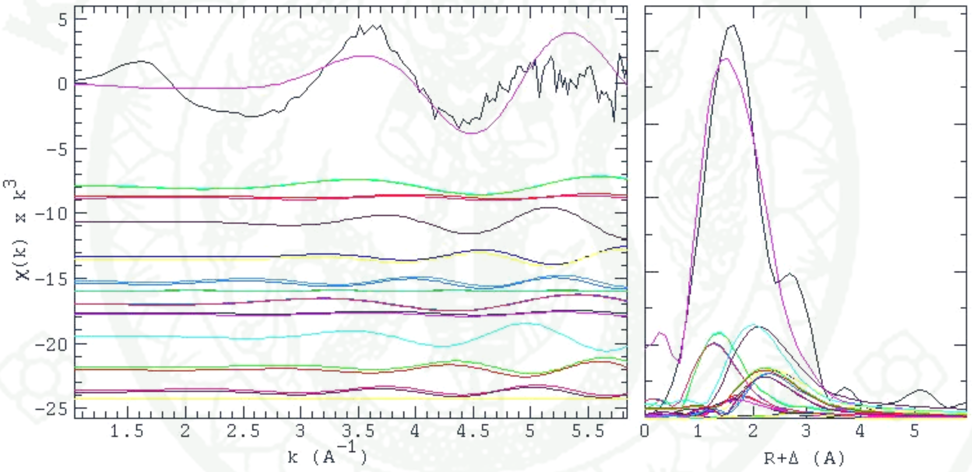

(b) CNTi08-LW

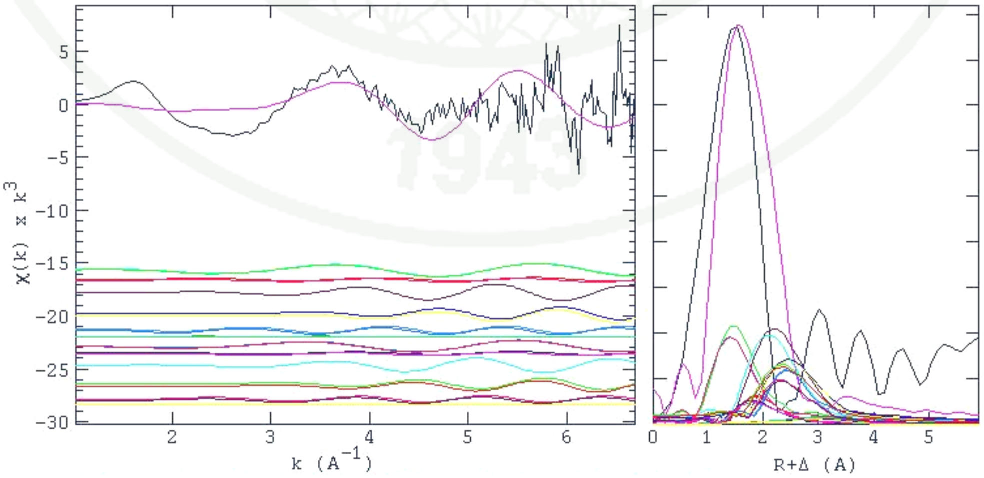

(c ) CNTi08-HW

**Figure 34** Fitted EXAFS (right) and FT of spectra (left) of 8%Ce/$TiO_2$ with Ce atom as interstitial defect; black line: experiment, pink line: theory.

For Ce atom as substitution defect :

The corresponding fits using simulations for the substitution defect of all 8%Ce/$TiO_2$ samples are shown in Figure 35.

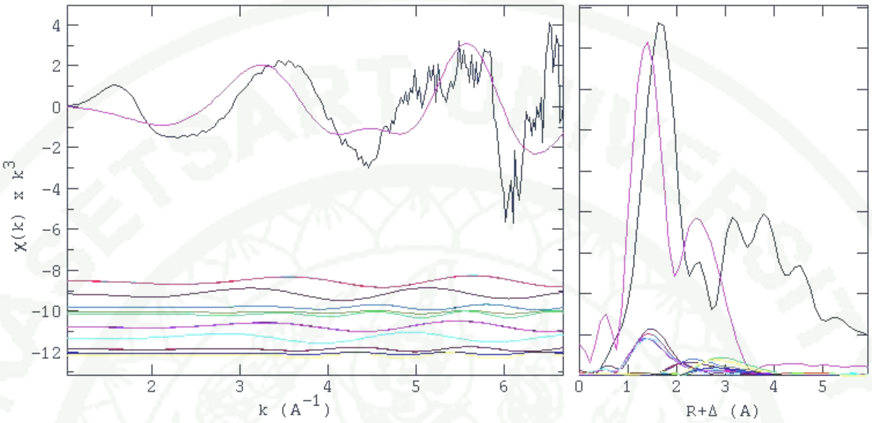

(a) CATi08-LW

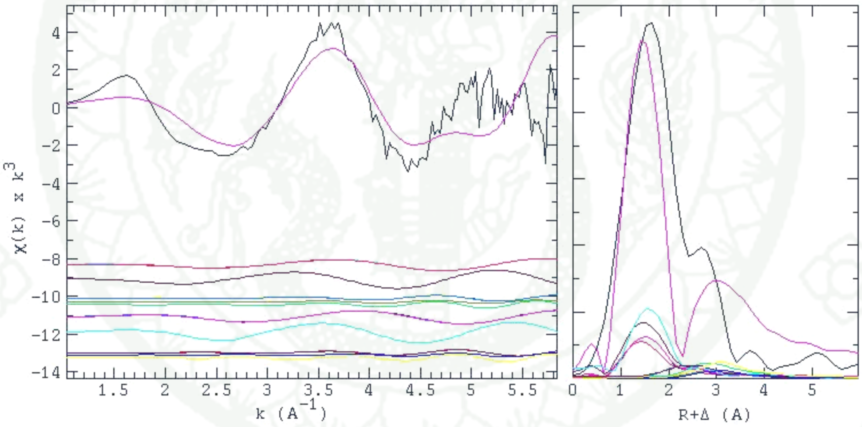

(b) CNTi08-LW

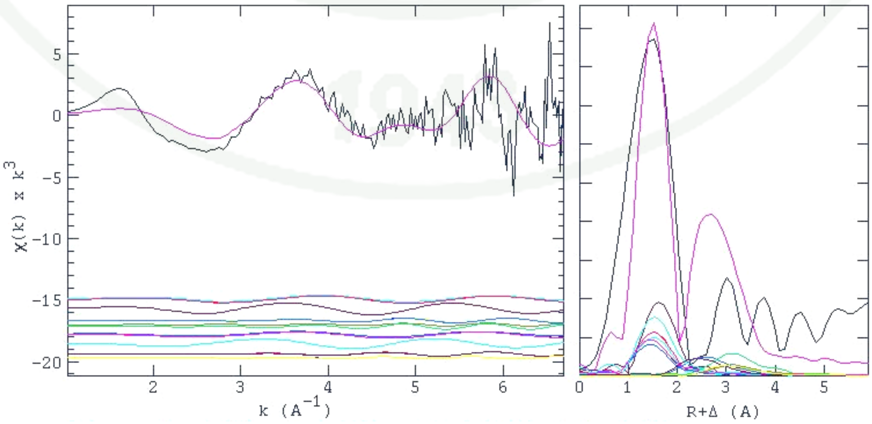

(c ) CNTi08-HW

**Figure 35** Fitted EXAFS (right) and FT of spectra (left) of 8%Ce/$TiO_2$ with Ce atom as substitution defect; black line: experiment, pink line: theory.

Although the quantitative agreement between theory and experiment is not especially good, it is evident from Figure 34 and 35 that the interstitial simulation is in better agreement with the measured spectra than the substitution simulation. At a qualitative level, the small peak in the EXAFS spectrum k~4.5 $Å^{-1}$, which is seen in the substitution simulation but not the interstitial simulation, is not present in the data. The Fourier transform of the spectra show that the interstitial simulation correctly accounts for the position of the primary peak in the data, whereas the substitution simulation can not.

The analysis was done using two sets for Ce in $TiO_2$: an interstitial site and the Ti -substitution site simulations. All 8%Ce/$TiO_2$ samples showed that the Ce atoms in $TiO_2$ obtained the best fits using the interstitial defect simulations with distance Ce-O as 2.09 and 2.64 Å and Ce-Ti as 2.87 and 3.13 Å.

*- High cerium content: 30%Ce/$TiO_{2(SG)}$*

Data were considered in an energy interval 5625-6000 eV for $L_3$-edge analysis (the spectrum at higher energies became too noisy to analyze). The $L_3$-edge spectra of 30%Ce/$TiO_2$ samples show a double-peak shape (like 8%Ce/$TiO_2$ samples) as shown in Table 15 and Figure 36.

**Table 15** The energy peaks of 30%Ce/$TiO_{2(SG)}$ samples for Ce $L_3$ edge.

| Sample code | Lower energy peak (eV) | Higher energy peak (eV) |
|---|---|---|
| CATi30-LW | 5730.70 | 5739.10 |
| CNTi30-LW | 5730.70 | 5739.10 |

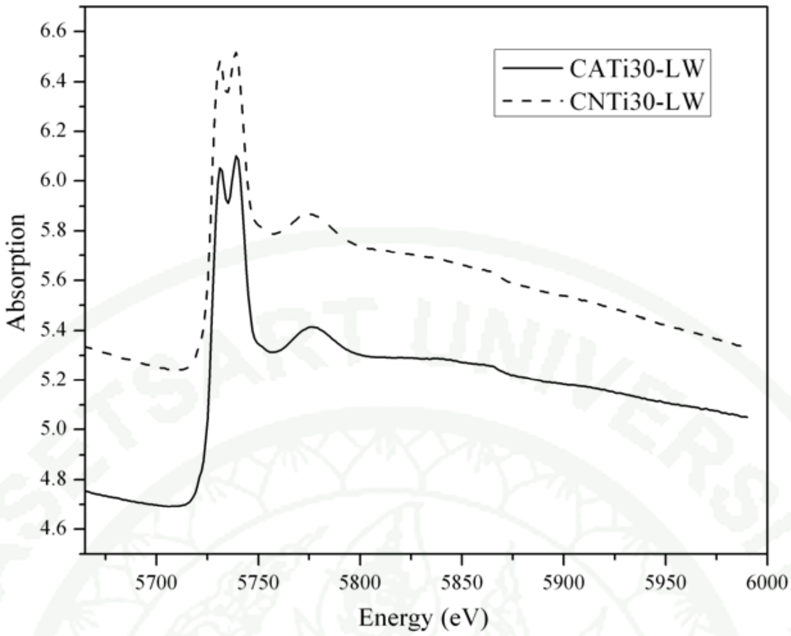

**Figure 36** Absorption spectra of $L_3$-edge of Ce in 30%Ce/$TiO_2$.

This double –peak shape is due to the mixed-valence behavior of Ce in its final state and the interaction between 4f orbitals of the metal and 2p orbitals of the ligands in its initial state (see, for e.g., Fonda 1999). A second edge includes the higher energy than the first by 9 eV. The absorption data of 30%Ce/$TiO_2$ were subtracted background as show in Figure 36. The background subtraction method can do in many ways and each way, it can change some things which differ from original data —such as the position and height of the spectra. This subtraction method can remain the position and height of the main peak occurring roughly 1.6 Å and 2.9 Å. (as show in figure 37b), so it is assumed this subtraction method is the right way.

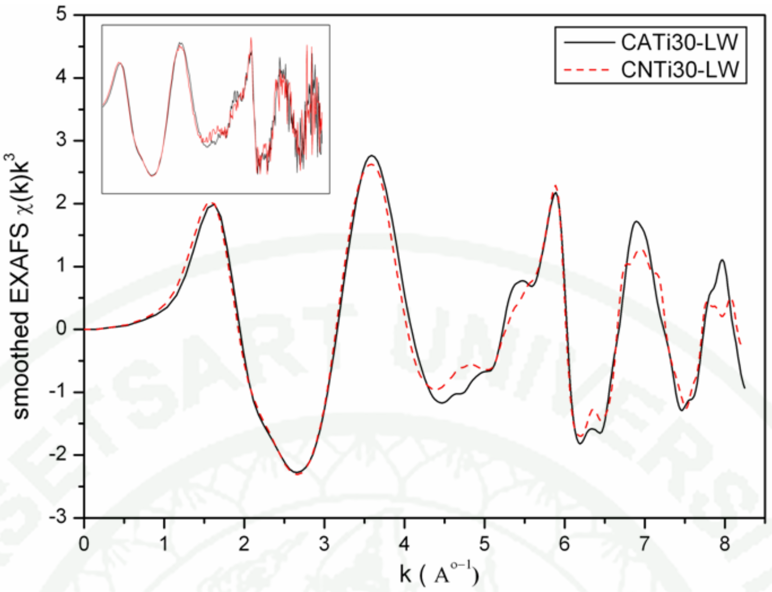

(a) measured EXAFS spectra

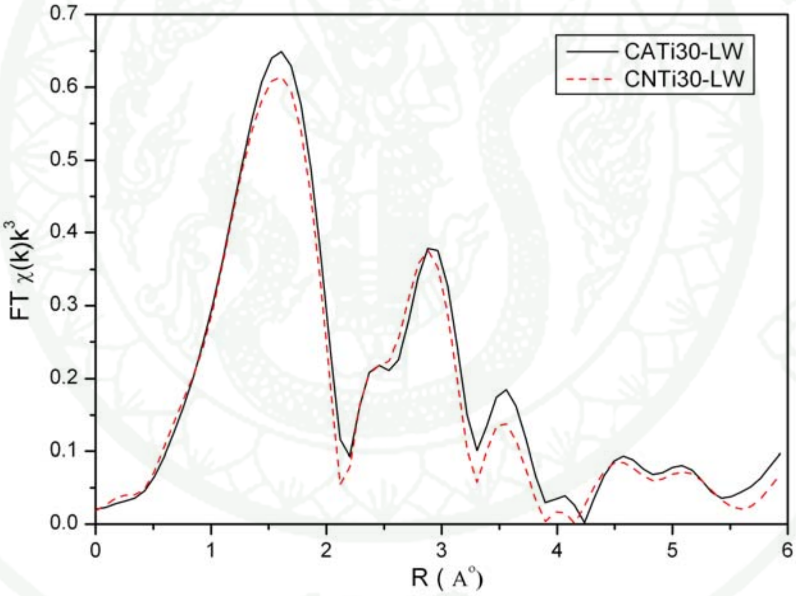

(b) Fourier transforms (FT)

**Figure 37** Ce $L_3$-edge spectra of 30%Ce/$TiO_2$.

Figure 37a shows smoothed EXAFS spectra of CATi30-LW and CNTi03-LW and original data (small panel) which are very similar especially k ranges to 4 Å$^{-1}$. However, the CNTi30-LW spectrum appears a small hump at k~4.5 Å$^{-1}$ that is more prominent than in the CATi30-LW spectrum. In Figure 37b, the magnitudes of the Fourier transforms (FT) of the spectra are shown. The FT spectra of two samples have a main peak occurring 1.62 Å, and a second peak is about 2.9 Å. There is also seen the slightly differences at distance 2.42 Å and the peak heights roughly 5%.

The analysis was done using two sets for Ce in $TiO_2$: an interstitial site and the Ti -substitution site with differencing in edge position by 9 eV. For each Ce defect site, the local structure was determined and the EXAFS spectra simulated so that, upon comparing the results with the measured spectra, the most likely site for Ce occupation in each sample could be determined. The theoretical plots of interstitial and substitution simulation show as see below figure. The FT spectra of 30%Ce/$TiO_2$ (Figure 36) are noticed that the two main peaks occur at 1.62 Å, and 2.9 Å, which are similar to the substitution theory graph more than interstitial theory.

Thus, the measured EXAFS were fitted with substitution theory spectra of CNTi30-LW as Figure 38. Notice, in FT fitting (the right panel), the measured (black line) and theory spectrum (pink line) are agreement. Contrary, in EXAFS fitting (the left panel) the theory spectrum has a hump peak (k ~4.5 $Å^{-1}$) that is not agreement in k space amplitude with measured EXAFS data (crude line), so it is assumed that the CNTi30-LW spectra can not obtain the best fits using the substitution simulation.

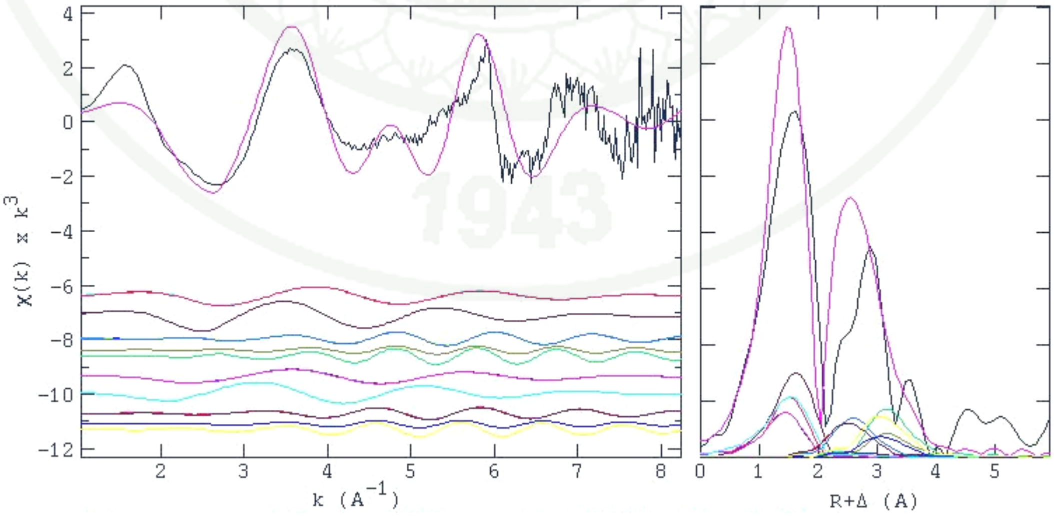

**Figure 38** Fitted EXAFS (right) and FT of spectra (left) of CNTi30-LW with Ce atom as substitution defect; black line: experiment, pink line: theory.

In this case, an interstitial mixed substitution simulation was used to resolve the amplitude fitting of k~4.5 Å$^{-1}$. Figure 39 shows the comparison between the interstitial mixed substitution and substitution simulation. Figure 39b shows that they have very similar Fourier transforms spectra, with two main peaks occur at R 1.5 Å, and 2.5 Å. The difference between them only shows up in the k-space spectrum in Figure 39a. From Figure 39(a), we can see two simulations of the k-space spectrum are the same features, except the mixed simulation (dash line) has the lower position, especially the lower amplitude at k~4.5 Å$^{-1}$. The feature is closer to our measured data than substitution simulation, so we concentrate on the interstitial mixed substitution simulation.

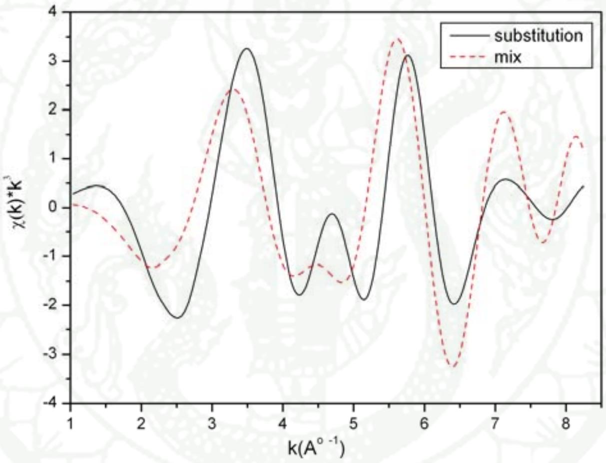

(a) simulated EXAFS spectra

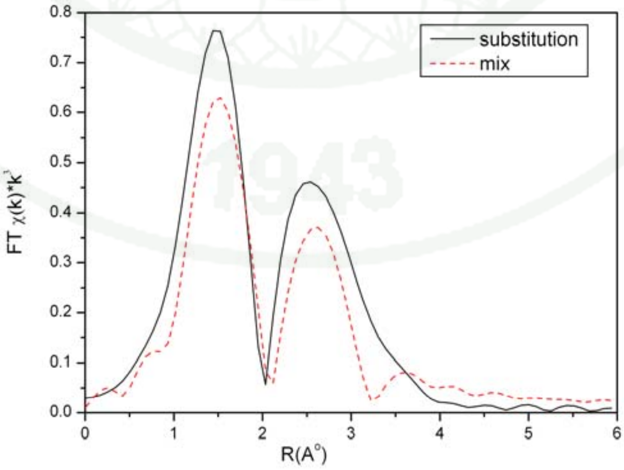

(b) Fourier transforms (FT)

**Figure 39** Comparison between the substitution (solid line) and interstitial mixed substitution simulation (dash line); (a) EXAFS, (b) FT spectra.

In addition, we consider interstitial mixed substitution simulation with different interstitial: substitution ratio to get the appropriate ratio with the fit amplitude at k~4.5 Å$^{-1}$. Figure 40 shows the k-space spectrum simulations with varying the interstitial: substitution ratio; 0.5:0.5, 0.3:0.7, 0.1: 0.9, 0.05: 0.95 and 0.01: 0.99, we can see that the simulations initially appear the hump peak (k~4.5 Å$^{-1}$) with interstitial: substitution ratio as 0.1:0.9.

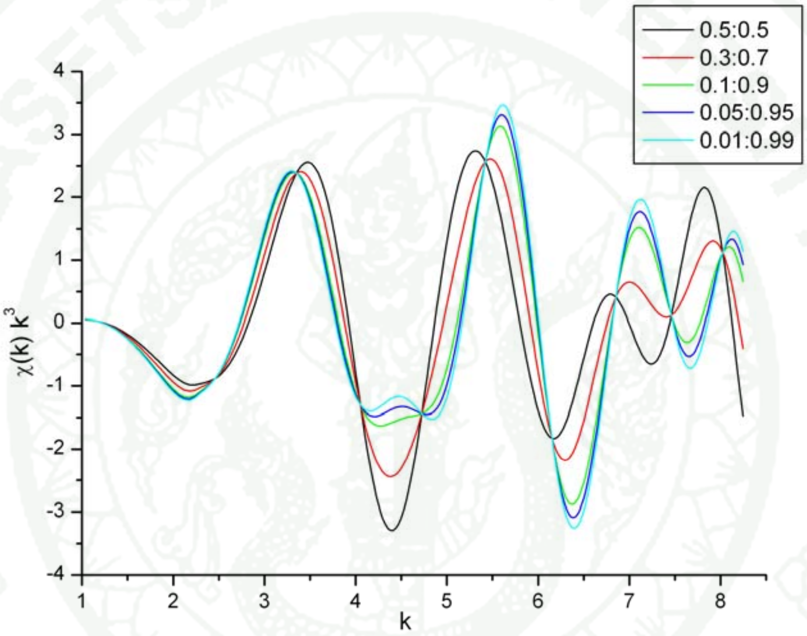

**Figure 40** Comparison of varied interstitial: substitution ratio for interstitial mixed substitution simulation.

From the above data, the measured data were fitted with the interstitial mixed substitution simulations. In Figure 40 show the data of all 30%Ce/$TiO_2$ samples along with best fits obtained using the interstitial mixed substitution defect simulations. In these fits, the free parameters were: (1) the (first) edge energy $E_0$, (2) coordination number of interstitial and substitution paths (interstitial: substitution ratio), (3) a single Debye-Waller factor (for one of the nearest neighbor O atoms). A second edge was included at energy higher than the first by 9 eV, as discussed previously.

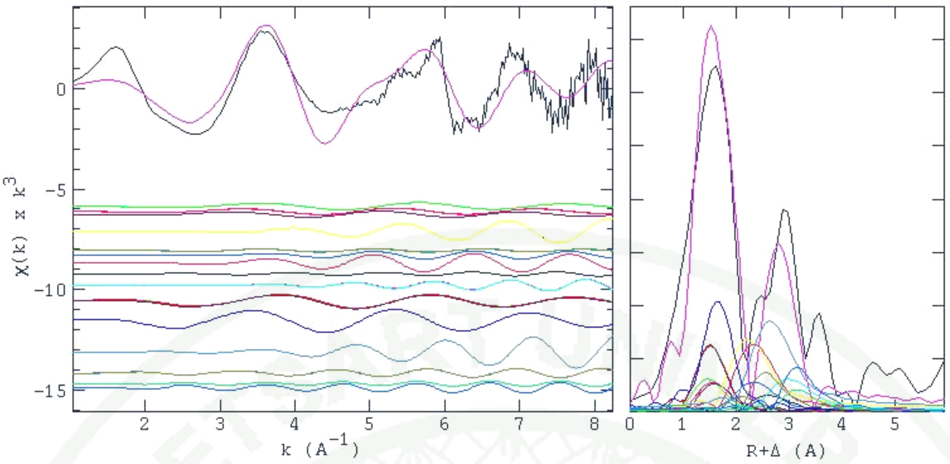

(a) CATi30-LW

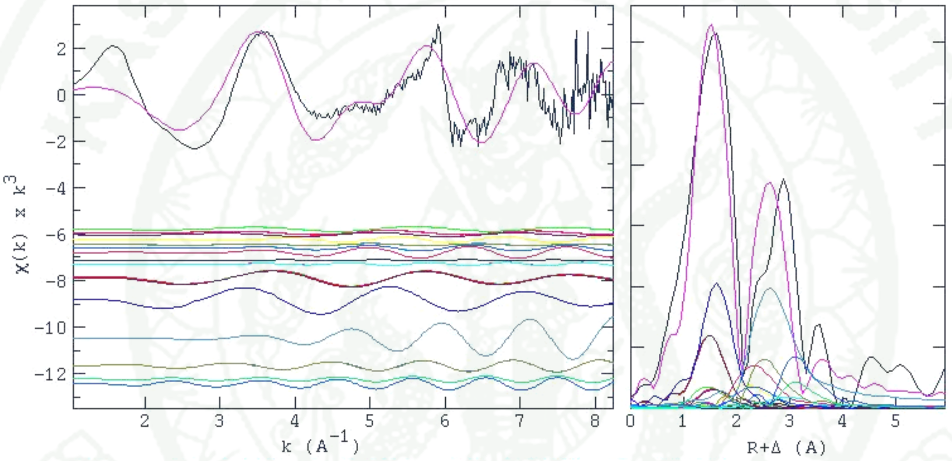

(b) CNTi30-LW

**Figure 41** Fitted EXAFS (right) and FT of spectra (left) of 30%Ce/$TiO_2$ with Ce atom as interstitial mixed substitution condition; black line: experiment, pink line: theory.

Figure 41a shows CATi30-LW spectrum fit in the interstitial mixed substitution simulation with 0.35 interstitial: 0.65 substitution ratio and CNTi30-LW (Figure 40b) fit with 0.22 interstitial: 0.78 substitution ratio. The ratios are similarly with the larger substitution ratio. However, it is noticed that the CNTi30-LW is the better fitting. It has been assumed that cerium ion resides in an anatase background, due to XRD and Raman spectra showed mainly anatase structure of CNTi30-LW with little variation whereas CATi30-LW was not clear about their structure. Addition, Raman result prominently exhibited the new compound peaks of CATi30-LW

(Reddy, 2003), which may affect to CATi30-LW spectra, not simple to fit. Therefore, CNTi30-LW fitting is better than another.

From the fitted data in Figure 41, there are two peaks occurring at distances less than 3 Å (note that the peak positions do not correspond to actual bond lengths since phase corrections have not been made, however the number and relative spacing of the peaks is meaningful. The first R peak is due to the nearest O atoms. The Ce has four oxygen neighbors at distance 2.08, 2.17 Å and two more at a distance 2.22, 3.31 Å. These six O atoms all contribute to the first peak. The second peak is associated with the 8 nearest Ti atoms. There are four Ti atoms at a distance 2.93 Å, and four more at 2.78, 3.64 Å, and all eight contribute to the second peak in the spectra. Note that the two peaks are clearly resolved in the spectrum because of the significant difference between the Ce-O and Ce-Ti interatomic distances. Noticed, the distances of Ce-O and Ce-Ti bonds are the average distances of interstitial and substitution simulations.

From the fitted results of 30%Ce/$TiO_2$ spectra, it can be assumed that Ce atoms of the samples reside as both an interstitial and substitution defect sites in $TiO_2$ anatase with different ratios; CATi30-LW and CNTi30-LW spectra fitted with interstitial: substitution ratios as 0.35: 0.65 and 0.22: 0.78, respectively.

For the high cerium precursor concentrations for both [$Ce(acac)_3$ and $Ce(NO_3)_3$] under low water hydrolyses [(30%Ce = 0.0015 mol) and Ti-alkoxide precursor (0.01 mol) in low water hydrolysis ($H_2O$ = 0.04 mol)], Ce-precursors would be hydrolyzed completely in the same way as the low cerium precursor concentrations. The mechanisms should be proposed in the same ways as shown in Scheme 15 for the low water hydrolysis and in Scheme 16 for the high water hydrolysis. The high concentration of Ce ions between Ti-O-Ti linkages make it possible for the Ce ions to substitute in the Ti ions positions in $TiO_2$ structure after calcination. However, the size of Ce ion (90 pm) which is bigger than Ti ion (60 pm) hinders the Ti-substitution. Therefore, the EXAFS simulations of both substitution and interstitial approaches fit well with the experimental results.

From EXAFS results, it can be concluded that the different localize of Ce atom in $TiO_2$ with different Ce percentage, following: the lower percentage resides as an interstitial site whereas the higher resides both an interstitial site and the Ti-substitution site in $TiO_2$, respectively.

### 1.2 Characterizations of the catalysts:
### $Co_{CP}$-$Ce_{CP}/TiO_2$ (anatase), $Co_{CP}/Ce$-$TiO_{2(SG)}$

*XRD results*

XRD patterns of the calcined Ce promoted catalysts compared with the unpromoted $Co_{CP}/TiO_2$ (anatase) and $TiO_2$ (anatase) are shown in Figure 42. The catalysts show peaks at $2\theta = 25.33$, 48.10 and 55.14° correspond to anatase structure of $TiO_2$ support. For Co deposited on Ce promoted $TiO_2$ [10%$Co_{CP}$/1%Ce-$TiO_{2(SG)}$] show very small peak of $Co_3O_4$ at $2\theta = 32.00$° (Batista *et al.*, 2003).

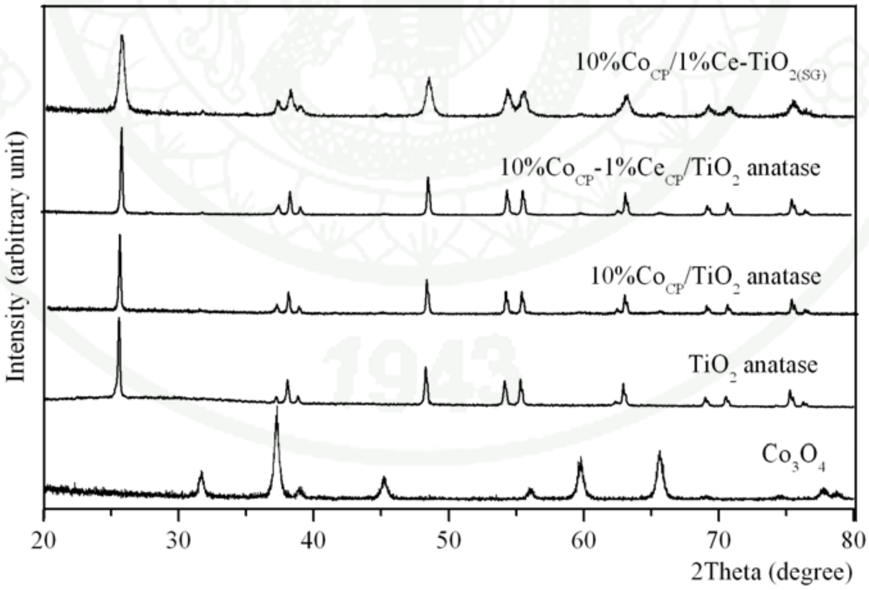

**Figure 42** XRD patterns of 10%$Co_{CP}$/1%Ce-$TiO_{2(SG)}$, 10%$Co_{CP}$-1%$Ce_{CP}/TiO_2$ anatase and 10%$Co_{CP}/TiO_2$ anatase catalysts, compared with $TiO_2$ anatase.

*Temperature Programmed Reduction (TPR) results*

TPR of the unpromoted $Co_{CP}/TiO_2$ (anatase), $Co_{CP}$-$Ce_{CP}/TiO_2$ (anatase) and $Co_{CP}/Ce$-$TiO_{2(SG)}$ are shown in Table 16. The low temperature peak (1st peak) is typically assigned to reduction of $Co_3O_4$ to CoO. The high temperature peak (2nd peak) is assigned to reduction of CoO species to $Co^0$ as shown in Table 16.

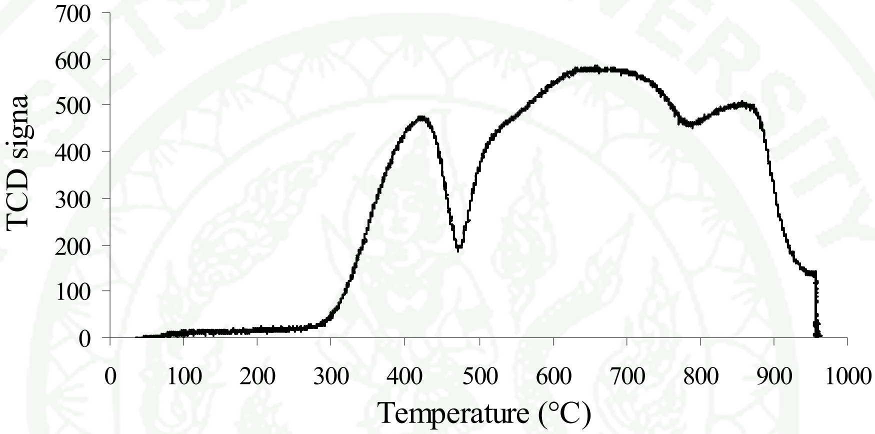

(a) $10\%Co_{CP}/TiO_2$ (anatase)

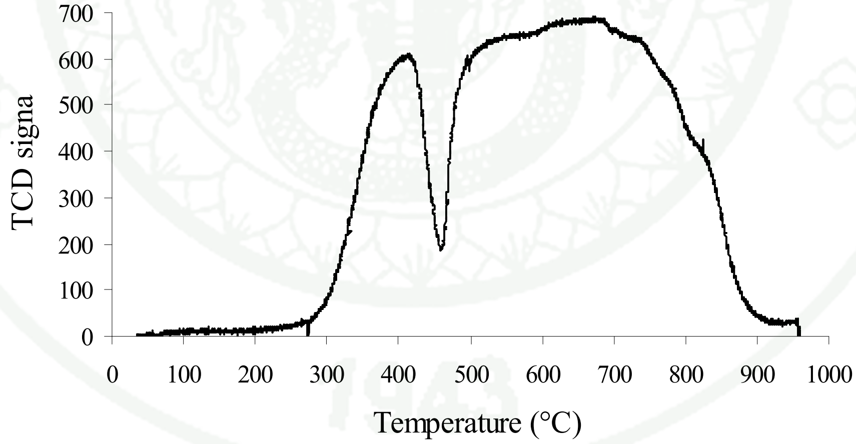

(b) $10\%Co_{CP}$-$1\%Ce_{CP}/TiO_2$ (anatase)

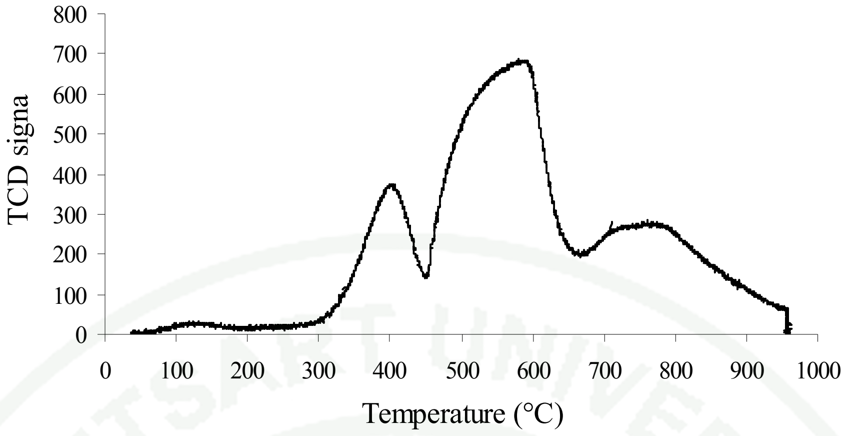

(c) $10\%Co_{CP}/1\%Ce\text{-}TiO_{2(SG)}$

**Figure 43** TPR profiles of (a) $10\%Co_{CP}/TiO_2$ (anatase), (b) $10\%Co_{CP}\text{-}1\%Ce_{CP}/TiO_2$(anatase) and (c) $10\%Co_{CP}/1\%Ce\text{-}TiO_{2(SG)}$.

**Table 16** TPR results of supported Cobalt FT catalysts.

| Catalysts | T (°C) of reduction | |
|---|---|---|
| | 1st | 2nd |
| $10\%Co_{CP}/TiO_2$ (anatase) | 421 | 480-900 |
| $10\%Co_{CP}\text{-}1\%Ce_{CP}/TiO_2$ (anatase) | 413 | 450-900 |
| $10\%Co_{CP}/1\%Ce\text{-}TiO_{2(SG)}$ | 400 | 579 |

Compared the cobalt reduction performances of the cobalt precipitated on the cerium promoted $TiO_2$ ($10\%Co_{CP}/1\%Ce\text{-}TiO_{2(SG)}$) to the cerium promoted cobalt on $TiO_2$ (10%Co-1%Ce/$TiO_2$-anatase) and the unpromoted cobalt on $TiO_2$ (10%Co on $TiO_2$-anatase), it showed that the cobalt precipitated on the cerium promoted $TiO_2$ ($10\%Co_{CP}/1\%Ce\text{-}TiO_{2(SG)}$) has been reduced to completion at lower temperature (around 579 °C) with narrow temperature range.

It can be explained that the chemical bond of Co-O-Ce made $CoO_x$ difficult to be reduced (Liu *et al*., 2007), therefore the cerium promoted cobalt on $TiO_2$ (10%Co-1%Ce/$TiO_2$-anatase) was slowly reduced with the wide temperature range (from 450-900 °C). The strong Co–$TiO_2$ also made the reduction of active Co much difficult

(480-800 $^{o}$C) for the reference (10%Co on $TiO_2$-anatase). The result of cerium promoted $TiO_2$ (10%$Co_{CP}$/1%Ce-$TiO_{2(SG)}$) confirmed the assumption that Ce promoted $TiO_2$ reduces the interaction of Co-O-Ce and Ce as a promoter with Ce ions interstitial species in $TiO_2$ eases the $CoO_x$ reduction to $Co^0$.

For the FT synthesis. the reduction temperature of the catalysts were operated at 550 $^{o}$C 7 h for 10%$Co_{CP}$-1%$Ce_{CP}$/$TiO_2$ (anatase) to obtain Co metal active spicies for the FT synthesis.

## 2. Fischer-Tropsch Experimental

### 2.1 Fischer-Tropsch product analysis:

Testing of instantaneous products analysis using model product substances

The model substances were collected in ampoules according to the Method 2.1 and analyzed with the existing ITSS set up I together with the following GC conditions.

*GC set up I condition I :*

| | |
|---|---|
| Column oven | 30 °C hold 5 min – 225 °C (rate 3 °C/min) hold 10 min |
| Stationary phase | CP-SilicaPLOT (bonded silica porous layer on the inner wall, 30m x 0.53 mm x 6.00 µm) |

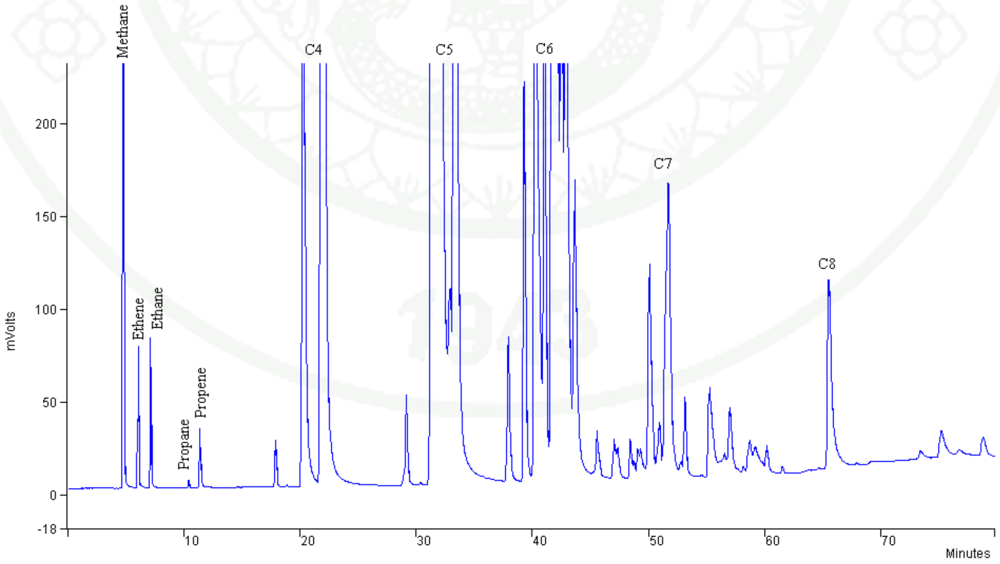

(a) gasoline vapor

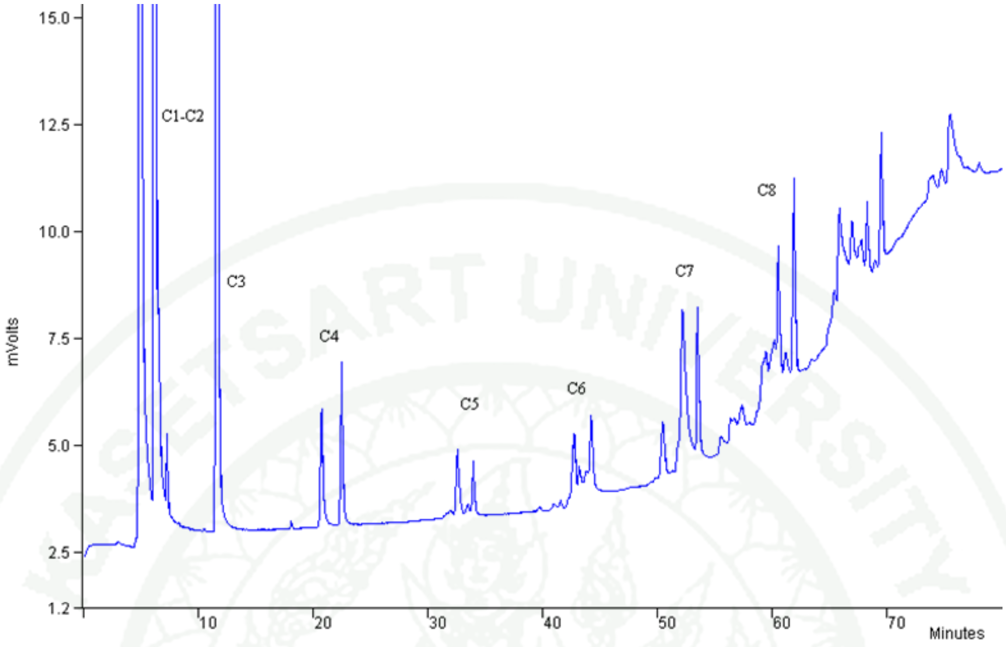

(b) diesel vapor

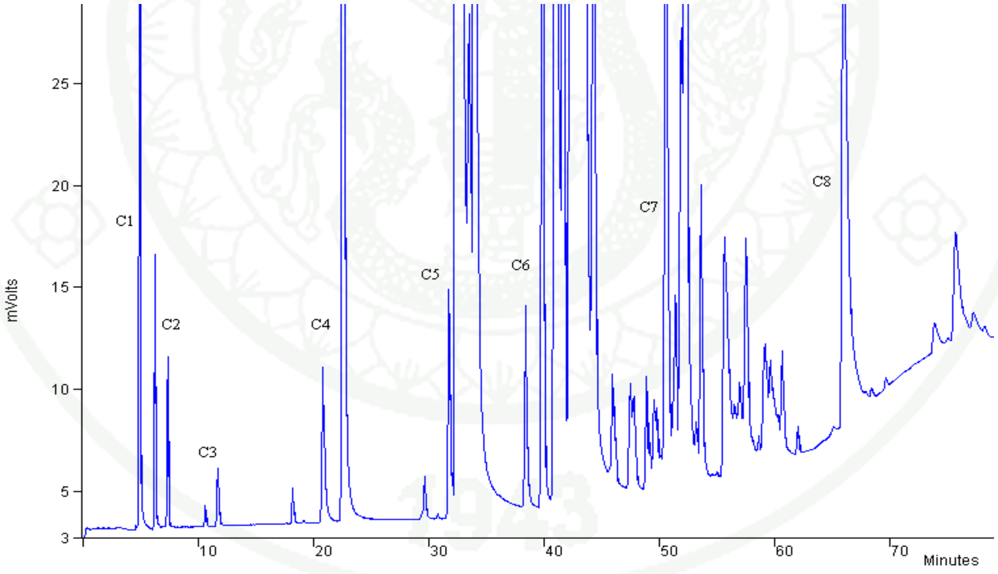

(c) gasoline mixed diesel

**Figure 44** Chromatograms of (a) gasoline vapor (b) diesel vapor (c) gasoline mixed diesel. All samples mixed with $N_2$ and natural gas in ampoules. The starting temperature program is 30 $^{o}$C.

Figure 44 shows chromatograms of model substance vapors: (a) gasoline vapor (b) diesel vapor (c) gasoline mixed diesel vapors in ampoules. The sample gases and vapors were stored in ampoules with the ampoule sampler and analyzed the sample components in the ampoules using the ampoule breaker connected to a GC with SilicaPLOT (GC set up I). In chromatogram (a) the gasoline was separated into methane, ethene, ethane, propene, propane, $C_4$, $C_5$, $C_6$, $C_7$, and $C_8$ hydrocarbon. In chromatogram (b), it shows that the diesel components are separated well up to $C_7$ hydrocarbon, the higher components show broad peak without separation. The chromatogram (c) is the mixture of (a) and (b) which is not separated well from $C_{5+}$.

To compare the column efficiency, the ampoules of gasoline vapor analyzed using GC with different columns; SilicaPLOT (GC set up I, condition II) and DB-1 (GC set up II, condition I) are presented in Figure 44a and b, respectively. The analysis methods using are as follows:

*GC set up I condition II :*

Column oven -80 $^{o}$C hold 3.5 min
rate 15 $^{o}$C/min; -35 $^{o}$C hold 3.5 min
rate 10 $^{o}$C/min; -5 $^{o}$C hold 2.0 min
rate 2 $^{o}$C/min; 25 $^{o}$C
rate 2 $^{o}$C/min; 225 $^{o}$C hold 10 min
Columns :
Stationary phases CP-SilicaPLOT (bonded silica porous layer)

*GC set up II condition I :*

Column oven -60 $^{o}$C hold 3.5 min
rate 15 $^{o}$C/min; -35 $^{o}$C hold 3.5 min
rate 10 $^{o}$C/min; -5 $^{o}$C hold 2.0 min
rate 2 $^{o}$C/min; 25 $^{o}$C

rate 2 $^{o}$C/min; 225 $^{o}$C hold 10 min

Columns :

Stationary phases DB-1 (polymethylsiloxane)

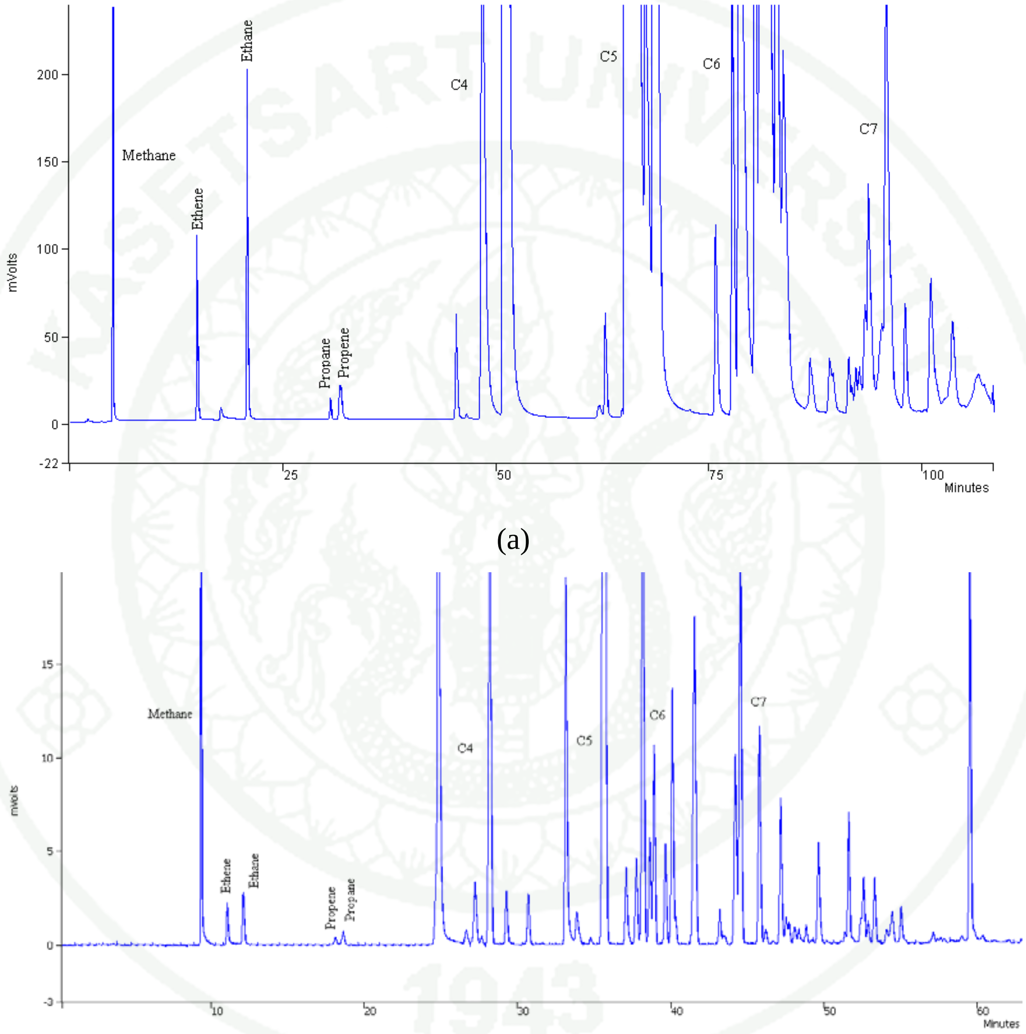

(a)

(b)

**Figure 45** Chromatograms of gasoline vapor mixed $N_2$ and $CH_4$ in ampoule. :(a) SilicaPLOT-analysis set up I and (b) DB-1-analysis set up II.

It can be seen that SilicaPLOT can separate the small molecules of hydrocarbon compounds ($C_1$-$C_4$) very well and is not suitable for the higher molecules such as $C_{5+}$. DB-1 is suitable for gasoline vapor from $C_1$ up to higher hydrocarbons.

The starting temperatures of the programs are also tested using GC set up I condition I and II and the chromatograms are shown in Figure 46(a) and (b).

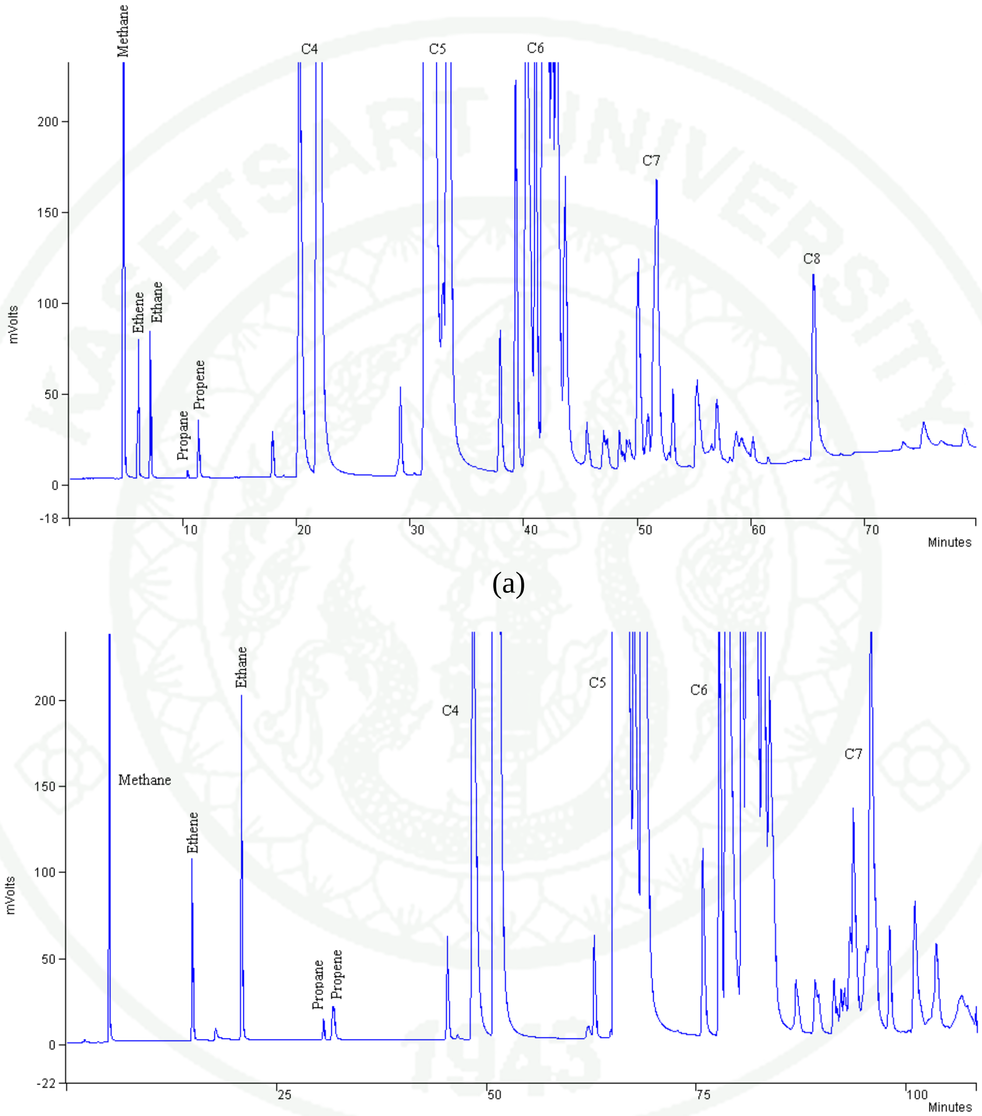

(a)

(b)

**Figure 46** Chromatograms of gasoline vapor mixed $N_2$ and $CH_4$ in ampoule. The starting temperature program is (a) 30 $^{o}$C and (b) -80 $^{o}$C.

The chromatograms of gasoline vapor mixed with $N_2$ and $CH_4$ starting at temperature (-80 $^{o}$C) show clear separation of hydrocarbons, especially $C_1$ – $C_4$ hydrocarbons.

### 2.2 Fischer-Tropsch synthesis

#### 2.2.1 Testing of experimental set up I

Cyclopropane (0.5% in $N_2$) was stored in the ampoules with the flowing rate 10.00 cm$^3$/min at 10 bar. The ampoules were analyzed using GC-FID with CP-SilicaPLOT (GC set up I condition I). The chromatograms of collected cyclopropane (CPr) are shown in Figure 47.

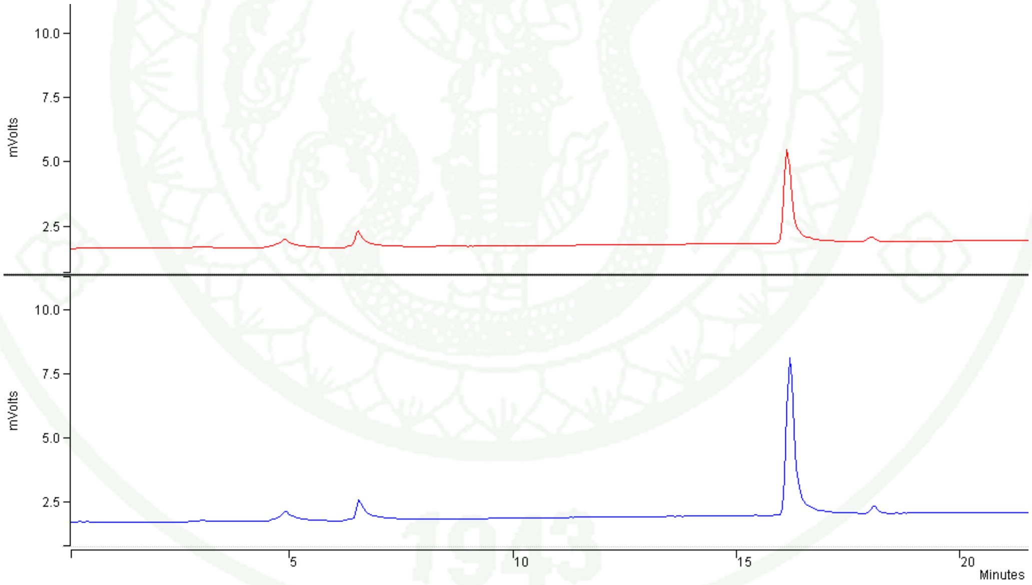

**Figure 47** Chromatograms of CPr ampoule; #2 (top) and #1 ampoule (bottom).

**Table 17** Summarize peak areas of CPr at 15.9 min. retention time.

| **No. of experiment** | **Peak area** |
|---|---|
| #1 | 87,055 |
| # 2 | 55,949 |
| # 3 | 112,512 |
| #4 | 77,703 |
| #5 | 73,286 |
| #6 | 129,375 |
| average | 98,219 |
| %rsd | 27.52 |

Background peaks (at 4.8 and 6.4 min) may be occurring from air or atmosphere or the leakage of breaker. It always appears in chromatograms and area decrease for the following analysis.

From the GC results, the peak areas of cyclopropane rather fluctuated. The reason may be the inconstant flowing of gas outlet after capillary in the FT line with the low flow rate of 9.00 $cm^3$/min. To solve this problem, the capillary chamber was removed from the set-up and re-arranged the experimental set-up as shown in Scheme 17.

### 2.2.2 Experimental set up II

Experimental set up II was developed to correct those problems of Experimental set up I such as the fluctuation of flow.

The fluctuation problem was solved by removing the capillary chamber from the set up I and the experimental set up I was remodeled to be a set up II as shown in Scheme 17.

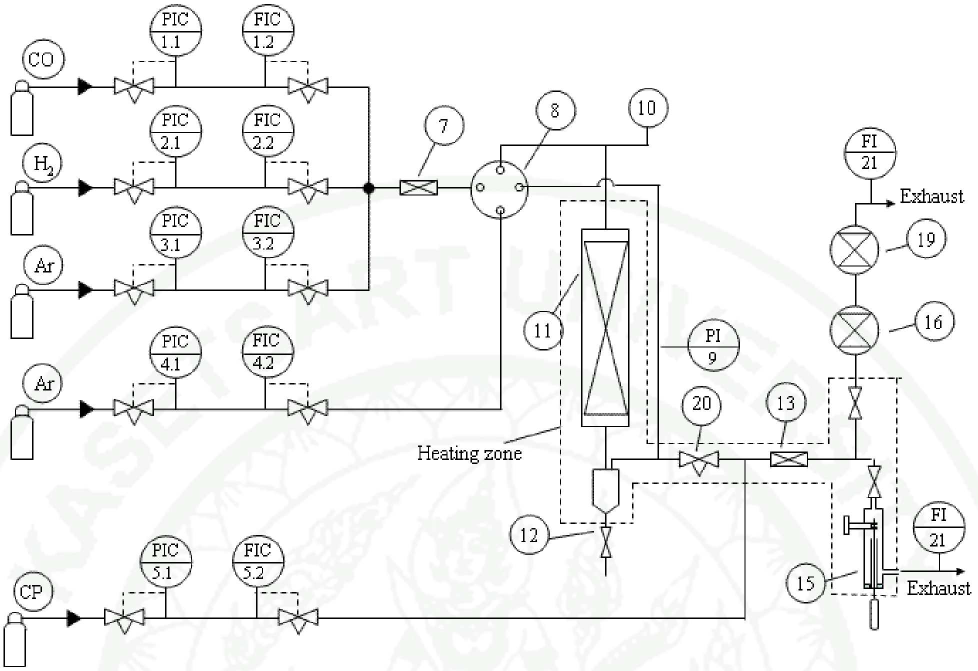

**Scheme 17** Fischer-Tropsch experimental set up II.

Moreover, number 20 in the set up I were replaced with a leak valve (Valve 20) in the set up II for controlling the pressure at 5 or 10 bar in the reaction line. Number 21 is the flow indicator at the end of line to indicate roughly the products gas flow.

To test the developed Fischer-Tropsch set up, the peak areas ratio of methane and the reference CPr were investigated by collecting the reference gas mixtures with the ampoule sampling unit in the reaction line.

*Testing of methane/cyclopropane ratio*

The ampoules of 0.5% CPr (in $N_2$) and $CH_4$ (purity 99.99%) mixture were collected with the instantaneous total stream sampling unit and analyzed using GC with FID and connected to DB-1 column (GC set up II condition I). Peak areas of the different $CH_4$/CPr ratios are compared in Figure 48.

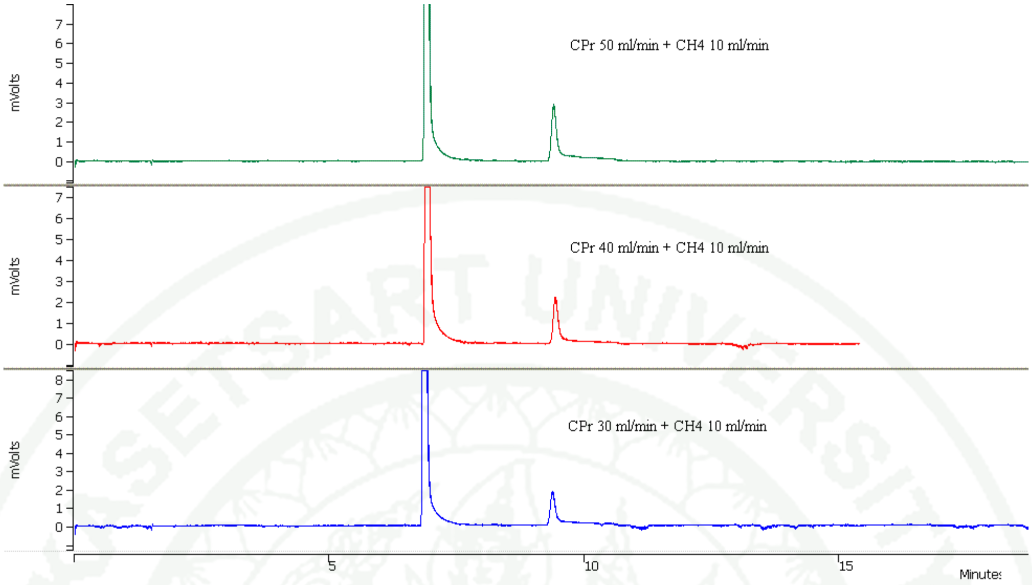

**Figure 48** The different of $CH_4$/CPr ratio in ampoules are analyzed using GC.

Retention time at 6.6 min and 9.1 min were assigned for $CH_4$ peak and CPr peak, respectively. Optimum condition is used for calibration curve of external standard as CPr 40.00 $cm^3$/min mixed with $CH_4$ (bypass) 10.00 $cm^3$/min at 1 bar, room temperature. Because of the CPr flowing was increased to 50.00 $cm^3$/min but the peak areas of $CH_4$/CPr slightly increased.

**Table 18** The results of peak area ratio of 0.5%CPr mixed with $CH_4$ in ampoules.

| No. | Area | | Area ratio of |
|---|---|---|---|
| | $CH_4$ | CPr | $CH_4$/CPr |
| #1 | 297,189 | 18,292 | 16.23 |
| #2 | 248,062 | 13,906 | 17.83 |
| #3 | 396,701 | 26,216 | 15.13 |
| #4 | 159,465 | 10,583 | 15.06 |
| #5 | 192,615 | 11,652 | 16.53 |
| #6 | 202,248 | 11,618 | 17.42 |
| #7 | 431,941 | 26,837 | 16.10 |

**Table 18** (Continued)

| No. | Area | | Area ratio of CH$_4$/CPr |
|---|---|---|---|
| | CH$_4$ | CPr | |
| #8 | 433,324 | 24,950 | 17.36 |
| #9 | 171,086 | 9,955 | 17.18 |
| #10 | 194,934 | 11,047 | 17.64 |
| | | average | 16.65 |
| | | %rsd | 6.03 |

*Calibration linear curve of cyclopropane*

The percentage of 0.5% cyclopropane (CPr) in N$_2$ as an external standard was varied using the mass flow controller and collected with the ITSS. The peak area of cycloprapane was analyzed using GC equipped with FID.

**Table 19** Percentage of cyclopropane of calibration curve.

| 0.5% CPr in N$_2$ (cm$^3$/min) | N$_2$ carrier gas (cm$^3$/min) | Total flow rate (cm$^3$/min) | %CPr |
|---|---|---|---|
| 3.00 | 47.00 | 50.00 | 0.03 |
| 3.00 | 27.00 | 30.00 | 0.05 |
| 5.00 | 20.00 | 25.00 | 0.10 |
| 10.00 | 15.00 | 25.00 | 0.20 |
| 20.00 | 20.00 | 40.00 | 0.25 |

Example

Calculation of %CPr

%CPr = (0.5/100 x flow of CPr) / total flow rate x 100

0.5% CPr flow rate = 3.00 $cm^3$/min

$N_2$ carrier gas flow rate = 27.00 $cm^3$/min

∴ %CPr = (0.5/100 x 3) / 30.00 x 100 = 0.05%

The calibration curve is plotted between the average of peak area and percentage of cyclopropane as shown in figure 49.

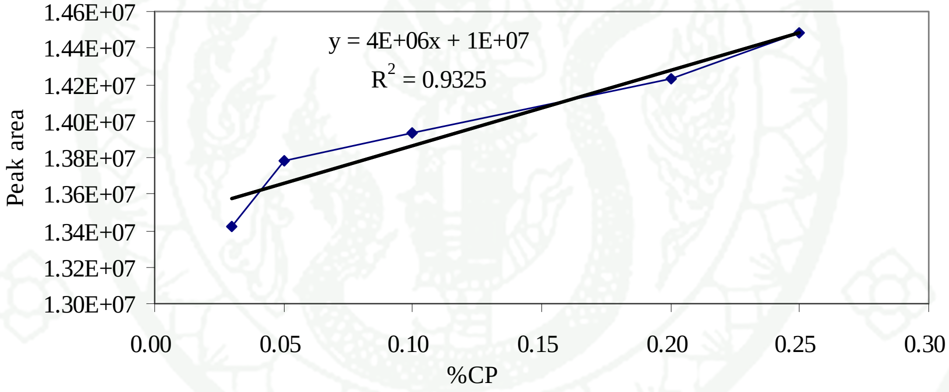

**Figure 49** Calibration linear curve of the CPr external standard.

*Reactor* :

In some cases, the quartz tube was found broken when opening the stainless steel reactor especially at the frit joint and the catalyst bed. Finally the reactor has been developed by changing the construction of the quartz and metal reactors.

*Stainless steel (SS) reactor*

For the SS-reactor, the bottom end has been changed concerning the possibility of the open-end for flowing through products, which has to be sealed by a holed septum (or a rubber sealing) and the metal shell as shown in Figure 50.

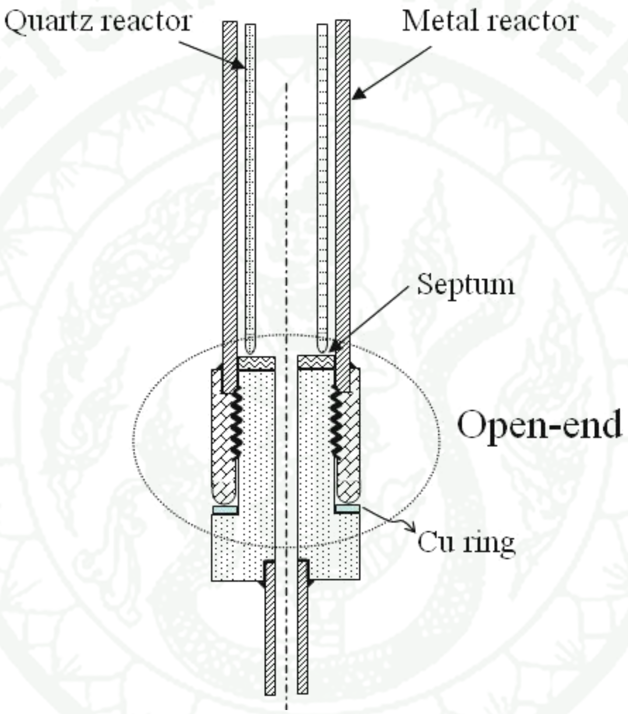

**Figure 50** Two parts of Open-end drawing of the stainless steel reactor.

*Quartz reactor*

For the quartz reactor, the quartz frit plate has been changed to a support to reduce the stress of the quartz. The new designed reactor is shown in Figure 51.

*Spring*

The pressure of the quartz tubing against the rubber sealing and the SS- spring on top should be aware. A longer spring with more compression length should be considered.

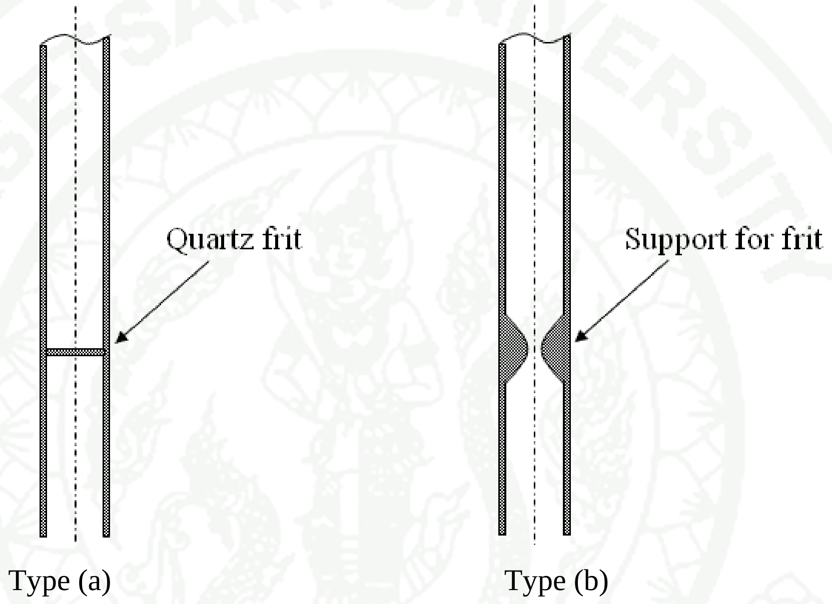

**Figure 51** Comparison the quartz frit joint and the support for frit of quartz tube: type (a) and type (b)

2.2.3 Fischer-Tropsch reaction

The developed FT set up (Set up II) was used for FT synthesis to investigate the activity of cobalt based catalysts.

**Table 20** Temperature, pressure and flow rate of gases for FT synthesis.

| Catalysts | T (°C) | P (bar) | Flow rate (cm$^3$/min) | | | $H_2$:CO | GHSV ($h^{-1}$) |
|---|---|---|---|---|---|---|---|
| | | | $H_2$ | CO | Ar* | | |
| 47%$Co_{SG}$ -7%$Ce_{SG}$/$SiO_2$ (aerosil) | 190 | 5 | 20.00 | 10.00 | 10.00 | 2:1 | 86 |
| 10%$Co_{CP}$-1%$Ce_{CP}$/$TiO_2$ (anatase) | 220 | 10 | 20.00 | 10.00 | 60.00 | 2:1 | 32 |

**Note** : Ar* as Ar (by pass)

FT synthesis has been tested on 47%Co-6%Ce/$SiO_{2(SG)}$ (aerosil) 1.5000 g (2.00 cm$^3$), 190 °C, 5.0 bar, $H_2$:CO = 2:1. The starting temperature of GC was 40 °C (Analysis with GC set up II condition III)

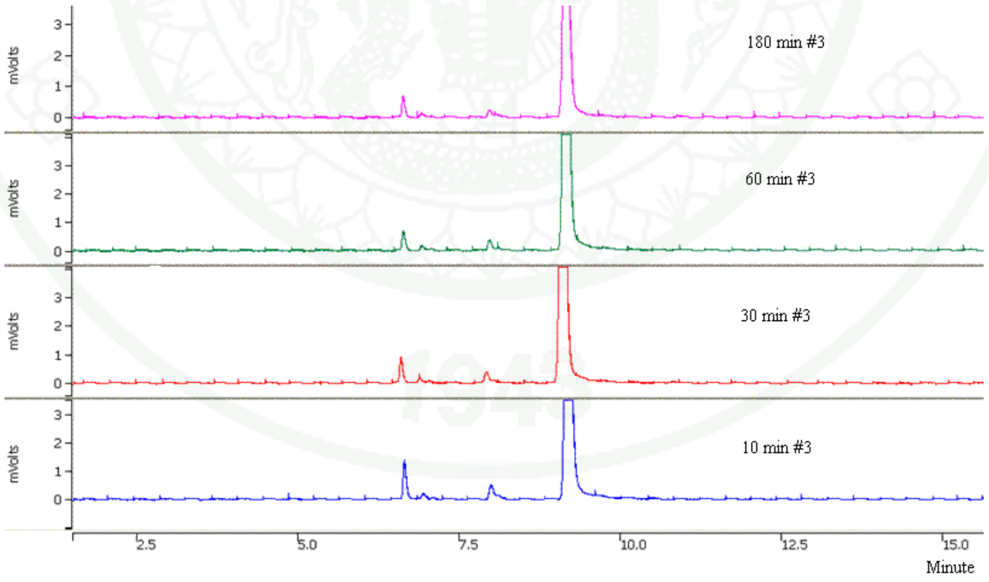

**Figure 52** Chromatograms of ampoule at reaction time 10, 30, 60 and 180 min for FTS on 47%$Co_{SG}$-6%$Ce_{SG}$/$SiO_2$(aerosil).

The peaks at the retention times of 6.6 and 9.1 min represent $CH_4$ and CPr, respectively, compared with the results from Nie (Nie, 1996). Note that peaks at the retention times of 6.9 and 7.9 min are impurities in CPr.

*Data analysis* (Nie, 1996)

From the hydrocarbon analysis by FID, the signal intensity is proportional to the number of carbon atom in a molecule. Therefore :

$$\left(\frac{\dot{n}_{c,\,foV,\,j}}{\dot{n}_{cpr}}\right)_{prod} \propto \left(\frac{F_j}{F_{cpr}}\right)_{prod}$$

$$= \mathrm{N}_{\mathrm{cpr}}\left(\frac{F_j}{F_{cpr}}\right)_{prod}$$

$\dot{n}_j$ : molar flow (mol/min) of hydrocarbon product

$\dot{n}_{C\,\mathrm{Pr}}$ : molar flow (mol/min) of the reference gas (cyclopropane)

$\mathrm{F_j}$ : peak areas of hydrocarbon product

$\mathrm{F_{cpr}}$ : peak areas of the reference gas (cyclopropane)

$\mathrm{N_{cpr}}$ : number of carbon atom in the reference gas (cyclopropane)

*Calculation:*

From the reaction: the reference gas used is 0.5%CPr in $N_2$ (40.00 $cm^3$/min)
molar flow (mol/min) of 0.5%vol CPr 40.00 $cm^3$/min
molecular weight of CPr = 42.00 g/mol
density of CPr gas = $1.877\text{x}10^{-3}$ g/$cm^3$

$$Molar\ \ flow\ \ of\ \ \mathrm{CP}r \;=\; \frac{0.5x(1.877x10^{-3})}{42}\,x\,\frac{40}{100} \;=\; 0.89\text{x}10^{-5}\ \ mol/\min$$

Calculation of molar flow of $CH_4$ product
Example: peak areas of $CH_4$ = 4,651

peak areas of CPr = 135,555

$$\frac{Molar\ flow_{CH4}}{0.89x10^{-5}} = 3\left(\frac{4651}{135555}\right)$$

$\therefore$ Molar flow of $CH_4$ = $9.16 \times 10^{-7}$ mol/min

**Table 21** Peak area of FT products at different reaction times on 47%$Co_{SG}$ -6%$Ce_{SG}$ /$SiO_2$(aerosil).

| Ampoule sampling at reaction time (min) | Peak area | | Molar flow of $CH_4$* |
|---|---|---|---|
| | $CH_4$ | CPr | |
| 10 | 4,651 | 135,555 | $9.16 \times 10^{-7}$ |
| 30 | 2,861 | 127,246 | $6.00 \times 10^{-7}$ |
| 60 | 2,285 | 124,189 | $4.91 \times 10^{-7}$ |
| 180 | 2,110 | 80,768 | $6.97 \times 10^{-7}$ |

**Note** : * Molar flow of $CH_4$ are referred to molar flow of 0.5%CPr: $N_2$ carrier gas 5.00 $cm^3$/min

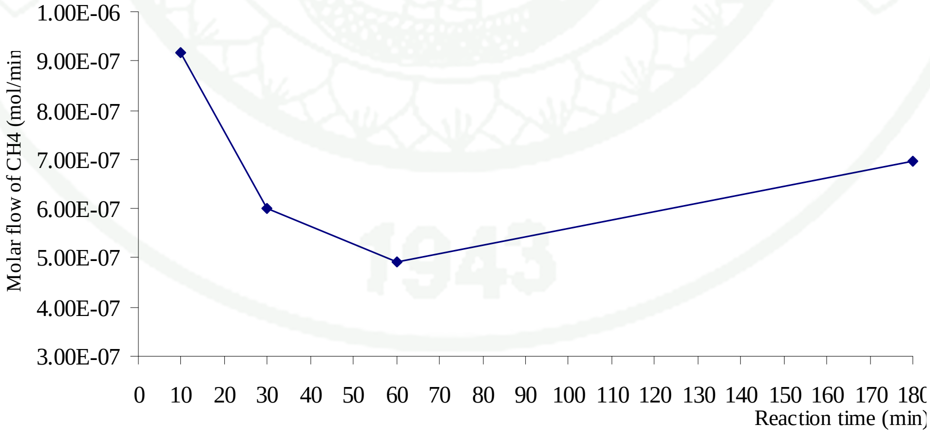

**Figure 53** Molar flow of $CH_4$ of FT synthesis on 47%$Co_{SG}$-6%$Ce_{SG}$ /$SiO_2$ (aerosil).

It shows that the experimental set up II, which was tested for FT synthesis on a known catalyst (47%$Co_{SG}$6%$Ce_{SG}SiO_2$(aerosil)) with the FT product analysis from the ITSS set up, can be used for further investigation. Suitable conditions have to be examined to produce the whole range of FT products.

Next, FT synthesis was tested on 10%$Co_{CP}$-1%$Ce_{CP}$/$TiO_2$ (anatase) 2.000 g (5.00 $cm^3$), 220 °C, 10 bar, $H_2$:CO = 2:1. The starting temperature of GC was 40 °C (Analysis with GC set up II condition III).

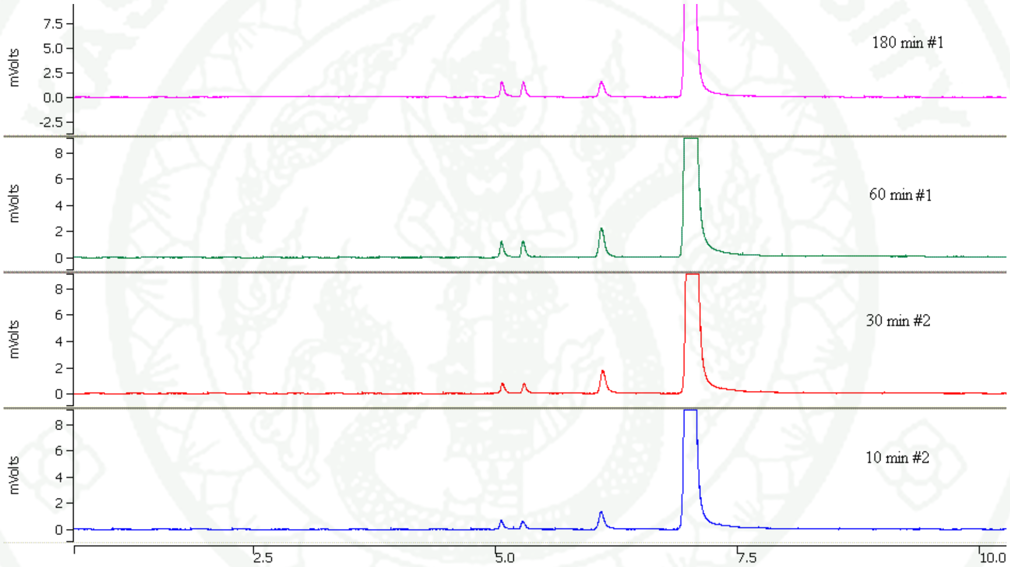

**Figure 54** Chromatograms of ampoule at reaction time 10, 30, 60 and 180 min of FT synthesis on 10%$Co_{CP}$-1%$Ce_{CP}$/$TiO_2$ (anatase).

The peaks at the retention time 5.1 and 7.0 min represent $CH_4$ and CPr, respectively, compared with the results from Nie (Nie, 1996).

**Table 22** Peak area of FT products at different reaction times on 10%Co$_{CP}$-1%Ce$_{CP}$/TiO$_2$ (anatase).

| Ampoule sampling at reaction time (min) | Peak area | | Molar flow of CH$_4$* |
|---|---|---|---|
| | CH$_4$ | CPr | |
| 10 | 2,384 | 336,775 | $1.89 \times 10^{-7}$ |
| 30 | 2,401 | 381,113 | $1.68 \times 10^{-7}$ |
| 60 | 3,548 | 465,626 | $2.03 \times 10^{-7}$ |
| 180 | 4,676 | 329,723 | $3.79 \times 10^{-7}$ |

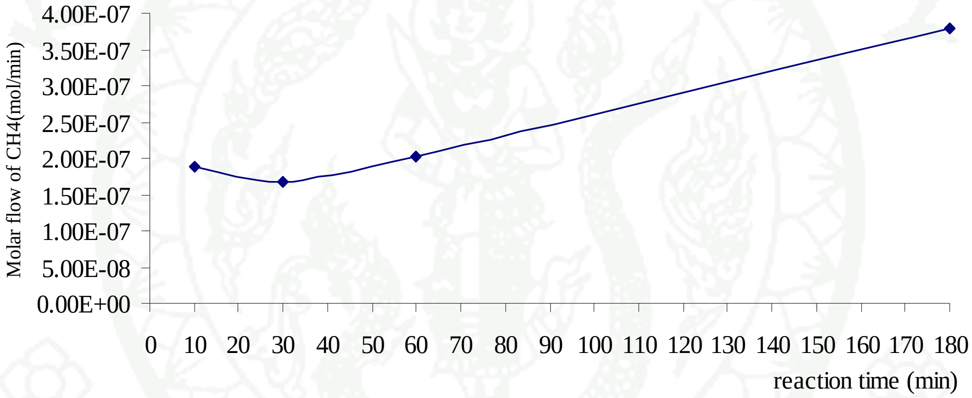

**Figure 55** Molar flow of CH$_4$ of FT synthesis on 10%Co$_{CP}$-1%Ce$_{CP}$/TiO$_2$ (anatase).

The FT synthesis on the prepared catalyst (10%Co$_{CP}$1%Ce$_{CP}$TiO$_2$ (anatase)) as a reference produced small molecule hydrocarbons almost in the same range of those produced from the known catalyst. The synthesis reaction time was rather short. Suitable conditions have to be further investigated.

# CONCLUSION

$TiO_2$ and cerium promoted $TiO_2$ were synthesized by the sol-gel method with different conditions, i.e. the ratios of water to Ti-alkoxide precursor (*H*), pH and cerium precursors.

The $TiO_2$ powder synthesized by the sol-gel with both low water content ($H$ = 4) and high water content ($H$ = 200) showing mixture phases of anatase and rutile, which were confirmed by XRD and XANES. The pH of the high water prepared solutions affected the phase ratios. The rutile phase increased with the decreased pH value, which was confirmed by XRD and Ti *K*-edge XANES.

Ce ions in the $TiO_2$ structure prevented the transformation of anatase to rutile, even though for those prepared from the high water content, which was observed only broad anatase peak from XRD. XANES spectra showed that the hydrolysis resulted from both the high and low cerium percentages of cerium precursors [$Ce(acac)_3$ and $Ce(NO_3)_3$] did not show significant effect on the mixture phases. Instead, the spectra showed the effects of the low and high water content. The low water content method ($H$ = 4) produced mainly the anatase phase. There was no evidence of $CeO_2$ from the Raman shifts of all samples, which indicated Ce ions stated in the $TiO_2$ structure.

Ce $L_3$-edge EXAFS spectra were used to observe the position of Ce ions in the $TiO_2$ structure from different Ce loading samples. The substitution sites and the interstitial sites of Ce ions in the structure were considered with the comparison of the simulation and experimental data. The 8%Ce/$TiO_2$ samples showed that the Ce ions in $TiO_2$ obtained the best fits using the interstitial defect simulations with Ce-O distances of 2.09 and 2.64 Å and Ce-Ti of 2.87 and 3.13 Å. The results from 30%Ce/$TiO_2$ samples prepared with the low water content showed that the Ce ions in $TiO_2$ exhibited both the interstitial and substitution defect simulations with different ratios. The samples prepared from $Ce(acac)_3$; CATi30-LW exhibited spectra fitted with interstitial: substitution ratios of 0.354: 0.646 and the samples prepared from

$Ce(NO_3)_3$; CNTi30-LW exhibited spectra fitted with interstitial: substitution ratios of 0.219: 0.781.

It could be assumed from EXAFS results that Ce ions in $TiO_2$ with different Ce percentages localized at different sites. The lower Ce percentage resided as an interstitial site whereas the higher resided both an interstitial site and the Ti-substitution site in $TiO_2$.

From the structural characterization of the sol-gel synthesized $TiO_2$ and $Ce/TiO_2$, it could be concluded that $TiO_2$ prepared from the low water content with mainly anatase phase should be used. As for the cerium promoted $TiO_2$, the lower percentage of cerium ions was considered due to the localized cerium ions at the interstitial sites in $TiO_2$, which should be more active than those at the substitution sites. Therefore 10%Co on 1%Ce/$TiO_2$-LW has been prepared and compared the cobalt reduction performance with 10%Co-1%Ce/$TiO_2$-anatase and 10%Co on $TiO_2$-anatase, it showed more completion of cobalt reduction at lower temperature. It confirms the assumption of Ce promoted $TiO_2$ reduces the interaction of Co-O-Ce. Ce as a promoter with Ce ions interstitial species in $TiO_2$ eases the $CoO_x$ reduction to Co.

The Fischer-Tropsch products analysis has been set up with the instantaneous total stream sampling (ITSS). The model substances of the Fischer-Tropsch products (i.e. natural gases, gasoline and diesel) have been tested and were analyzed effectively using a GC equipped with a polymethylsiloxane coated capillary column.

The Fischer-Tropsch experimental set up has been tested with a known catalyst $47\%Co_{SG}6\%Ce_{SG}47\%SiO_2$ (aerosil). The analysed Fischer-Tropsch product was $C_1$ together with cyclopropane as reference gas. The FT synthesis on the prepared catalyst ($10\%Co_{CP}1\%Ce_{CP}TiO_2$ (anatase)) as a reference produced small molecule hydrocarbons almost in the same range of those produced from the known catalyst. The synthesis reaction time was rather short. Suitable conditions have to be further investigated.

# LITERATURE CITED

Bare, S. R. 2003. **EXAFS data collection and analysis course**. National Synchrotron Research Center, Nakhon-Ratchasima

Batista, M.S., R.K.S. Santos, E.M. Assaf, J.M. Assaf and E.A. Ticianelli. 2003. Characterization of the activity and stability of supportedcobalt catalysts for the steam reforming of ethanol. **J. Power Sources**. 124: 99–103.

Bertole, C. J., C. A. Mims and G. Kiss. 2004. Support and rhenium effects on the intrinsic site activity and methane selectivity of cobalt Fischer–Tropsch catalysts. **J. Catal.** 221: 191–203.

Cano, F. M. 2006**. Manganese Promotion in Titania-Supported Cobalt Fischer-Tropsch Catalysis.** Ph.D. Thesis. Utrecht University. Netherlands.

Chen, L.X., T. Rajh, Z. Wang and M.C. Thurnauer. 1997. XAFS studies of surface structures of $TiO_2$ nanoparticles and photocatalytic reduction of metal ions. **J. Phys. Chem. B.** 101: 10688-10697.

Choi, H.C., Y.M.Jung and S.B. Kim. 2005. Size effects in the Raman spectra of $TiO_2$ nanoparticles. **Vib. Spectros.** 37:33-38.

Claeys, M. 1997. **Selektivität, Elementarschritte und kinetische Modellierung bei der Fischer-Tropsch-Synthese**. Ph.D. Thesis, Universität Karlsruhe. Germany.

Diehl, F. and A.Y. Khodakov. 2008. Promotion of cobalt Fischer-Tropsch catalysts with noble metals:a Review. **Oil & Gas Science and Technology**. 1-14.

Dijk, H. A.J. van. 2001. **The Fischer-Tropsch synthesis: A mechanistic study using transient isotopic tracing.** Ph.D. Thesis. Technische Universiteit Eindhoven. Eindhoven. Netherlands.

Dominguez, A., Y. Fernandez, B. Fidalgo, J.J. Pis, J.A. Menendez.  2008. Bio-syngas production with low concentrations of $CO_2$ and $CH_4$ from microwave-induced pyrolysis of wet and dried sewage sludge. **Chemosphere.** 70: 397-403.

Douglas, A.S., F.J. Holler and S.R. Crouch. 2007. **Principles of Instrumental Analysis.** 6th ed. Tomson Brooks/Cole. USA.

Duvenhage, D.J. and N.J. Coville. 2005. Effect of K, Mn and Cr on the Fischer Tropsch activity catalysts of Fe:Co/$TiO_2$. **Catal. Lett.**  104: 129-133.

Ertl. G., H. Knözinger and J. Weitkamp.  1999. **Preparation of solid catalysts.** Wiley-VCH, New York. 60-73.

Erzinger, J. 2000. What is Raman spectroscopy?. **Inorganic and isotope geochemistry** (online). Available: http://www.gfz-potsdam.de/pb4/pg2/equipment/raman/raman.html.

Farges, F., G. E. Brown, Jr. and J. J. Rehr 1997. Ti *K*-edge XANES studies of Ti coordination and disorder in oxide compounds: Comparison between theory and experiment. **Phys. Rev. B.** 56: 1809-1819.

Francisco, M.S.P. and V.R. Mastelaro. 2002. Inhibition of the anatase-rutile phase transformation with addition of $CeO_2$ to CuO- $TiO_2$ system: Raman spectroscopy, X-ray diffraction and textural studies. **Chem. Mater.** 14: 2514-2518.

Fonda E., Andreatta D., Colavita P.E. and Vlaic G. 1999. EXAFS analysis of the $L_3$ edge of Ce in $CeO_2$: effects of multi-electron excitations and final-state mixed valence. **J. Synchrotron Rad.** 6:34-42.

George, G.N. and I.J. Pickering. 1993. **EXAFSPAK- A Suite of Computer Programs for Analysis of X-ray Absorption Spectra**. Menlo Park. Canada.

Gonzalez, R.D., T. Lopez and R. Gomez. 1997. Sol-gel preparation of supported metal catalyst. **Catal. Today.** 35: 293 317.

Hiroshi, H., H. Tanaka and K. Fujimoto. 2007. Studies on catalytic performance of precipitated iron/silica catalysts for Fischer–Tropsch Synthesis**. Appl. Catal. A.** 328: 117–123.

Hsu, J.-P. and A. Nacu. 2003. On the factors influencing the preparation of nanosized titania sols. **Langmuir.** 19: 4448-4454.

Hu, Y., H.-L. Tsai and C.-L. Huang. 2003. Effect of brookite phase on the anatase-rutile transition in titania nanoparticles. **J. Europ. Ceram. Soc.** 23: 691-696.

Iglesia, E. 1997. Design, synthesis, and use of cobalt-based Fischer-Tropsch synthesis catalysts. **Appl. Catal. A** 161: 59-78.

Jacobs, G., T. K. Das, Y.Zhang, J. Li, G. Racoillet and B. H. Davis. 2002. Fischer–Tropsch synthesis: support, loading, and promoter effects on the reducibility of cobalt catalysts. **Applied Catalysis A: General** 233: 263–281.

Jalama, K., N. J. Coville, D. Hildebrandt, D. Glasser, L. L. Jewell, J. A. Anderson, S. Taylor, D. Enache and G. J. Hutchings. 2007. Effect of the addition of Au on $Co/TiO_2$ catalyst for the Fischer Tropsch reaction. **Top. Catal.** 44: 129-136

Jiu, J., S. Isoda, M. Adachi and F. Wang. 2007. Preparation of $TiO_2$ nanocrystalline with 3–5 nm and application for dye-sensitized solar cell. **J. Photochem. Photobiol. A: Chem.** 189: 314–321.

Jongsomjit, B., T. Wongsalee and P. Praserthdam. 2005. Characteristics and catalytic properties of Co/$TiO_2$ for various rutile:anatase ratios. **Catal. Commn.** 6: 705–710.

Jongsomjit, B., T. Wongsalee and P. Praserthdam. 2006. Catalytic behaviors of mixed $TiO_2$-$SiO_2$-supported cobalt Fischer–Tropsch catalysts for carbon monoxide hydrogenation. **Mater. Chem. Phys.** 97: 343–350.

Khodakov, A. Y. 2008. Fischer-Tropsch synthesis: Relations between structure of cobalt catalysts and their catalytic performance. **Catal. Today** doi:10.1016/j.cattod.2008.10.036.

Khodakov, A. Y, W. Chu and P. Fongarland. 2007. Advances in the Development of Novel Cobalt Fischer-Tropsch Catalysts for Synthesis of Long-Chain Hydrocarbons and Clean Fuels. **Chem. Rev.** 107: 1692-1744.

Kikuchi, H., M. Kitano, M. Takeuchi, M. Matsuoka, M. Anpo and P. V. Kamat. 2006. Extending the photoresponse of $TiO_2$ to the visible light region: Photoelectrochemical behavior of $TiO_2$ thin films prepared by the radio frequency magnetron sputtering deposition method. **J. Phys. Chem. B** 110: 5537-5541.

Kitazawa, S., Y. Choi, S. Yamamoto and T. Yamaki. 2006. Rutile and anatase mixed crystal $TiO_2$ thin films prepared by pulsed laser deposition. **Thin Solid Films** 515: 1901–1904.

Kroschwitz, I. and M. Howe-Grant. 1996. **Kirk-Othmer Encyclopedia of Chemical Technology**. Wiley & Sons, New York, 4th ed.

Krumeich, F. 2004. Bragg description of diffraction. **Electron microscopy** (online). Available: http://www.microscopy.ethz.ch/bragg.htm.

Kuznetsova, I., N., V. Blaskov and L. Znaidi. 2007. Study on the influence of heat treatment on the crystallographic phases of nanostructured $TiO_2$ films. **Mater. Sci. Eng. B** 137: 31–39.

Lewis, I. R. and H. G. M. Edwards. 2001. **Handbook of Raman Spectroscopy**. Marcel Dekker, Inc., New York.

Li, J., G. Jacobs,Y. Zhang, T. Das and B. H. Davis. 2002. Fischer–Tropsch synthesis :effect of small amounts of boron, ruthenium and rhenium on $Co/TiO_2$ catalysts. **Appl. Catal. A.** 223: 195–203.

Lin, J. and Yu J.C. 1998. An investigation on photocatalytic activities of mixed $TiO_2$-rare earth oxides for the oxidation of acetone in air. **J. Photochem. Photobiol. A.** 116:63-67.

Luca, V., L.H. Tracey, K.R. Nicholas and Russel F.H. 1999. NMR and X-ray absorption study of lithium intercalation in micro- and nanocrystalline anatase. **Chem. Mater.** 11: 2089-2102.

Luo, M., J. Chen, L. Chen, J. Lu, Z. Feng and C. Li. 2001. Structure and redox properties of $Ce_xTi_{1-x}O_2$ solid solution. **Chem. Mater.** 13: 197-202.

Lynch, L., O. Ducreux, D. Uzio and B. Rebours. 1998. X-ray studies of metal-support interaction in catalysts. Available Source: http://www.anl.gov/PCS/acsfuel/preprint%20archive/Files/45_2_SAN%20FRANCISCO_03-00_0325.pdf

Mahshid, S., M. Askari and M. S. Ghamsari. 2007. Synthesis of $TiO_2$ nanoparticles by hydrolysis and peptization of titanium isopropoxide solution. **J. Mater. Process. Technol.** 189: 296–300.

Moradi, G. R., M.M. Basir, A. Taeb and A. Kiennemann. 2003. Promotion of Co/$SiO_2$ Fischer–Tropsch catalysts with zirconium. **Catal. Commun.** 4: 27–32.

Madikizela, N.N. and N.J. Coville. 2002. A study of Co/Zn/$TiO_2$ catalysts in the Fischer–Tropsch reaction. **J. Mol. Catal. A.** 181: 129–136.

Madikizela-Mnqanqeni, N. N. and N. J. Coville. 2007. The preparation and study of sol–gel synthesized Co/Zn/$TiO_2$ Fischer–Tropsch catalysts. **Appl. Catal. A.** 317: 195–203.

Mahshid, S., M. Askari and M. S. Ghamsari. 2007. Synthesis of $TiO_2$ nanoparticles by hydrolysis and peptization of titanium isopropoxide solution. **J. Mater. Process. Technol.** 189: 296–300.

Martínez, A., C. López, F. Márquez and I. Díaz. 2003. Fischer–Tropsch synthesis of hydrocarbons over mesoporous Co/SBA-15 catalysts: the influence of metal loading, cobalt precursor, and promoters. **J. Catal.** 220: 486–499.

Matsuo, S., N. Sakaguchi and H. Wakit. 2005. Pre-edge feature of Ti K-edge x-ray absorption near-edge structure of the local structure of sol-gel titanium oxides. **Anal. Sci.** 21: 805-809.

Mohamed, M. M., W.A. Bayoumy, M. Khairy and M.A. Mousa. 2007. Synthesis of micro–mesoporous $TiO_2$ materials assembled via cationic surfactants: Morphology, thermal stability and surface acidity characteristics. **Micropor. Mesopor. Mater.** 103: 174–183.

Morales, F., Frank M.F.de Groot , O.L.J.Gijzeman, A. Mens, O. Stephan and B.M.Weckhuysen. 2005. Mn promotion effects in Co/$TiO_2$ Fischer–Tropsch catalysts as investigated by XPS and STEM-EELS. **J. Catal.** 230: 301–308.

Morales, F., D. Grandjean, A. Mens, F. M. F. de Groot, and B. M. Weckhuysen. 2006. X-ray Absorption Spectroscopy of Mn/Co/$TiO_2$ Fischer-Tropsch Catalysts: Relationships between Preparation Method, Molecular Structure, and Catalyst Performance**. J. Phys. Chem. B** 110: 8626-8639.

Niemantsverdriet, J. W. 1995. **Spectroscopy in catalysis**. VCH., Weinheim.

Ni, M., D.Y.C. Leung, M.K. H. Leung and K. Sumathy. 2006. An overview of hydrogen production from biomass. **Fuel Process. Technol.** 87: 461–472.

Nie, Z. 1996. **Anfangsaktivität und selektivität der Fischer-Tropsch-Synthese mit modifizierten Kobalt und Nickelkatalysatoren.** Ph.D. Thesis, Universität Karlsruhe. Germany.

Oh, S.-M. and T. Ishigaki. 2004. Preparation of pure rutile and anatase $TiO_2$ nanopowders using RF thermal plasma. **Thin Solid Films** 457: 186–191.

Oskam, G., A. Nellore, R.L. Penn and P.C. Searson. 2003. The growth kinetics of $TiO_2$ nanoparticles from titanium (IV) alkoxide at high water/titanium ratio. **J. Phys. Chem. B**. 107: 1734-1738.

Ohashi, T., S. Yamazaki, T. Tokunaga, Y. Arita, T. Matsui, T. Harami and K. Kobayashi. 1998. EXAFS study of $Ce_{1-x}Gd_xO_{2-x/2}$. **Solid State Ionics.** 113–115: 559–564.

Patterson A.L. 1939. The Scherrer Formula for X-ray Particle Size Determination. **Phys. Rev.** 56:978 982.

Purans, J., A. Azens and C.G. Granqvist. 2001. X-ray absorption study of Ce–Ti oxide films. **Electrochim. Acta**. 46: 2055-2058.

Rattanakam, R. 2005. **The influence of cerium ions and the hydrolysis effect in sol-gel preparation on structure and catalytic property of Ce/TiO$_2$ oxidative catalyst**. M.S. Thesis, Kasetsart University.

Rehr, J.J. and R.C. Albers. 2000. Theoretical approaches to X-ray absorption fine structure. **Rev. Mod. Phys.** 72: 621-654

Riva, R., H. Miessner, R. Vitali and G.D. Piero. 2000. Metal–support interaction in Co/SiO$_2$ and Co/TiO$_2$. **Appl. Catal. A.** 196: 111–123.

Rohr, F., O.A. Lindvåg, A. Holmen and E.A. Blekkan. 2000. Fischer–Tropsch synthesis over cobalt catalysts supported on zirconia-modified alumina. **Catal. Today.** 58: 247–254.

Schlabach, S., D.V. Szabo, D. Vollath, P. de la Presa and M. Forker. 2007. Zirconia and titania nanoparticles studied by electric hyperfine interactions, XRD and TEM. **J. Alloys Comp.** 434–435: 590–593.

Schulz, H. 1999. Short history and present trends of Fischer–Tropsch synthesis. **Appl. Catal. A.** 186: 3–12.

Schulz, H. 2003. Major and minor reactions in Fischer–Tropsch synthesis on cobalt catalysts. **Top. Catal.** 26: 73-85.

Schulz, H., E. Steen and M. Claeys. 1995. Specific inhibition as the kinetic principle of the Fischer-Tropsch synthesis. **Top. Catal.** 2: 223-234.

Schulz, H., T. Riedel and G. Schaub. 2005. Fischer–Tropsch principles of co-hydrogenation on iron catalysts. **Top. Catal**. 32: 117-124.

Schulz, H., W. BÖhringer, C.P. Kohl, N.M. Rahman and A. Will. 1984. **Development and application of capillary GC Total Stream Sampling Technique for Gas/Vapor multi component mixtures (Report)**. German Society for Petroleum Sciences and Coal Chemistry. Universität Karlsruhe. Germany.

Sekiya, T., S. Ohta, S. Kamei, M. Hanakawa and S. Kurita. 2001. Raman spectroscopy and phase transition of anatase $TiO_2$ under high pressure. **J. Phys. Chem. Solids.** 62: 717-721.

Spurr, R.A. and Myers H. 1957. Ouantitative analysis of anatase-rutile mixture with an X-ray diffractometer. **Anal. Chem.** 29: 760-762.

Storsæter, S., Ø. Borg, E.A. Blekkan, B. Tøtdal and A. Holmen. 2005. Fischer–Tropsch synthesis over Re-promoted Co supported on $Al_2O_3$, $SiO_2$ and $TiO_2$: Effect of water. **Catal. Today**. 100: 343–347.

Subiranas, A.M. 2008. **Combining Fischer-Tropsch Synthesis (FTS) and hydrocarbon teactions in one reactor.** Ph.D. Thesis, Universitat Fridericiana Karlsruhe. Germany.

Swamy, V., B.C. Muddle and Q. Dai. 2006. Size-dependent modifications of the Raman spectrum of rutile $TiO_2$. **Appl. Phys. Lett.** 89: 163118.

Wang, H., J.L. Ye, Y. Liu, Y.D. Li and Y.N. Qin. 2007. Steam reforming of ethanol over $Co_3O_4/CeO_2$ catalysts prepared by different methods. **Catal. Today** 129: 305–312.

Xu, Y.-H., H.-R. Chen, Z.-X. Zeng and B. Lei. 2006. Investigation on mechanism of photocatalytic activity enhancement of nanometer cerium-doped titania. **Appl. Surf. Sci.** 252: 8565–8570.

Xiong, H., Y. Zhang, K. Liew and J. Li. 2005. Catalytic performance of zirconium-modified Co/$Al_2O_3$ for Fischer–Tropsch synthesis. **J. Mol. Catal. A.** 231: 145–151.

Yang, S., W. Zhu, Z. Jiang, Z. Chen and J. Wang. 2006. The surface properties and the activities in catalytic wet air oxidation over $CeO_2$–$TiO_2$ catalysts. **Appl. Surf. Sci.** 252: 8499–8505.

Yates, I. C. and C. N. Satterfield. 1992. Hydrocarbon Selectivity from Cobalt Fischer-Tropsch Catalysts. **Energy & Fuels** 6: 308-314.

Yeung, K.L., S.T. Yau, A.J. Maira, J.M. Coronado, J. Soria and P.L. Yuea. 2003. The influence of surface properties on the photocatalytic activity of nanostructured $TiO_2$. **J. Catal.** 219: 107-116.

Yu, H.F. and S.M. Wang. 2000. Effects of water content and pH on gel-derived $TiO_2$-$SiO_2$. **J. Non-Crys . Solids.** 261:260 267.

Zhang, Q., L. Gao and J. Guo. 2000. Effect of hydrolysis conditions on morphology and crystallization of nanosized $TiO_2$ powder. **J. Eur. Ceram. Soc.** 20: 2153-2158.

Zhang, Q., Y., L. Hou, J. W. Tierney and I. Wender. 2005. Acetylenes as probes in the Fischer–Tropsch Reaction. **Top. Catal.** 32: 125-133.

# APPENDICES

# Appendix A

The drawing of ampoule breaker

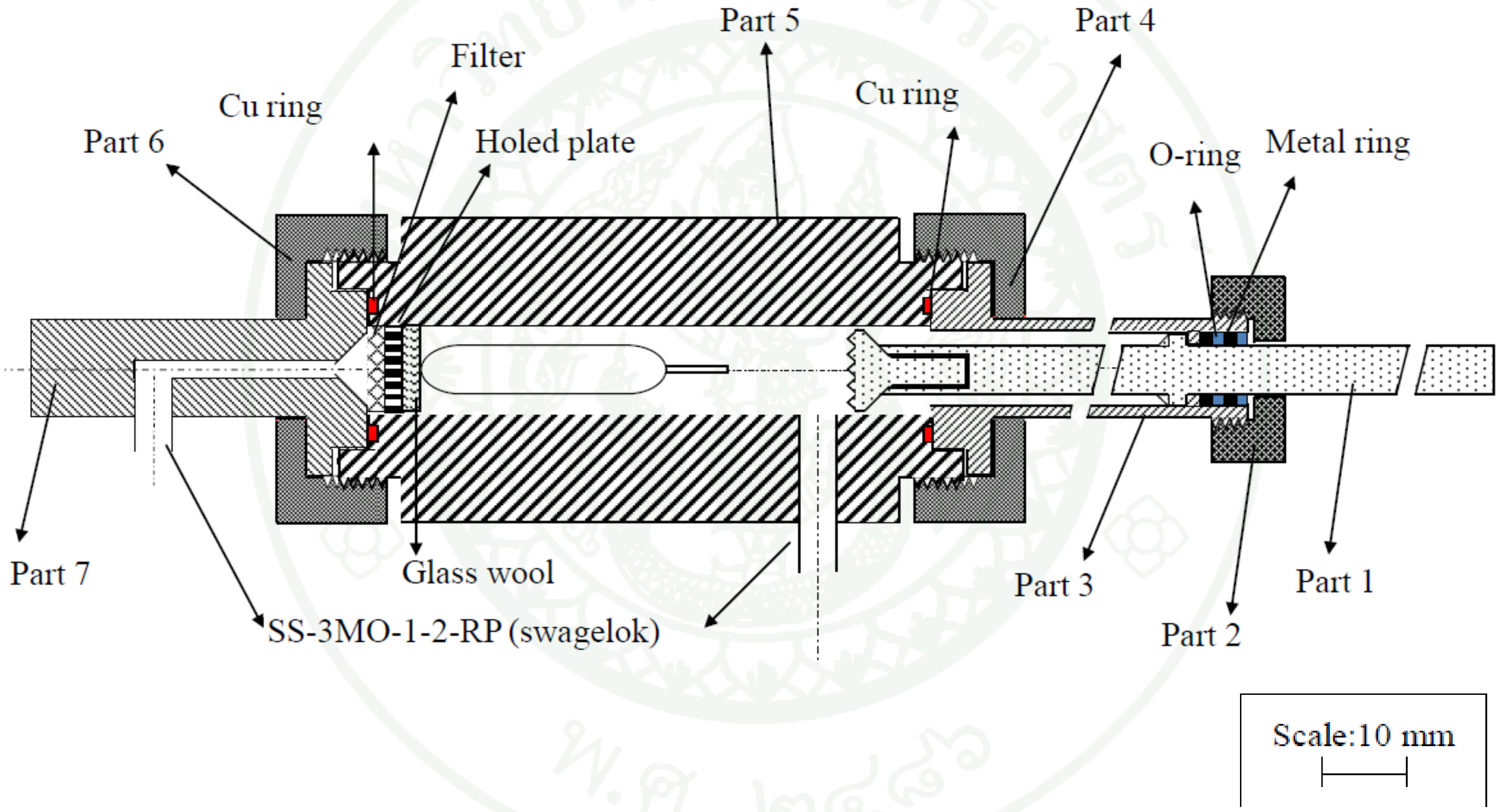

**Figure A1** Drawing of Ampoule breaker.

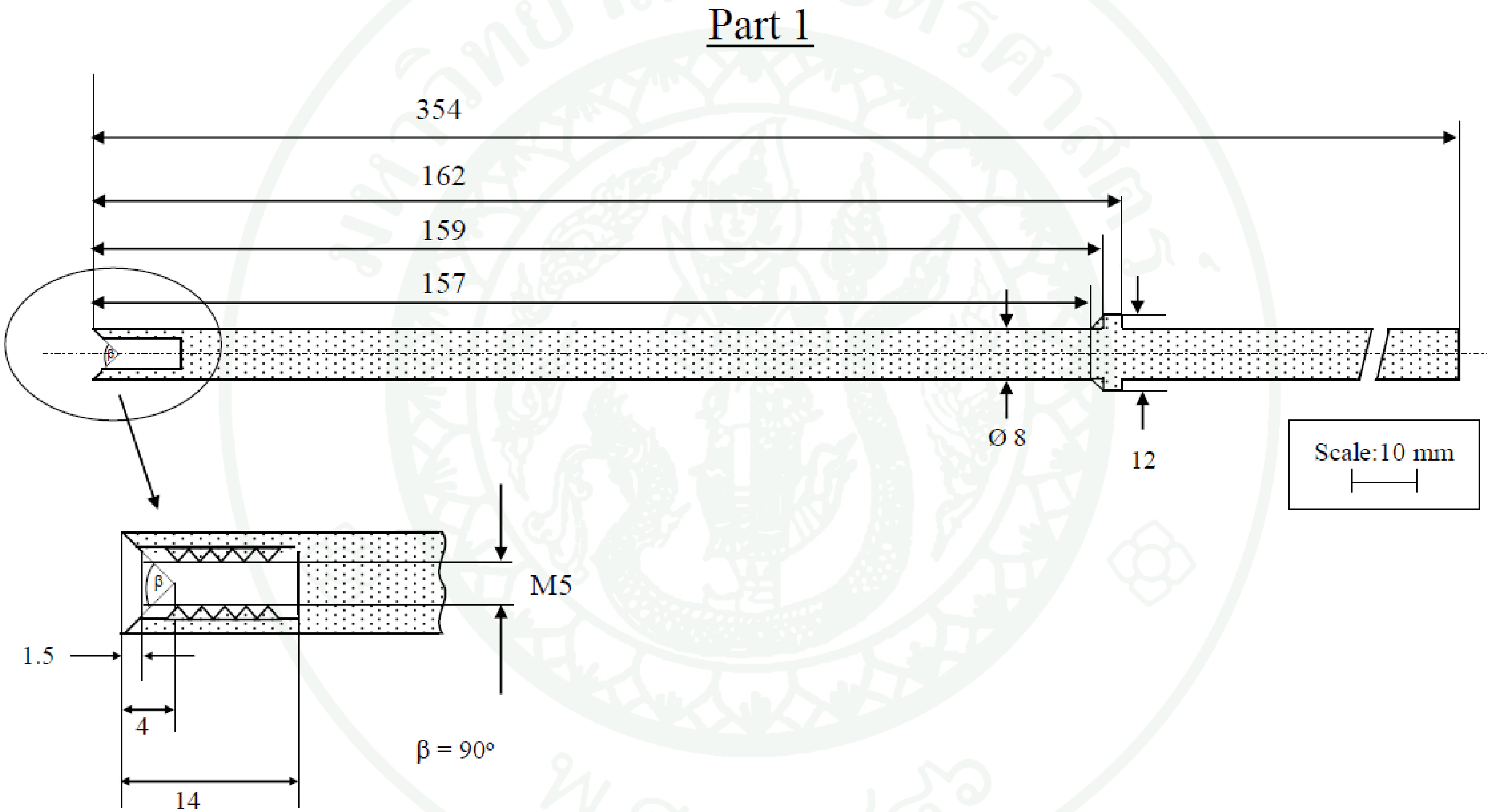

**Figure A2** Part 1 of Ampoule breaker.

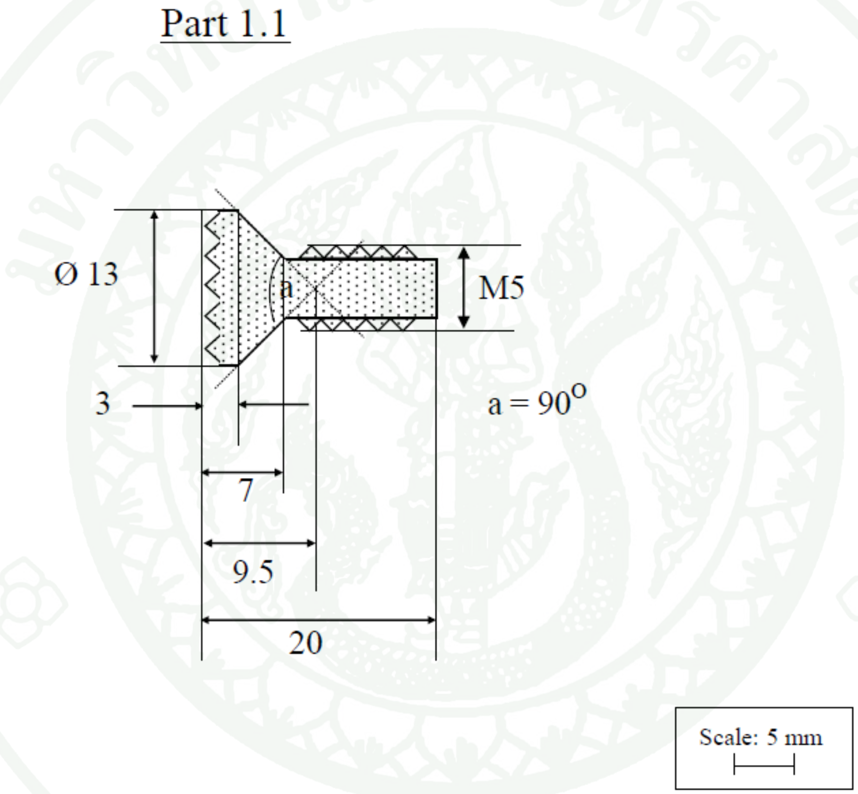

**Figure A3** Part 1.1 of Ampoule sampler.

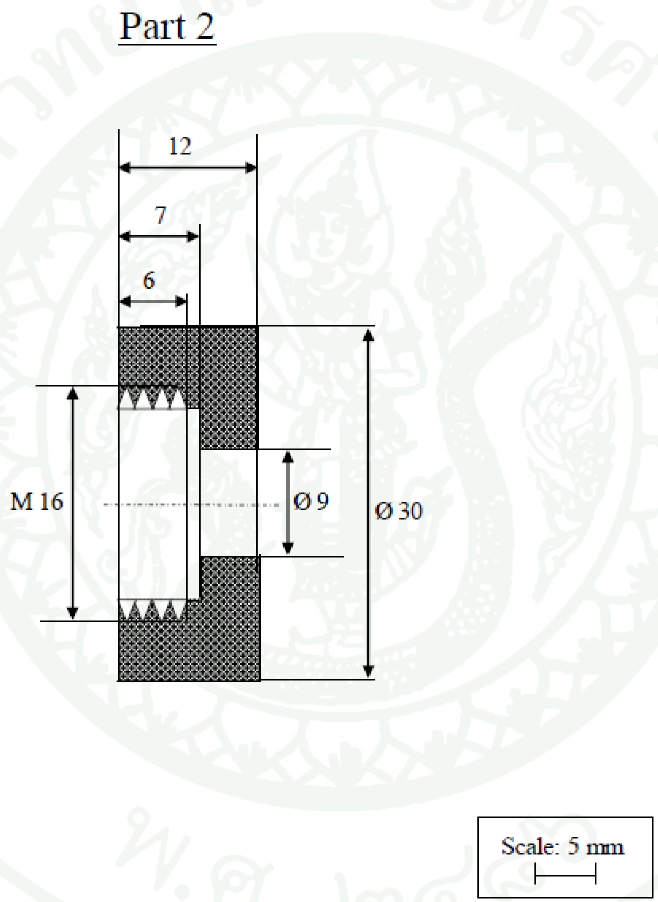

**Figure A4** Part 2 of Ampoule sampler.

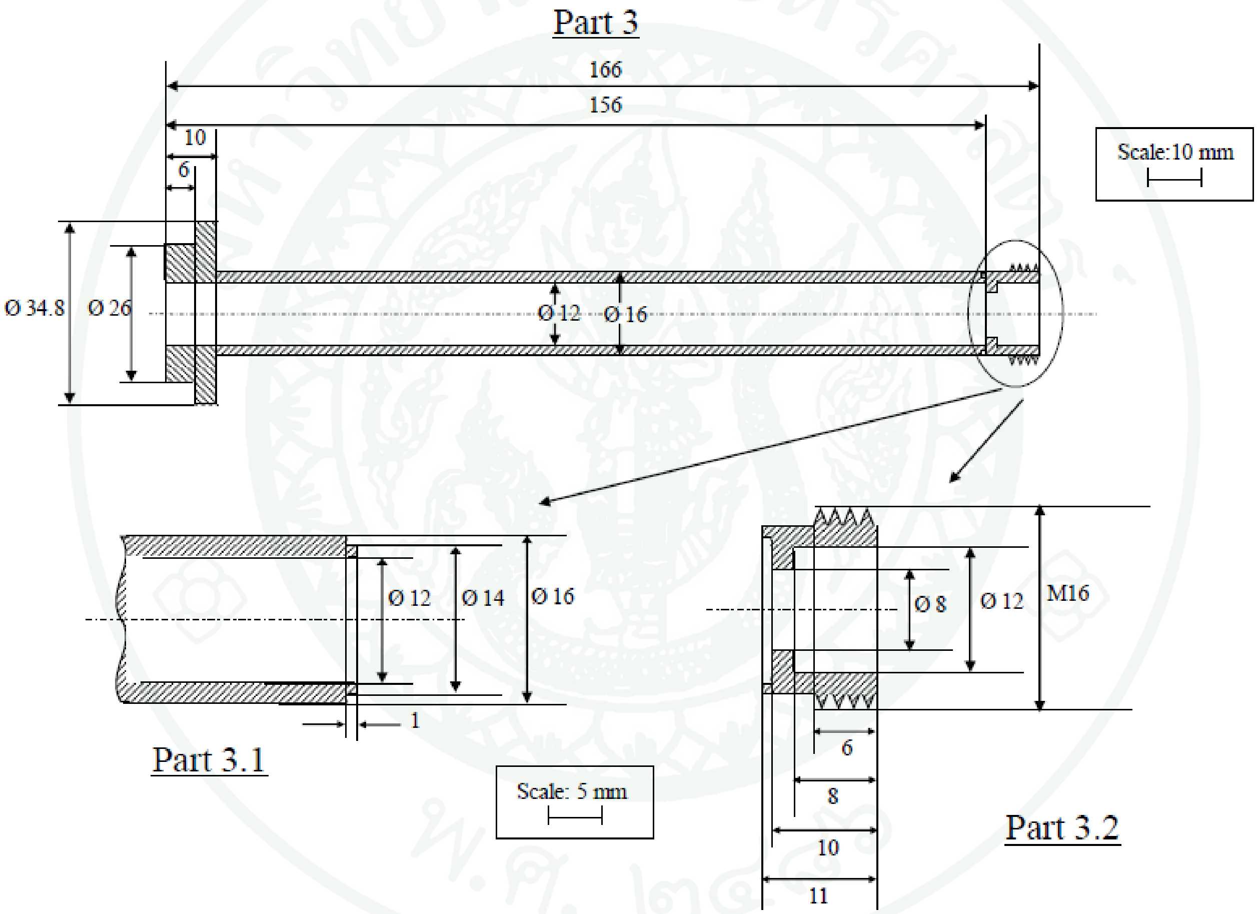

**Figure A5** Part 3 of Ampoule sampler.

## Part 4

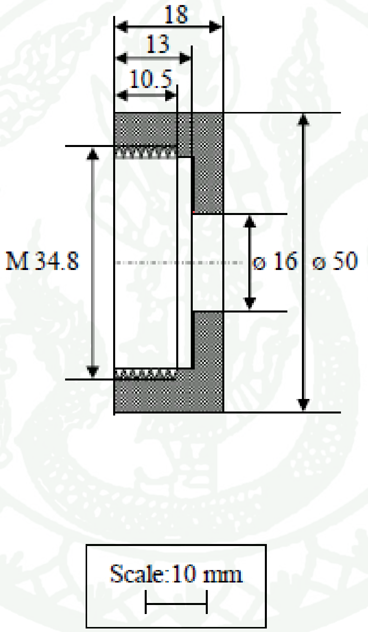

**Figure A6** Part 4 of Ampoule sampler.

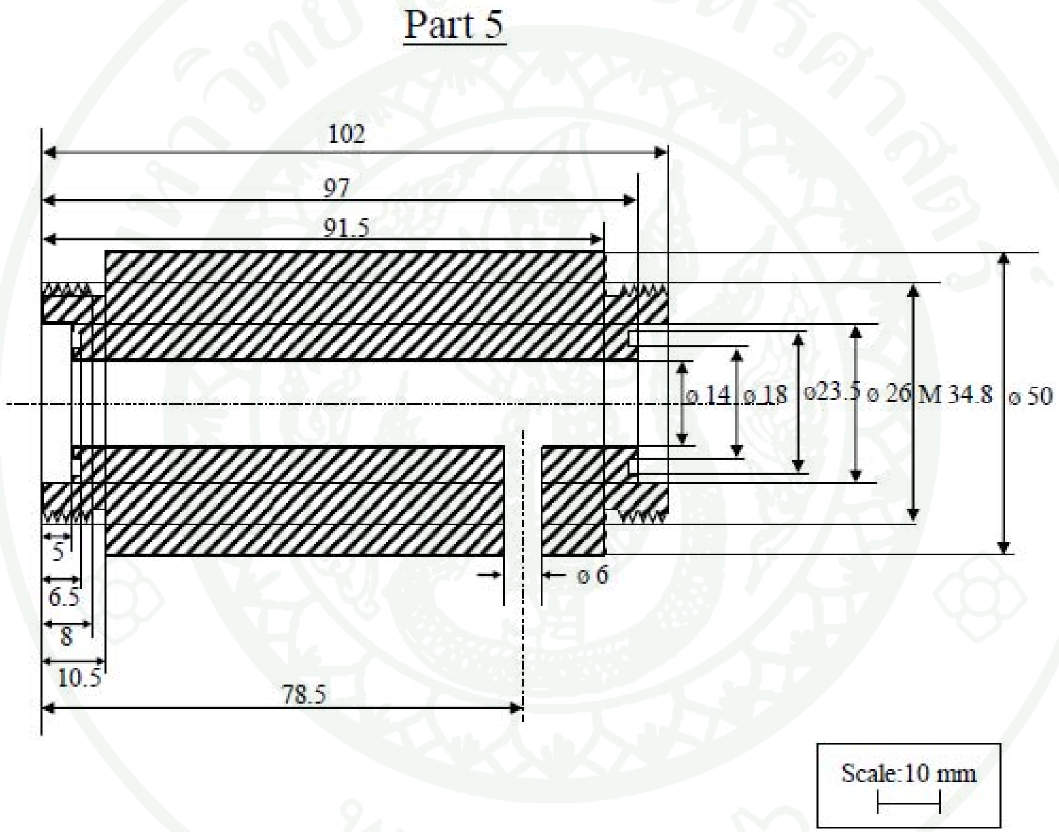

**Figure A7** Part 5 of Ampoule sampler.

Part 6

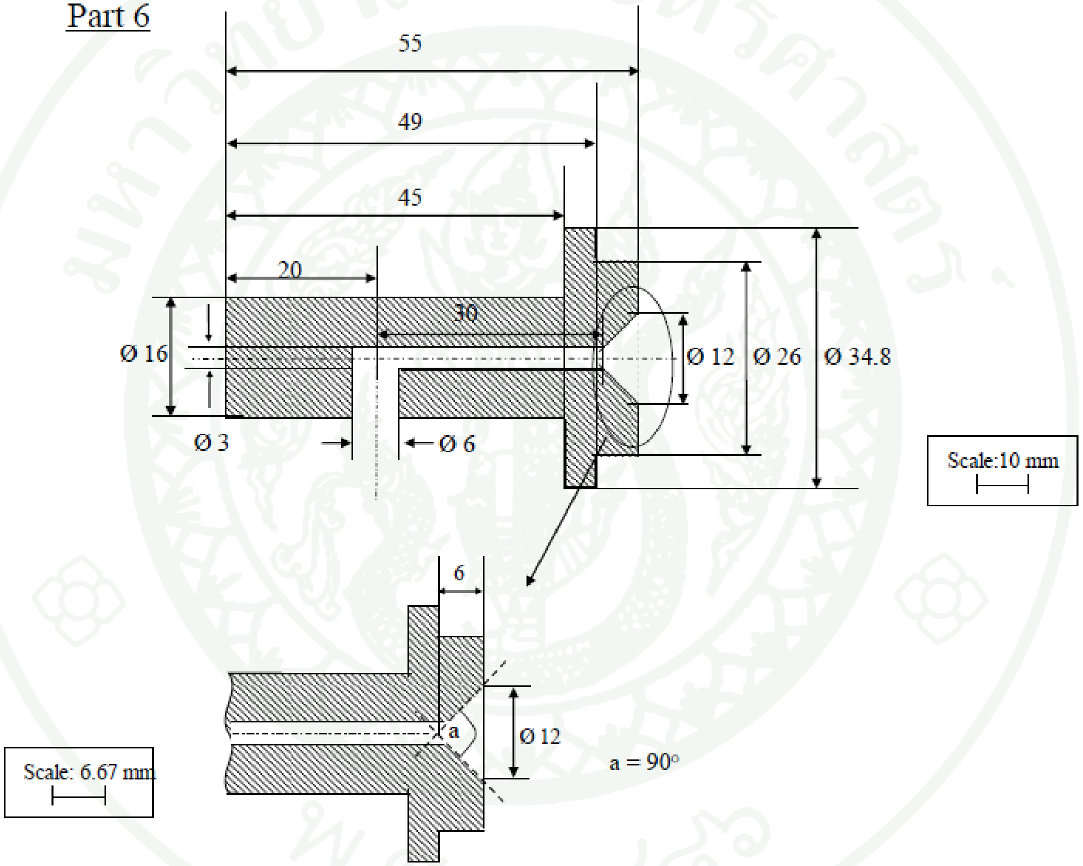

**Figure A8** Part 6 of Ampoule sampler.

# Appendix B

The drawing of ampoule sampler

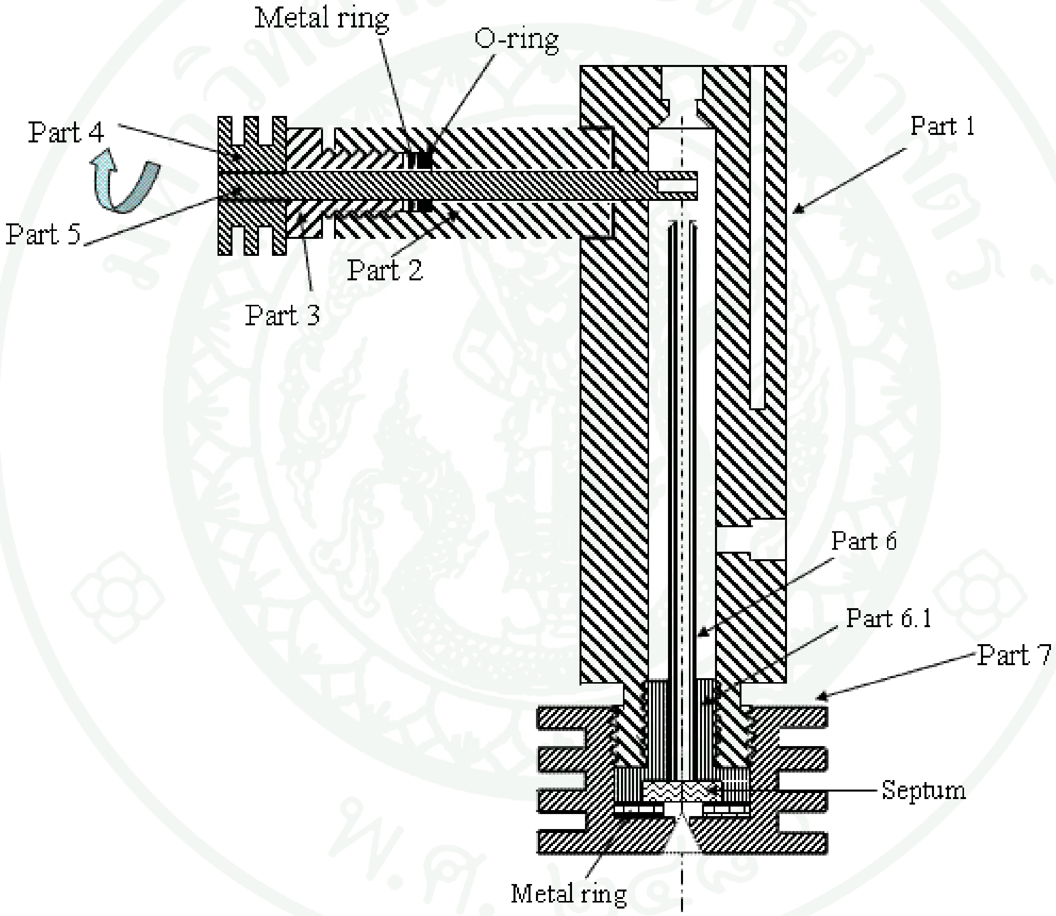

**Figure B1** Drawing of ampoule sampler.

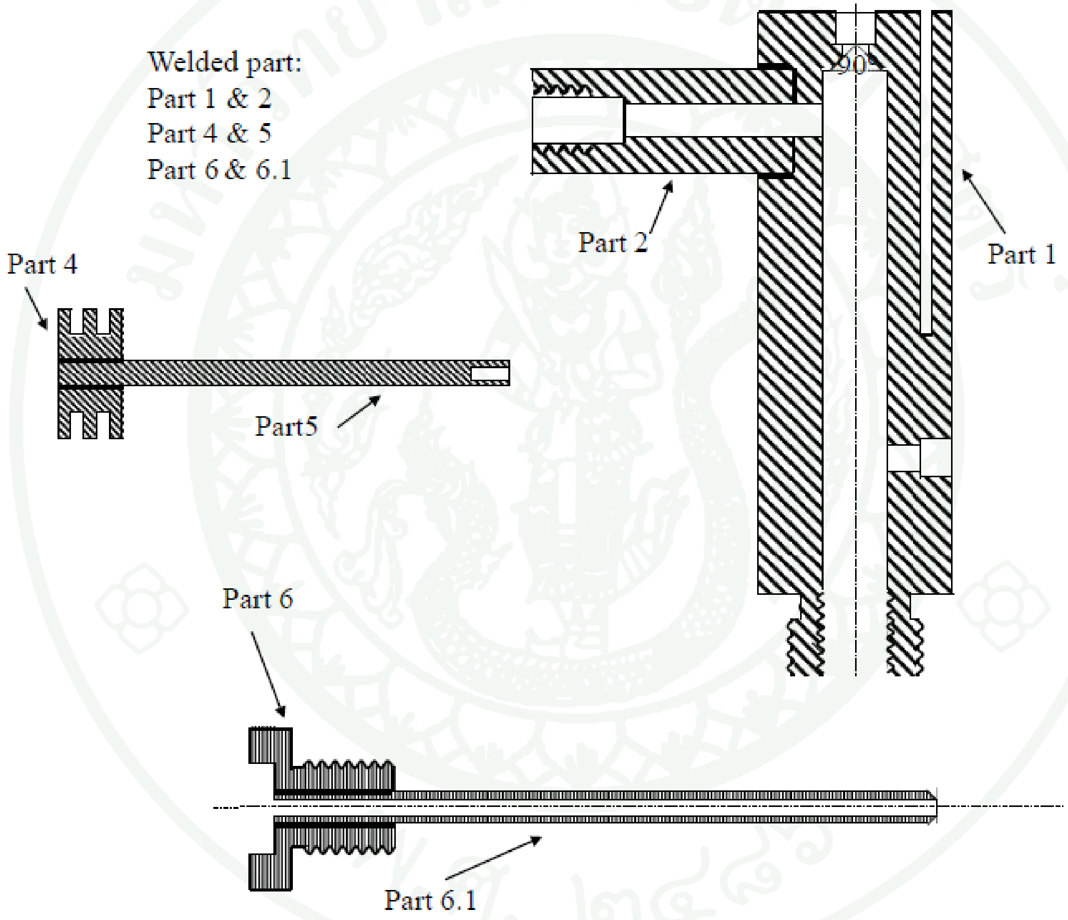

**Figure B2** Welded parts of ampoule sampler.

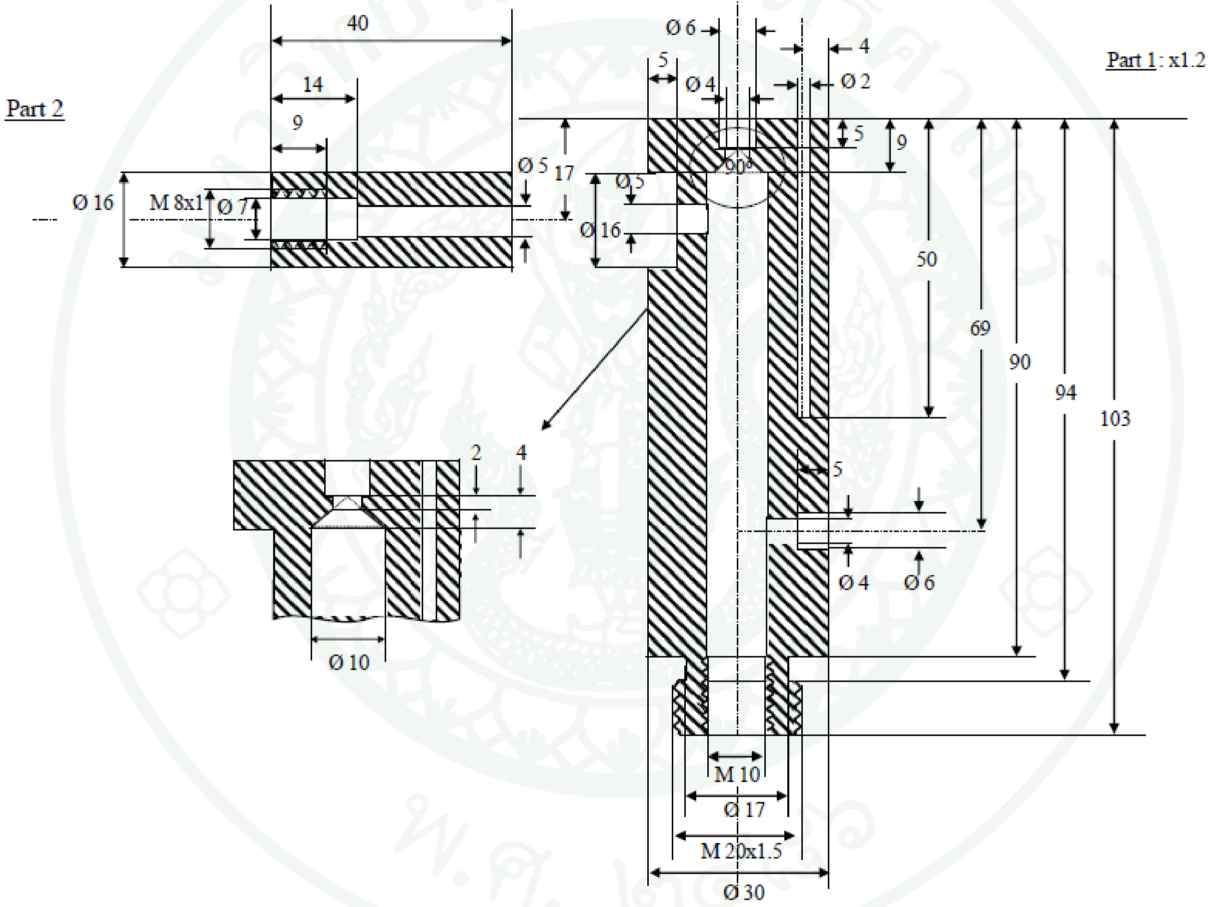

**Figure B3** Part 1 and 2 of ampoule sampler.

Part 3 : x2

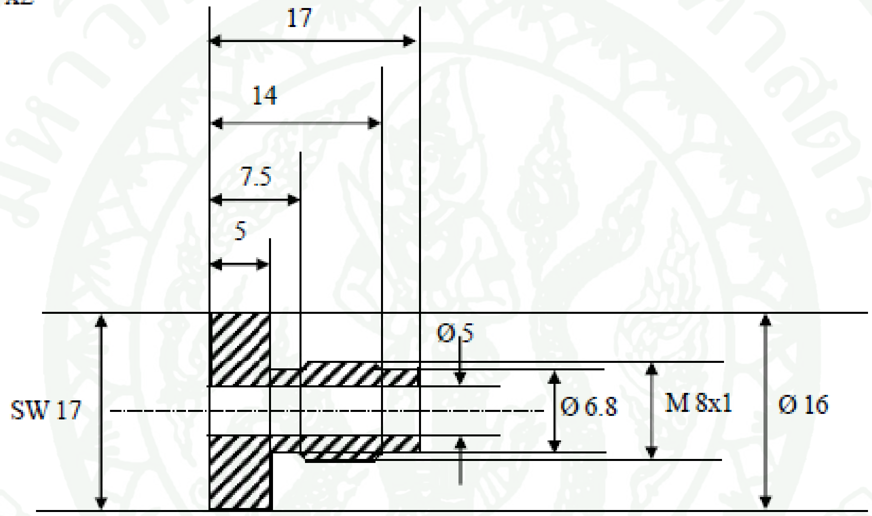

**Figure B4** Part 3 of ampoule sampler.

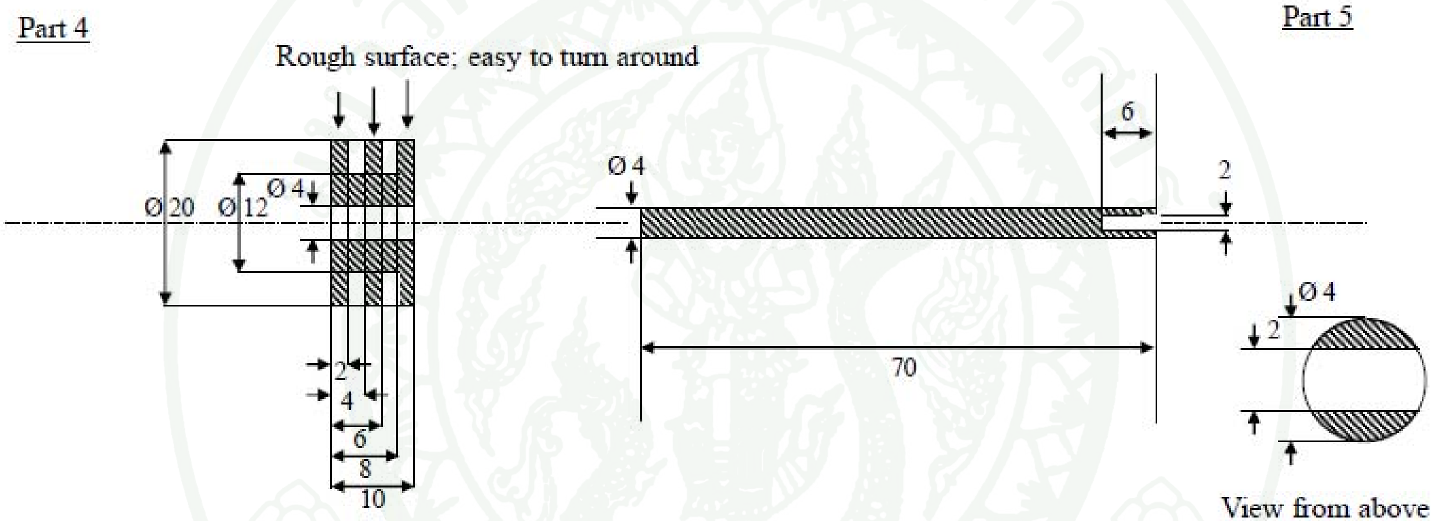

**Figure B5** Part 4 and 5 of ampoule sampler.

Part 6

: x2

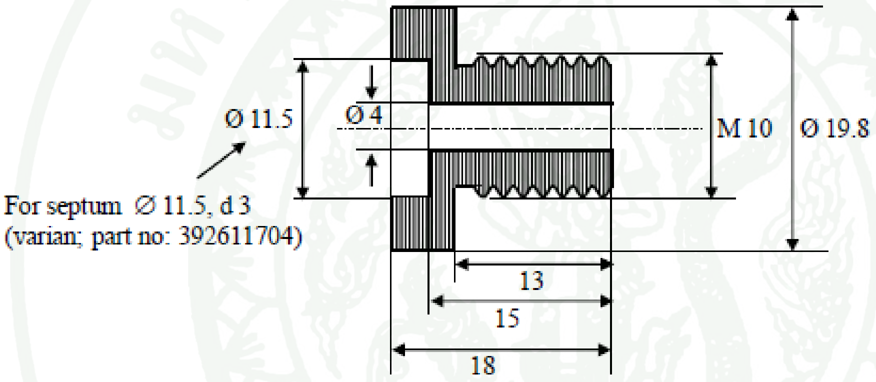

For septum ∅ 11.5, d 3
(varian; part no: 392611704)

Part 6.1

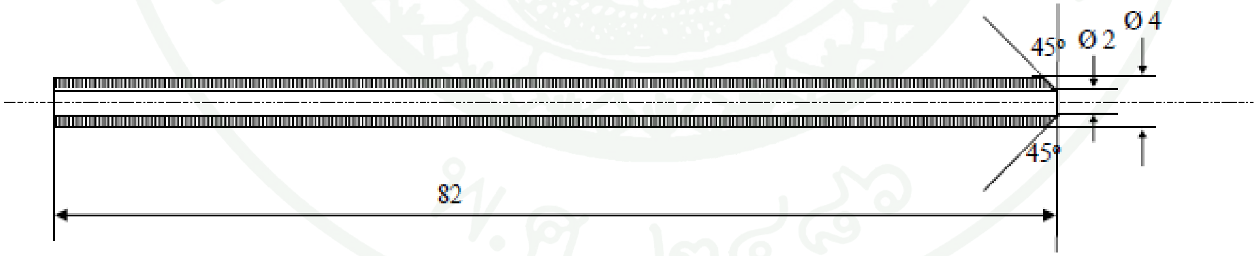

**Figure B6** Part 6 and 6.1 of ampoule sampler.

Part 7x2

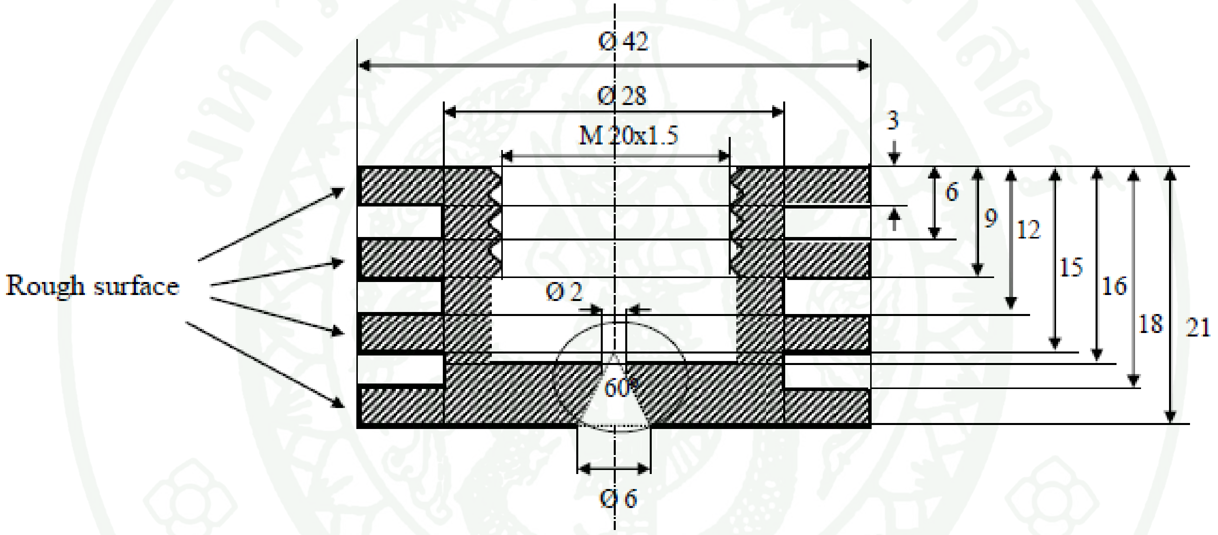

**Figure B7** Part 7 of ampoule sampler.

Metal ring

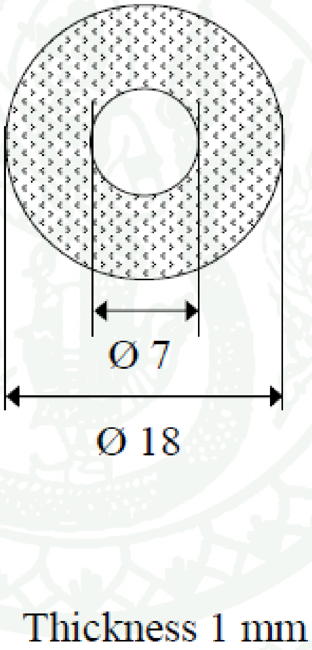

**Figure B8** Metal ring of ampoule sampler.

# Appendix C

The drawing of reactor

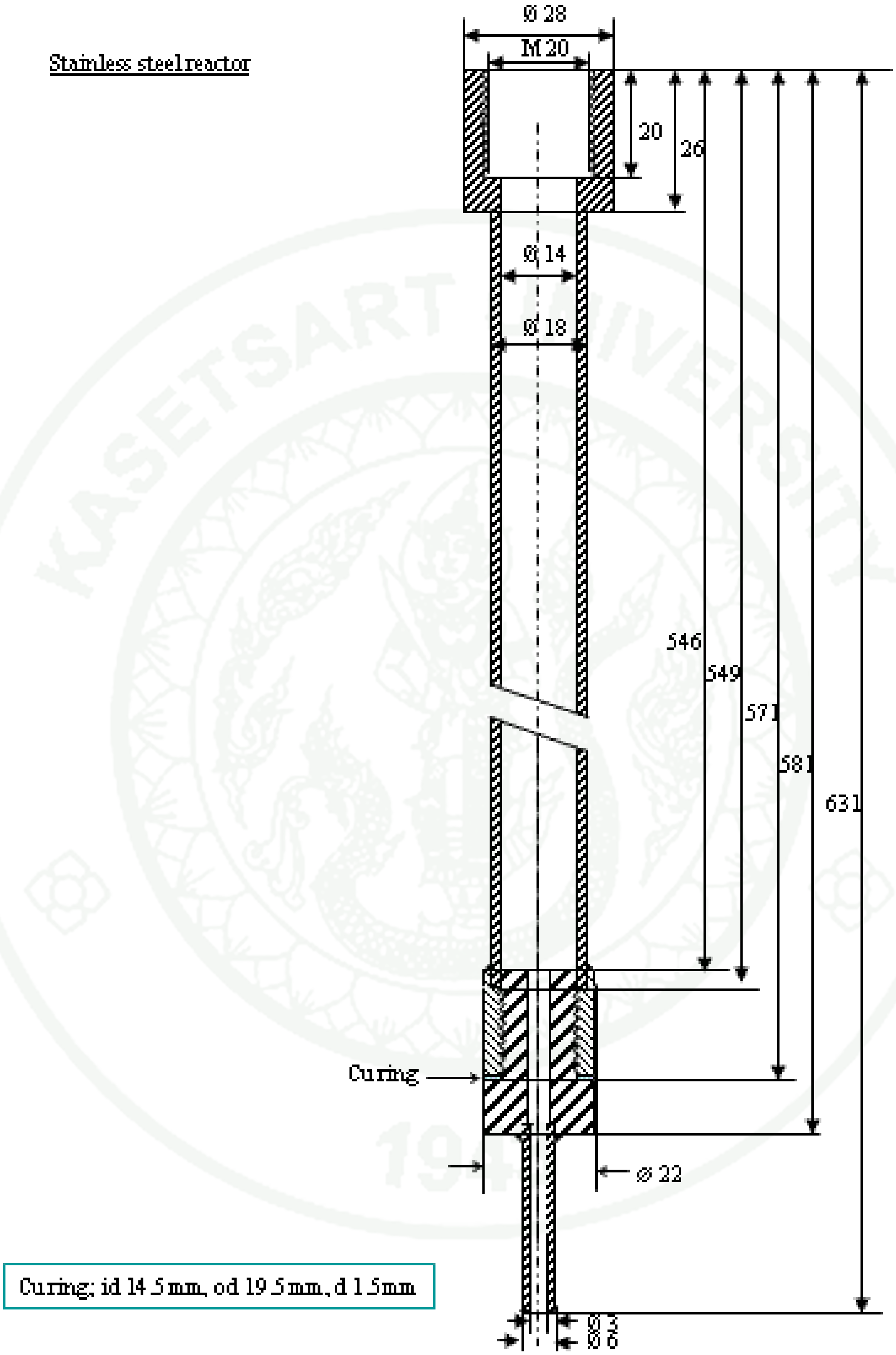

**Figure C1** Drawing of stainless steel reactor.

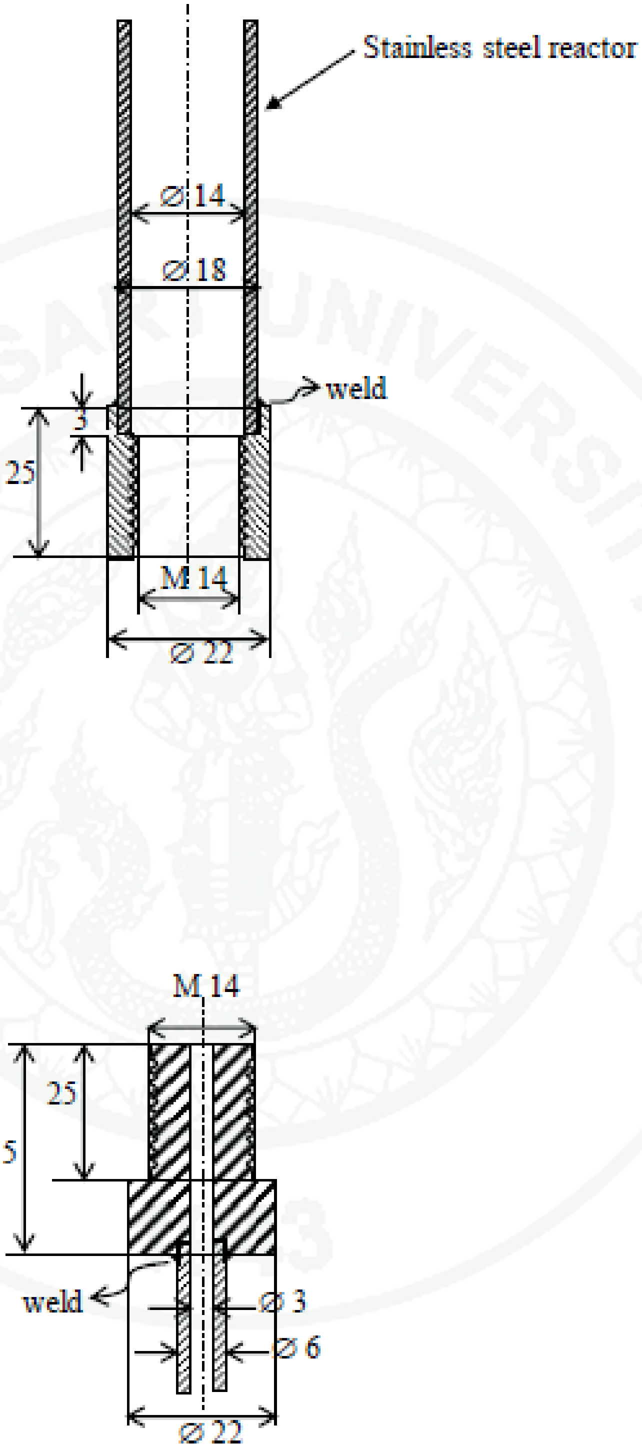

**Figure C2** Opened bottom part drawing of steel reactor.

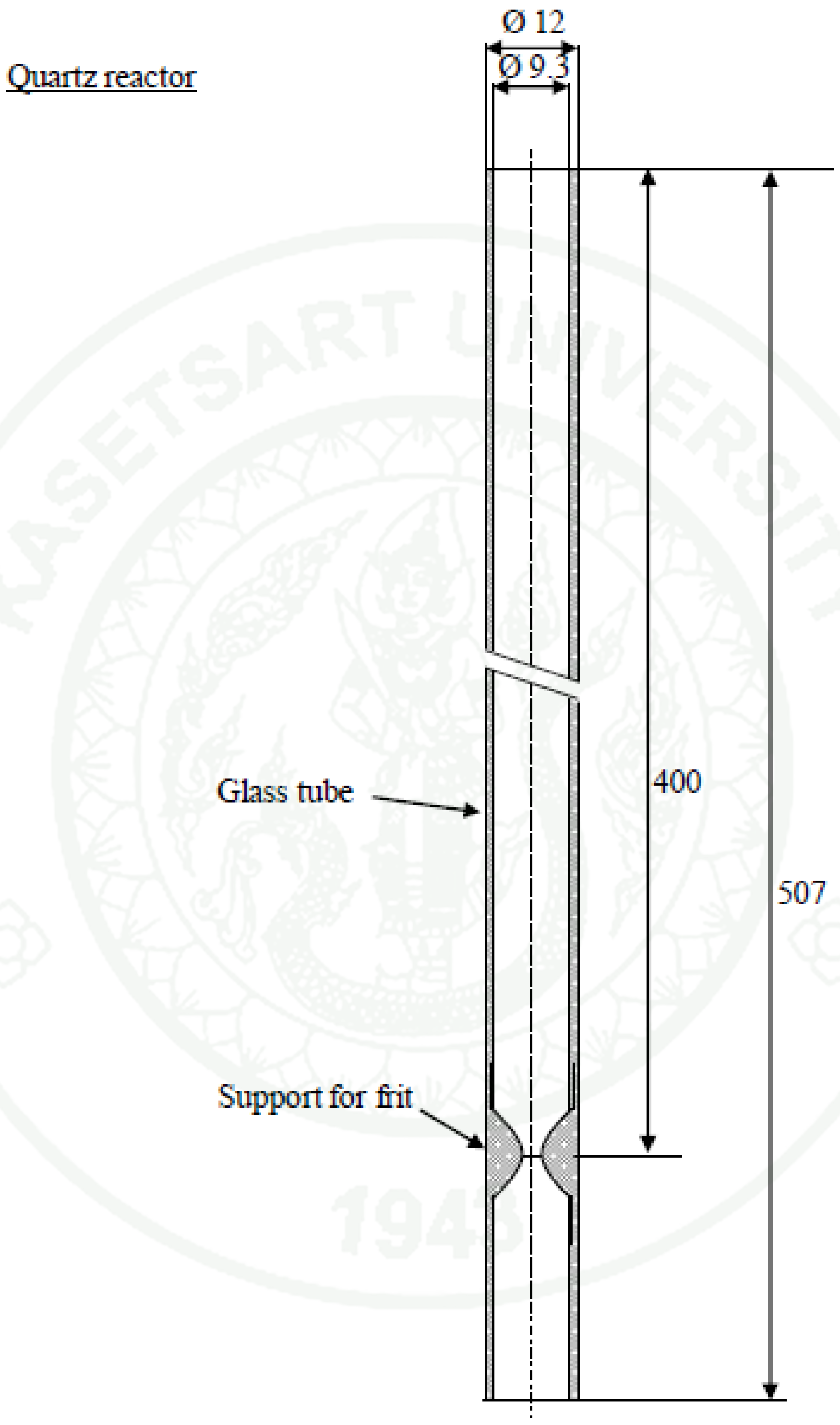

**Figure C3** Quartz reactor drawing.

# Appendix D

## EXAFS analysis of Ce $L_3$-edge of in Ce/$TiO_2$

## 1. Fitting results of Ce as Interstitial defect in anatase $TiO_2$

### 1.1 CATi08-LW

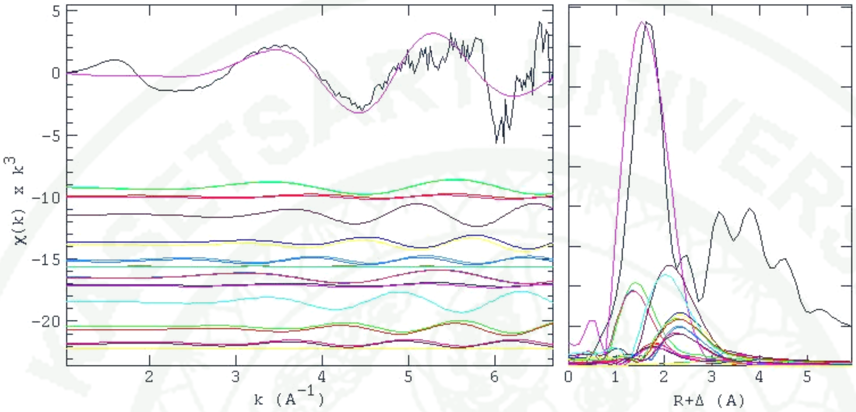

010 (0 = Ce atom , 1 = O atom; Ce – O )

| Coordination Number | R,Å | $\sigma^2$ |
|---|---|---|
| 0.20000E+01 | 0.20864E+01 | 0.75400E-02 |
| 010 | | |
| 0.20000E+01 | 0.20889E+01 | 0.75800E-02 |
| 010 | | |
| 0.10000E+01 | 0.26208E+01 | 0.75700E-02 |
| 010 | | |
| 0.10000E+01 | 0.26538E+01 | 0.75800E-02 |
| 020 (0 = Ce atom, 2 =Ti atom ; Ce – Ti ) | | |
| 0.40000E+01 | 0.28736E+01 | 0.14070E-01 |
| 020 | | |
| 0.20000E+01 | 0.31325E+01 | 0.90500E-02 |
| 020 | | |
| 0.20000E+01 | 0.31538E+01 | 0.90800E-02 |
| 010 | | |
| 0.40000E+01 | 0.32656E+01 | 0.10740E-01 |
| 010 | | |
| 0.40000E+01 | 0.32873E+01 | 0.10750E-01 |
| 01010 | | |
| 0.20000E+01 | 0.41727E+01 | 0.80800E-02 |
| 01010 | | |
| 0.20000E+01 | 0.41777E+01 | 0.83400E-02 |
| 010 | | |
| 0.20000E+01 | 0.20864E+01 | 0.75400E-02 |
| 010 | | |
| 0.20000E+01 | 0.20889E+01 | 0.75800E-02 |
| 010 | | |
| 0.10000E+01 | 0.26208E+01 | 0.75700E-02 |

```
010
 0.10000E+01            0.26538E+01            0.75800E-02
020
 0.40000E+01            0.28736E+01            0.14070E-01
020
 0.20000E+01            0.31325E+01            0.90500E-02
020
 0.20000E+01            0.31538E+01            0.90800E-02
010
 0.40000E+01             0.32656E+01           0.10740E-01
010
 0.40000E+01            0.32873E+01            0.10750E-01
01010
 0.20000E+01            0.41727E+01            0.80800E-02
```

### 1.2 CNTi08-HW

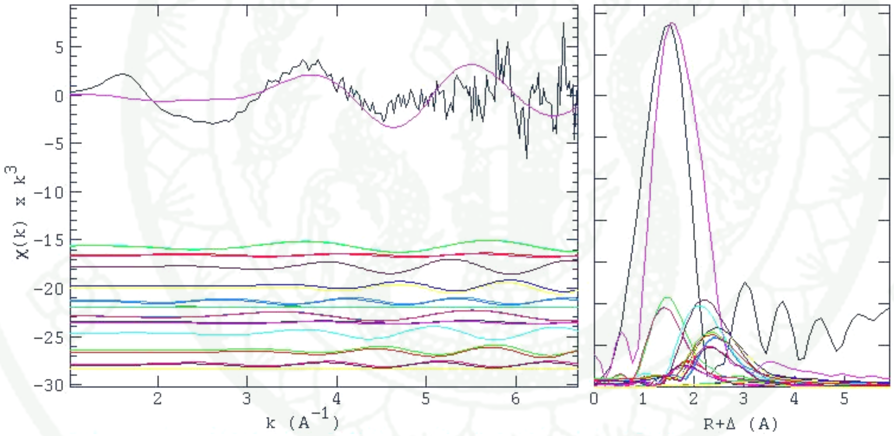

```
010
 0.20000E+01            0.20864E+01            0.90400E-02
010
 0.20000E+01            0.20889E+01            0.90800E-02
010
0.10000E+01             0.26208E+01            0.90700E-02
010
 0.10000E+01            0.26538E+01            0.90800E-02
020
 0.40000E+01            0.28736E+01            0.18070E-01
020
 0.20000E+01            0.31325E+01            0.90500E-02
020
 0.20000E+01            0.31538E+01            0.90800E-02
010
 0.40000E+01            0.32656E+01             0.10740E-01
```

```
010
 0.40000E+01           0.32873E+01           0.10750E-01
01010
 0.20000E+01           0.41727E+01           0.90800E-02
01010
 0.20000E+01           0.41777E+01           0.93400E-02
010
 0.20000E+01           0.20864E+01           0.90400E-02
010
 0.20000E+01           0.20889E+01           0.90800E-02
010
 0.10000E+01           0.26208E+01           0.90700E-02
010
 0.10000E+01           0.26538E+01           0.90800E-02
020
 0.40000E+01           0.28736E+01            0.18070E-01
020
 0.20000E+01           0.31325E+01           0.90500E-02
020
 0.20000E+01           0.31538E+01           0.90800E-02
010
0.40000E+01            0.32656E+01           0.10740E-01
010
 0.40000E+01           0.32873E+01           0.10750E-01
01010
 0.20000E+01           0.41727E+01           0.90800E-02
01010
 0.20000E+01           0.41777E+01           0.93400E-02
```

1.3 CNTi08-LW

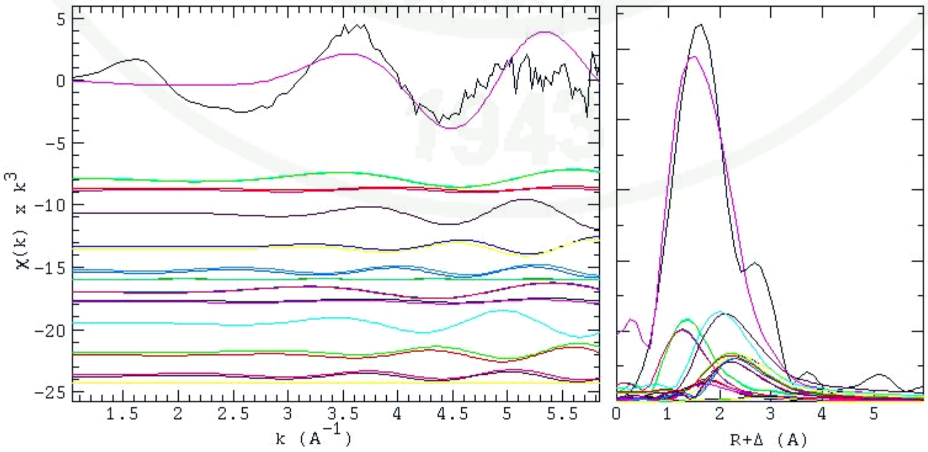

```
010
 0.20000E+01           0.20864E+01           0.53700E-02
```

```
010
 0.20000E+01         0.20889E+01         0.55300E-02
010
 0.10000E+01         0.26208E+01         0.55000E-02
010
 0.10000E+01         0.26538E+01         0.55300E-02
020
 0.40000E+01         0.28736E+01         0.10700E-01
020
 0.20000E+01         0.31325E+01         0.50700E-02
020
 0.20000E+01         0.31538E+01         0.51800E-02
010
 0.40000E+01         0.32656E+01         0.52800E-02
010
 0.40000E+01         0.32873E+01         0.53200E-02
01010
 0.20000E+01         0.41727E+01         0.51800E-02
01010
 0.20000E+01         0.41777E+01         0.51900E-02
010
 0.20000E+01         0.20864E+01         0.53700E-02
010
 0.20000E+01         0.20889E+01         0.55300E-02
010
 0.10000E+01         0.26208E+01         0.55000E-02
010
 0.10000E+01         0.26538E+01         0.55300E-02
020
 0.40000E+01         0.28736E+01         0.10700E-01
020
 0.20000E+01         0.31325E+01         0.50700E-02
020
 0.20000E+01         0.31538E+01         0.51800E-02
010
 0.40000E+01         0.32656E+01         0.52800E-02
010
 0.40000E+01         0.32873E+01         0.53200E-02
01010
 0.20000E+01         0.41727E+01         0.51800E-02
01010
 0.20000E+01         0.41777E+01         0.51900E-02
```

**Table D1** The nearest shells around Ce atom as *interstitial* defect into $TiO_2$ lattice.

| atom shell | # Coordination | Distance ($A^o$) | Averaged $\sigma^2$ |
|---|---|---|---|
| Ce-O | 4 | 2.086±0.003 | 0.007±0.002 |
| Ce-O | 2 | 2.621±0.030 | 0.0073±0.002 |
| Ce-Ti | 4 | 2.8736 | 0.0143±0.004 |
| Ce-Ti | 4 | 3.1431±0.010 | 0.0078±0.002 |

## 2. Fitting results of Ce as substitution defect in anatase $TiO_2$

### 2.1 CATi08-LW

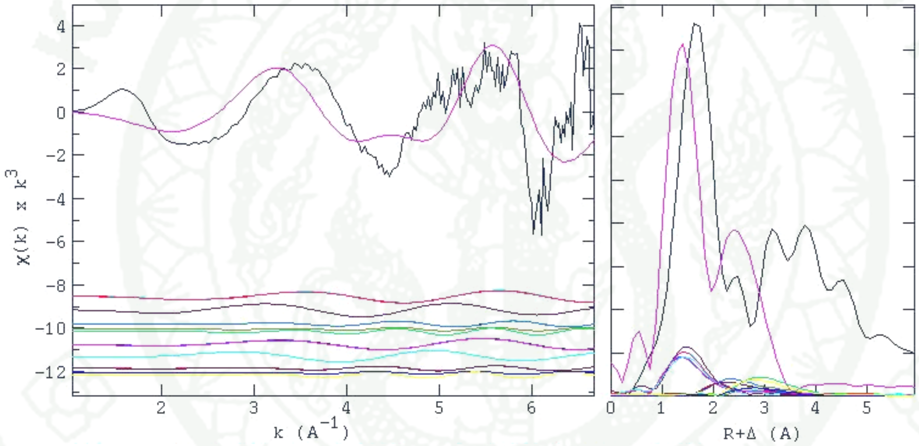

```
010
 0.10000E+01          0.20837E+01          0.89600E-02
010
 0.10000E+01          0.20843E+01          0.91800E-02
010
 0.10000E+01          0.20843E+01          0.91800E-02
010
 0.10000E+01          0.20849E+01          0.91800E-02
010
 0.20000E+01          0.22217E+01          0.18240E-01
020
 0.10000E+01          0.31542E+01          0.18030E-01
020
 0.10000E+01          0.31542E+01          0.18030E-01
020
 0.10000E+01          0.31555E+01          0.18030E-01
020
 0.10000E+01          0.31562E+01          0.18030E-01
```

```
020
 0.10000E+01          0.37750E+01          0.18580E-01
020
 0.20000E+01          0.37757E+01          0.18680E-01
010
 0.10000E+01          0.20837E+01          0.89600E-02
010
 0.10000E+01          0.20843E+01          0.91800E-02
010
 0.10000E+01          0.20843E+01          0.91800E-02
010
 0.10000E+01          0.20849E+01          0.91800E-02
010
 0.20000E+01          0.22217E+01          0.18460E-01
020
 0.10000E+01          0.31542E+01          0.18970E-01
020
 0.10000E+01          0.31542E+01          0.18970E-01
020
 0.10000E+01          0.31555E+01          0.18970E-01
020
 0.10000E+01          0.31562E+01          0.18970E-01
020
 0.10000E+01          0.37750E+01          0.18940E-01
020
 0.20000E+01          0.37757E+01          0.18940E-01
```

### 2.2 CNTi08-HW

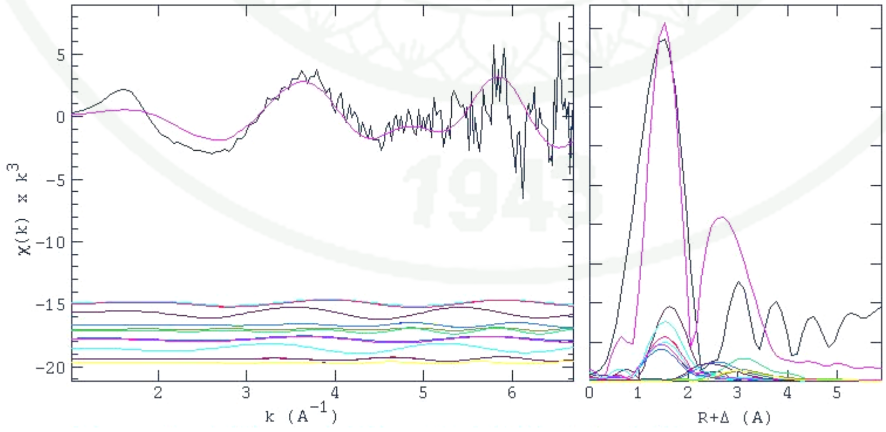

```
010
 0.10000E+01          0.20837E+01          0.15440E-01
010
 0.10000E+01          0.20843E+01          0.12090E-01
010
```

```
 0.10000E+01           0.20843E+01           0.12090E-01
010
 0.10000E+01           0.20849E+01           0.12090E-01
010
 0.20000E+01           0.22217E+01           0.13730E-01
020
 0.10000E+01           0.31542E+01           0.15820E-01
020
 0.10000E+01           0.31542E+01           0.15820E-01
020
 0.10000E+01           0.31555E+01           0.15820E-01
020
 0.10000E+01           0.31562E+01           0.15820E-01
020
 0.10000E+01           0.37750E+01           0.15170E-01
020
 0.20000E+01           0.37757E+01           0.15590E-01
010
 0.10000E+01           0.20837E+01           0.15440E-01
010
 0.10000E+01           0.20843E+01           0.12090E-01
010
 0.10000E+01           0.20843E+01           0.12090E-01
010
 0.10000E+01           0.20849E+01           0.12090E-01
010
 0.20000E+01           0.22217E+01           0.13640E-01
020
 0.10000E+01           0.31542E+01           0.15830E-01
020
 0.10000E+01           0.31542E+01           0.15830E-01
020
 0.10000E+01           0.31555E+01           0.15830E-01
020
 0.10000E+01           0.31562E+01           0.15830E-01
020
 0.10000E+01           0.37750E+01           0.15700E-01
020
 0.10000E+01           0.37757E+01           0.15590E-01
```

2.3 CNTi08-LW

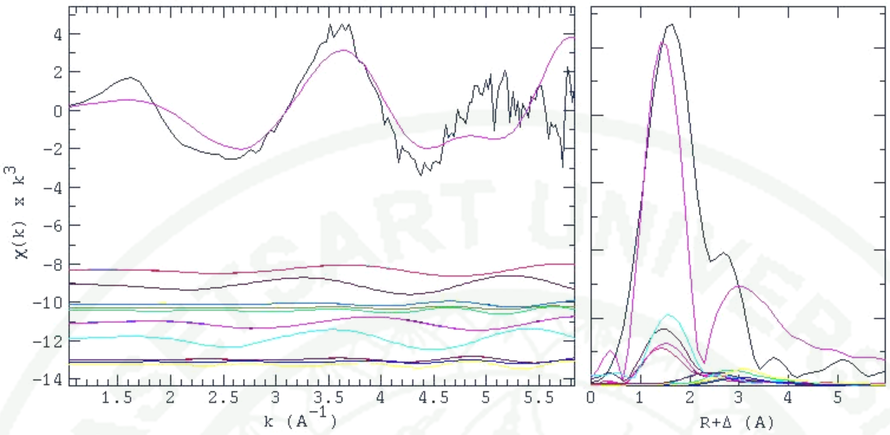

```
010
 0.10000E+01         0.20837E+01         0.81700E-02
010
 0.10000E+01         0.20843E+01         0.81800E-02
010
 0.10000E+01         0.20843E+01         0.81800E-02
010
 0.10000E+01         0.20849E+01         0.81800E-02
010
 0.20000E+01         0.22217E+01         0.10060E-01
020
 0.10000E+01         0.31542E+01         0.16530E-01
020
 0.10000E+01         0.31542E+01         0.16530E-01
020
 0.10000E+01         0.31555E+01         0.16530E-01
020
 0.10000E+01         0.31562E+01         0.16530E-01
020
 0.10000E+01         0.37750E+01         0.16920E-01
020
 0.20000E+01         0.37757E+01         0.16180E-01
010
 0.10000E+01         0.20837E+01         0.81700E-02
010
 0.10000E+01         0.20843E+01         0.81800E-02
010
 0.10000E+01         0.20843E+01         0.81800E-02
010
 0.10000E+01         0.20849E+01         0.81800E-02
010
 0.20000E+01         0.22217E+01         0.10620E-01
```

```
020
 0.10000E+01           0.31542E+01           0.16920E-01
020
 0.10000E+01           0.31542E+01           0.16920E-01
020
 0.10000E+01           0.31555E+01           0.16920E-01
020
 0.10000E+01           0.31562E+01           0.16920E-01
020
 0.10000E+01           0.37750E+01           0.16840E-01
020
 0.20000E+01           0.37757E+01           0.16840E-01
```

**Table D2** The nearest shells around Ce atom as *substitution* defect into $TiO_2$ lattice.

| atom shell | # Coordination | Distance (A$^o$) | Averaged $\sigma^2$ |
|---|---|---|---|
| Ce-O | 4 | 2.084±0.001 | 0.0109±0.005 |
| Ce-O | 2 | 2.2217 | 0.0140±0.004 |
| Ce-Ti | 4 | 3.155±0.001 | 0.0168±0.002 |
| Ce-Ti | 4 | 3.775±0.001 | 0.0169±0.002 |

## 3. Fitting results of Ce as interstitial mixed substitution in anatase $TiO_2$

### 3.1 CATi30-LW; $N_{interstitial}$ : $N_{substitution}$ = 0.354 : 0.646

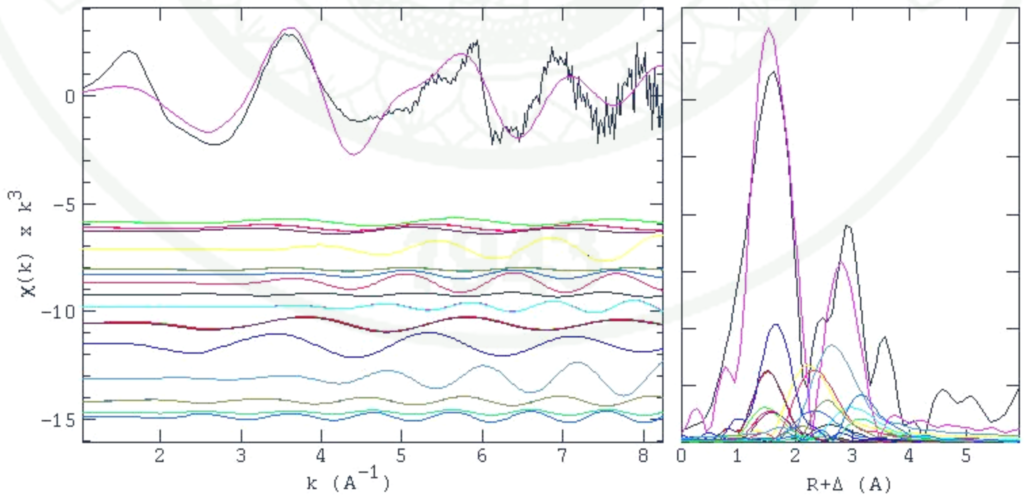

```
010
 0.35440E+00           0.20795E+01           0.98800E-02
 010
 0.35440E+00           0.20803E+01           0.98800E-02
```

```
010
 0.35440E+00          0.21657E+01          0.98400E-02
010
 0.35440E+00          0.21684E+01          0.98400E-02
010
 0.35440E+00          0.22188E+01          0.98300E-02
020
 0.35440E+00          0.27772E+01          0.14100E-02
020
 0.35440E+00          0.27772E+01          0.14100E-02
010
 0.35440E+00          0.28016E+01          0.95500E-02
010
 0.35440E+00          0.28064E+01          0.95500E-02
010
 0.35440E+00          0.28080E+01          0.95500E-02
020
 0.35440E+00          0.29293E+01          0.99700E-02
020
 0.35440E+00          0.29299E+01          0.99700E-02
020
 0.81207E+00          0.29307E+01          0.99700E-02
010
 0.35440E+00          0.33128E+01          0.13800E-02
020
 0.35440E+00          0.36358E+01          0.15800E-02
020
 0.35440E+00          0.36368E+01          0.15800E-02
010
 0.64558E+00          0.20837E+01          0.11000E-01
010
 0.64558E+00          0.20843E+01          0.11000E-01
010
 0.64558E+00          0.20843E+01          0.11000E-01
010
 0.64558E+00          0.20849E+01          0.11000E-01
010
 0.12912E+01          0.22217E+01          0.11500E-01
020
 0.64558E+00          0.31542E+01          0.15300E-02
020
0.64558E+00           0.31542E+01          0.15300E-02
020
 0.64558E+00          0.31555E+01          0.15300E-02
020
 0.64558E+00          0.31562E+01          0.15300E-02
020
 0.64558E+00          0.37750E+01          0.17900E-02
```

```
020
 0.12912E+01            0.37757E+01            0.17900E-02
```

### 3.2 CNTi30-LW; $N_{intersitial}$ : $N_{substitution}$ = 0.219 : 0.781

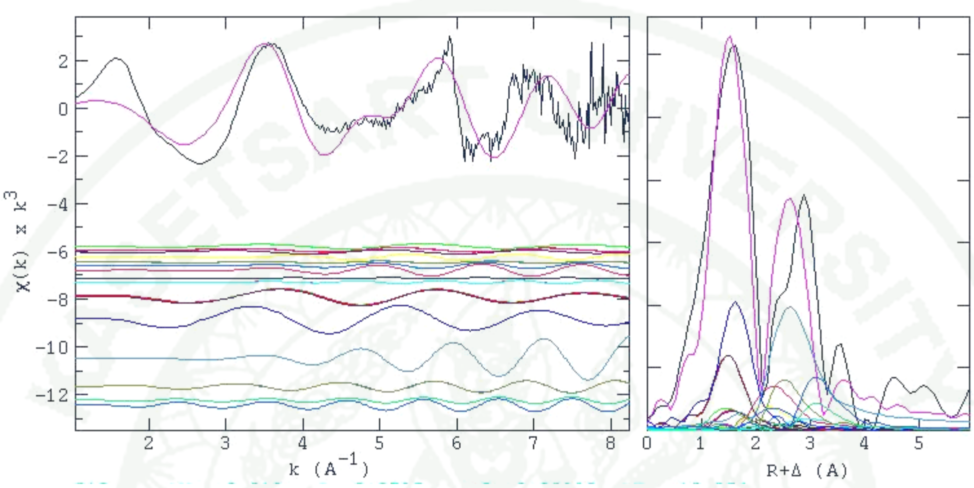

```
010
 0.21891E+00            0.20795E+01            0.99000E-02
010
 0.21891E+00            0.20803E+01            0.99000E-02
010
 0.21891E+00            0.21657E+01            0.99000E-02
010
 0.21891E+00            0.21684E+01            0.99000E-02
010
 0.21891E+00            0.22188E+01            0.99000E-02
020
 0.21891E+00            0.27772E+01            0.99100E-02
020
 0.21891E+00            0.27772E+01            0.99100E-02
010
 0.21891E+00            0.28016E+01            0.92500E-02
010
 0.21891E+00            0.28064E+01             0.92500E-02
010
 0.21891E+00            0.28080E+01            0.92500E-02
020
 0.21891E+00            0.29293E+01            0.93700E-02
020
 0.21891E+00            0.29299E+01            0.93700E-02
020
 0.43792E+00            0.29307E+01            0.93700E-02
010
```

```
 0.21891E+00          0.33128E+01          0.93800E-02
020
 0.21891E+00          0.36358E+01           0.88800E-02
020
 0.21891E+00          0.36368E+01          0.88800E-02
010
 0.78155E+00          0.20837E+01          0.14000E-01
010
 0.78155E+00          0.20843E+01          0.14000E-01
010
 0.78155E+00          0.20843E+01          0.14000E-01
010
 0.78155E+00          0.20849E+01          0.14000E-01
010
 0.15632E+01          0.22217E+01          0.14050E-01
020
 0.78155E+00          0.31542E+01           0.20300E-02
020
 0.78155E+00          0.31542E+01          0.20300E-02
020
 0.78155E+00          0.31555E+01          0.20300E-02
020
 0.78155E+00          0.31562E+01          0.20300E-02
020
 0.78155E+00          0.37750E+01          0.30900E-02
020
 0.15632E+01          0.37757E+01          0.30900E-02
```

**Table D3** The nearest shells around Ce atom as *interstitial mixed substitution* defect into $TiO_2$ lattice.

| atom shell | # Coordination | Distance ($A^o$) | Averaged $\sigma^2$ |
|---|---|---|---|
| Ce-O | 2 | 2.083 ±0.004 | 0.0116±0.001 |
| Ce-O | 2 | 2.1671±0.002 | 0.0099±0.001 |
| Ce-O | 1 | 2.2202±0.001 | 0.0113±0.001 |
| Ce-O | 1 | 3.3128 | 0.0054±0.004 |
| Ce-Ti | 2 | 2.7772 | 0.0057±0.004 |
| Ce-Ti | 4 | 2.9300±0.004 | 0.0097±0.0003 |
| Ce-Ti | 2 | 3.6363±0.001 | 0.0052±0.004 |

# CURRICULUM VITAE

**NAME** : Miss Anwaraporn Niltharach

**BIRTH DATE** : September 25th, 1977

**BIRTH PLACE** : Sakon nakhon, Thailand

**EDUCATION** :

| **YEAR** | **INSTITUTE** | **DEGREE/DIPLOMA** |
|---|---|---|
| 1999 | Kasetsart Univ. | B.Sc. (Chemistry) |
| 2003 | Kasetsart Univ. | M.Sc. (Chemistry) |

**POSITION/TITLE** : Lecturer

**WORK PLACE** : Faculty of Resource and Environment,
Kasetsart University, Siracha campus

**SCHOLARSHIP/AWARDS**

**Graduate scholarships** :

1) Research Assistant for performing the XPS and XAS operations, 2006-2007. Synchrotron Light Research Institute, Ministry of Science and Technology, Thailand.

2) Sandwich Program, 2006-2009. Strategic Scholarship for Frontier Research Network of Thailand Commission of Higher Education, Ministry of Education, Thailand.

3) DAAD scholarship for International PhD candidates, September – December 2009. Insitutut für Technische Chemie und Polymerchemie. Karlsruher Institut für Technologie, Germany.

**Research Fund :**

Project: Studying of Wastewater Quality from the Communities and Industries at Sriracha, Chonburi province. 2004-2005. Kasetsart University Research and Development Institute.

**Presentations and Publications:**

1. **Niltharach, A.** and A. Worayingyong. Vanadium and Cerium species on $TiO_2$ (anatase) oxidative catalysts: Preparation and characterization by X-ray and Raman spectroscopies, in The 29th Congress on Science and Technology of Thailand (STT 2003), Khonkaen university, Khonkaen, Thailand, 2003, p. 115.

2. Worayingyong, A., **A. Niltharach** and Y. Poo-arporn. 2004. A comparative study of toluene catalytic oxidation over cerium/$TiO_2$ (anatase) and vanadium/$TiO_2$ (anatase) catalysts. *ScienceAsia*. 30(4): 341-349.

3. **Niltharach, A.**, A. Worayingyong and P. Songsiriritthigul. X-ray absorption spectroscopy study of the Ti K edge and Ce $L_3$ edge in Ce doped $TiO_2$ crystalline, in Pure and Applied Chemistry Internation Conference (PACCON 2008), Sofitel Centara Grand Bangkok, Bangkok, Thailand, January 30 - February 1, 2008.

4. T-Thienprasert, J., S. Klaithong, **A. Niltharach**, A. Worayingyong, S. Na-Phattalung and S. Limpijumnong. 2010. Local structure of cobalt in Co-doped $TiO_2$ by Synchrotron X-ray Absorption Near Edge Structure (to prepare manuscript).

**Award:**

Instantaneous Total Product Stream Analysis Unit, **Anwaraporn Niltharach**, Korakoch Prangtong, Siriapa Pleangtarat, Pinsuda Viravathana and Attera Worayingyong, the Consolation award of KU Innovation awards, 2009